Biventricular Active Mesh Model of the Heart and Analysis of Morphologic Changes Toward Physiology and Pathologies

by

Chun G. Schiros

A dissertation submitted to the Graduate Faculty of
Auburn University
in partial fulfillment of the
requirements for the Degree of
Doctor of Philosophy

Auburn, Alabama
December 8th 2012

Approved by

Thomas S. Denney, Jr., Chair, Professor of Electrical and Computer Engineering
Stanley J. Reeves, Professor of Electrical and Computer Engineering
Shumin Wang, Assistant Professor of Electrical and Computer Engineering
Louis J. Dell'Italia, Director of center for Heart Failure Research

ABSTRACT

Cardiovascular disease (CVD) has been reported as the number one cause of death in the world. It is estimated that by 2030, about 23.6 million people will die from a type of CVD. It is a problem that crosses both gender and ethnicity and is a problem that gets worse with age. Heart failure is usually the end result of most cardiac diseases. Therefore, correct diagnosis and early prevention of CVDs are significantly important. Used as powerful tools for clinical diagnosis, medical imaging techniques have been dramatically developed and improved over the past two decades. Among them, cardiovascular magnetic resonance imaging (cMR) is becoming a leading imaging modality for advanced clinical research, drug studies and patient management due to its high image resolution, minimal invasion and reproducibility, compared with other conventional imaging techniques. Geometric and functional analyses of the left ventricle (LV) of human hearts have been well developed using cMR. However, the development of right ventricle (RV) shape and functional analyses are relatively new territory. Analysis of the RV and interaction between the LV and the RV can provide extra information that might suggest subtle abnormality of cardiac function in patients with normal LV functions.

In this dissertation, three major research projects are presented.

The first study evaluated the role of the alterations in the changes in LV volume and geometry in achieving elevated stroke volume in endurance athletes' hearts and patients with chronic compensated mitral regurgitation (MR), which represented physiologic, and pathologic left ventricular volume overload. Cine cMR, with tissue tagging was performed on all subjects of

both groups. Three-dimensional data analysis, utilizing in-house software was performed to evaluate the differences in geometry and function between the two groups. The result of this study shows that in the setting of similar increases in LV volumes and stroke volume, marathoners' hearts maintain a normal LV sphericity, a conically-shaped apex and normal wall thickness with lower LV twist, while, in MR hearts, LV sphericity is increased and the apex is more rounded.

The second study further assessed the important role that apex remodeling played in the progression of the severity of mitral regurgitation and its significance as an indicator for timing of surgery. cMR and 3D data analysis were performed on 94 patients with chronic degenerative isolated MR to uncover the importance of volumetric analysis as an indicator of left ventricular remodeling. Among these patients, 35 patients underwent mitral valve repair and each had a 12-month follow-up analysis. The major finding of the study is that LV end-systolic (LVES) dimension does not accurately reflect the extent of LV remodeling, largely due to rounding of the apex and global spherical LV remodeling.

The previous two studies highlighted the need for accurate modeling of LV geometry – particularly at the apex. Other research has highlighted a similar need for accurate modeling of RV geometry, which does not have the circular symmetry of the LV. Most current LV models use a polar type of coordinate system with a singularity at the origin, which makes it difficult to model the LV apex and the RV as a whole.

Therefore, for the third research project, we proposed a biventricular active mesh model of the human heart that can accurately fit smooth surfaces to both the LV and RV including the LV apex and RV base. The computation time for generating a mesh for a new subject using the proposed algorithm was less than one minute. Moreover, such new meshes can potentially

correct the contour errors near both the LV and RV outflow tracts which were usually difficult to determine manually, because the generated new meshes were constrained by the variation from their training sets.

ACKNOWLEDGEMENTS

I would love to express my most sincere gratitude to my PhD advisor Dr. Thomas S. Denney, Jr. It was his tremendous encouragement and his strong confidence in me that helped me explore my potential and made me become who I am today. He was always patient in guiding me through my research, recognized my strengths and spared no effort to provide me the best opportunities. His meticulous research attitude, considerate personality, and sharp vision in the field of research, have been a great influence on me. With his cultivating influence, I have learned how to be a good researcher.

I greatly thank Dr. Stanley Reeves who has been an extraordinary professor in the past six years of my research. His classes were always fun to attend and he made the material easy to understand. His passion and unconditional devotion to education and research have touched me deeply and gained my greatest respect. Working with Dr. Reeves as a teaching assistant had provided me a great opportunity to learn more from him. Even after I have left Auburn for UAB, Dr. Reeves has still kept in touch displaying a genuine concern and a commitment to my well-being. For all this, I am very thankful to him.

I cannot give more thanks to Dr. Louis J. Dell'Italia. Working with him in the last two years has been a remarkable life experience. His strong encouragement and trust in me have helped me achieve my success in research and helped me believe in myself. His limitless research desire, profound expertise, and unsparing appreciation of others' work inspired me

deeply. His thorough care for my research and my life are so marvelous that I cannot thank him enough.

I am also very thankful for Dr. Shumin Wang for his gracious willing to be my committee member, for his time and great insights on my research project. Besides research, the conversations with him about what is the most important life achievement have been a great lesson to me.

I also want to thank Dr. Nedret Billor as she was graciously willing to be my University Reader and that she gave me a lot of good advice for my dissertation in terms of statistics. I thank her being a great mentor for my master degree in Probability and Statistics, from which I have learned the solid knowledge of statistics, which is very useful for my PhD research.

The first four years of my PhD research was supported by the NIH Specialized Center of Clinically Oriented Research in Cardiac Dysfunction HL7077. I thank Dr. Louis J. Dell'Italia, the principle investigator, and Dr. Thomas S. Denney, Jr., Dr. Himanshu Gupta, Dr. Steven Lloyd, the co-investigators of this grant. The last two years of my research was supported by the NIH National Heart Lung and Blood Institute (NHLBI) grand 1 R01 HL104018-01 (R01). I thank Dr. Himanshu Gupta, the principle investigator, and Dr. Thomas S. Denney, Jr., the co-investigator of this grant.

My thanks also go to my dear friends from Auburn, Wei Zha, Wenting Deng, Tao Ma, Bharath Ambale Venkatesh, Qiqi Liang, Yuan Tian and friends from UAB, Kevin Wei, Pam Powell, Ke Shi, Pia Todora, Danielle Yancey, Justin Barnes, and Eddie Bradley. I shared laughter and tears with them and dreamed about the future with them. I cannot imagine my life without these friends. I specially want to thank Yuan who lived with me for the first two years

and taught me how to be a cook from scratch. I thank Kevin Wei for a happy friendship that we built together during my studying at UAB.

Finally, I want to specially thank my family for their unlimited love for me. I thank my husband Matthew C. Schiros dearly. He has changed the way I look at this world and how I value life. He has been supportive, patient, loving and encouraging. He gives me the bravery to go through the difficulties of life; we share the joys and sorrows along the way. I thank my sister Jie Guo for being a good listener and light-hearted girlfriend. She trusts me as a big sister and always looks up to me. I thank her for helping me strive for my best. I greatly thank my dad Binglong Guo and my mom Xiu'E Xiao for their selfless love for me. Their endless support is the reason that I have made it this far. I truly admire their success and will try to match their achievement. This dissertation is dedicated to them.

TABLE OF CONTENTS

Abstract ii

Acknowledgements v

List of Figures xii

List of Abbreviations xv

Chapter 1 Introduction 1

1.1 Cardiac Anatomy 1

1.2 Heart Diseases 6

1.3 Cardiac Imaging Modalities 7

1.3.1 Echocardiography 8

1.3.2 Computed Tomography 8

1.3.3 Nuclear Imaging 8

1.3.4 Cardiovascular Magnetic Resonance imaging 9

1.4 cMR Protocols 11

1.5 Content of the Following Chapters 14

Chapter 2 Ventricular Structural Remodeling in Marathoners 16

2.1 Introduction 17

2.2 Material and Methods 18

2.2.1 Study Population 18
2.2.2 cMR 18
2.2.3 LV Work Rate 20
2.2.4 Statistical Analysis 20
2.3 Results 21
2.3.1 Patient Demographics 21
2.3.2 Ventricular Volumes 21
2.3.3 LV Global and Regional Geometry 22
2.3.4 LV Strains Indices 25
2.4 Discussion and Conclusions 27
Chapter 3 Magnetic Resonance Imaging with Three-Dimensional Analysis Reveals Important Left Ventricular End-Systolic Remodeling in Isolated Mitral Regurgitation 29
3.1 Introduction 29
3.2 Methods 31
3.2.1 Study Population 31
3.2.2 Surgery 31
3.2.3 Magnetic Resonance Imaging 32
3.2.4 Bullet Formula 34
3.2.5 Statistical Analysis 34
3.3 Result 36
3.3.1 Clinical Characteristics 36

3.3.2 cMR-Derived Variables in Controls and MR Patients 37
3.3.3 Effect of LVESD on Baseline LV Geometry and Function 40
3.3.4 LV Geometry and Function following MV repair 43
3.3.5 Recovery after Surgery in MR Patients with LVESD < and ⩾ 37 mm 45
3.3.6 Incidence of Post-operative LV Dysfunction 48
3.3.7 Supplementary Analysis 49
3.4 Discussion 53
Chapter 4 Myocardial Surface Modeling Using Cine CMR 57
4.1 Introduction 57
4.1.1 Coordinate-Based Surface Modeling 59
4.1.2 Non-Coordinated-Based Modeling 61
4.1.3 Conclusion 64
4.2 Motivation 66
4.3 Skrinjar's Method 69
4.4 Statistical Deformable Model 74
4.4.1 Previous Research 74
4.4.2 Active Shape Model (ASM) 75
4.5 Proposed Biventricular Active Mesh Model 76
4.5.1 Triangulated Mesh Generation and Smoothing 77
4.5.2 Active Mesh Model (AMM) 83

4.5.3 Cardiac Geometric and Functional Analyses 88

4.6 Results 97

4.6.1 Study Population 97

4.6.2 Model Performance Validation 97

4.7 Discussion 120

4.8 Conclusion 122

Chapter 5 Conclusion and Future Work 124

bibliography 127

LIST OF FIGURES

Figure 1.1 Interior view of a human heart. 2

Figure 1.2 Cardiac cycle 5

Figure 1.3 Pathological heart remodeling 6

Figure 1.4 Cine MRI slice prescriptions 12

Figure 1.5 Tagged cMR images of short-axis view, 4CH and 2CH views 13

Figure 1.6 Coronary artery territories 14

Figure 2.1 LV and RV cMR short-axis images 23

Figure 2.2 LV and RV cMR long-axis images 24

Figure 2.3 Comparisons of LV ED and ES geometric remodeling 25

Figure 2.4 LVES twist of three representatives of control, marathoner and MR 26

Figure 3.1 Description of MR LV remodeling 39

Figure 3.2 Correlation between LVESV and LVESD 40

Figure 3.3 Comparisons of geometry and shortening in controls vs. MR 42

Figure 3.4 Comparisons of geometry in controls vs. surgical MR at ED 46

Figure 3.5 Comparisons of geometry in Controls vs. surgical MR at ES 47

Figure 3.6 Comparisons of LVES maximum shortening in controls vs. surgical MR 48

Figure 3.7 Comparisons of geometry in controls vs. surgical MR (LVEF>60%) at ED 51

Figure 3.8 Comparisons of geometry in controls vs. surgical MR (LVEF>60%) at ES 52

Figure 3.9 Comparisons of maximum shortening in controls vs. surgical MR (LVEF>60%) 53

Figure 4.1 Triangulated cubes for marching cubes algorithm 62

Figure 4.2 Illustration of the terracing effects by marching cubes 63

Figure 4.3 Illustration of the interior heart with RVOT highlighted 67

Figure 4.4 Summery of Skrinjar's Method[120] 69

Figure 4.5 Biventricular active mesh model generation procedure 77

Figure 4.6 2D illustration of the angular interpolation 79

Figure 4.7 A typical LV and RV epicardium 3D segmentations 79

Figure 4.8 Illustration of the intersection between 4CH view slice and LVOT slice 80

Figure 4.9 Result of adding extra RV short axis contour 81

Figure 4.10 Illustration of the one ring neighborhood of a vertex v 83

Figure 4.11 Active mesh deformation flow chart 87

Figure 4.12 The coordinate system on the tangent plane of vertex v 91

Figure 4.13 Illustration of the LV location in the prolate spheroidal coordinates 93

Figure 4.14 Local coordinates on the RV free wall 94

Figure 4.15 Illustration of the LV and RV segments in the prolate spheroidal coordinates 96

Figure 4.16 Example of the RV segments 96

Figure 4.17 The curvature error by triangulation on a perfect sphere. 100

Figure 4.18 Illustration of a prolate spheroid and a perfect normal LV 101

Figure 4.19 The curvature errors on the perfect LV versus V 101

Figure 4.20 The curvature errors on the perfect LV by increasing semi-minor to semi-major axis ratio 102

Figure 4.21 The curvature errors versus segment levels 103

Figure 4.22 The raw curvature errors versus segment levels 104

Figure 4.23 The curvature errors versus M 106

Figure 4.24 The curvature errors by increasing γ 107

Figure 4.25 The mesh goodness of fit by increasing γ 108

Figure 4.26 Illustration of the deformed triangulated surfaces with fitted contours 109

Figure 4.27 Compare AMM1 versus AMM2 based on the stroke volume difference 110

Figure 4.28 Compare AMM1 versus AMM3 based on the stroke volume difference 111

Figure 4.29 Correlation analysis and Bland-Altman plot of LVSV versus RVSV 112

Figure 4.30 Scatter plot and correlation analysis of circumferential curvatures between PSB and Triangulated 113

Figure 4.31 Bland-Altman plot of circumferential curvature comparison 114

Figure 4.32 Scatter plot and correlation analysis of longitudinal curvatures between PSB and the proposed method 115

Figure 4.33 Bland-Altman plot of longitudinal curvature comparison..... 116

Figure 4.34 Illustration of the surface fitting by the proposed method vs. PSB..... 117

Figure 4.35 Compare LV Apex Curvatures between Normal and MR 118

Figure 4.36 Boxplot of LVSV in the normal test group and MR test group 119

Figure 4.37 Boxplot of RVEDV in the normal test group and PH test group 120

LIST OF ABBREVIATIONS

LV	Left Ventricle
RV	Right Ventricle
ED	End-Diastole
ES	End-Systole
EF	Ejection Fraction
cMR	Cardiovascular Magnetic Resonance imaging
MRI	Magnetic Resonance Imaging

CHAPTER 1 INTRODUCTION

Medical image analysis has been widely used in clinical applications for diagnosing brain function, heart diseases, knee problems, and so on. Since cardiovascular diseases have been recognized as the most dominant cause of death in the world [1], cardiac imaging techniques have quickly developed and are commonly employed in cardiac clinical practice [2]. The primarily used imaging modalities for human hearts include but are not limited to, Computed Tomography (CT), nuclear imaging, ultrasound and Cardiovascular Magnetic Resonance imaging (cMR) [2]. Even though CT and ultrasound are more regularly used in clinical practice, there are more evident advantages of using cMR. The most important strength of cMR is that it does no harm to patients due to the lack of ionizing radiation, which is required for CT or single-photon emission CT (SPECT). Moreover, cMR scans have superior temporal resolution compared with CT scans and better spatial resolution than ultrasound. Compared with nuclear imaging, such as positron emission tomography (PET) and SPECT, which only focus on functional analysis, evaluation using cMR is the most comprehensive.

This chapter will first describe the anatomy and function of human hearts. Then a brief introduction on several cardiac pathologies will be introduced, followed by an overview of cardiac imaging modalities. A summary of the following chapters is presented at the end.

1.1 Cardiac Anatomy

A human heart is about the size of a fist, located anterior to the vertebral column and posterior to the sternum. It weighs about 200 grams to 425 grams [3], varying from males to females. Figure 1.1[4] shows the interior view of the anatomy of a normal human heart.

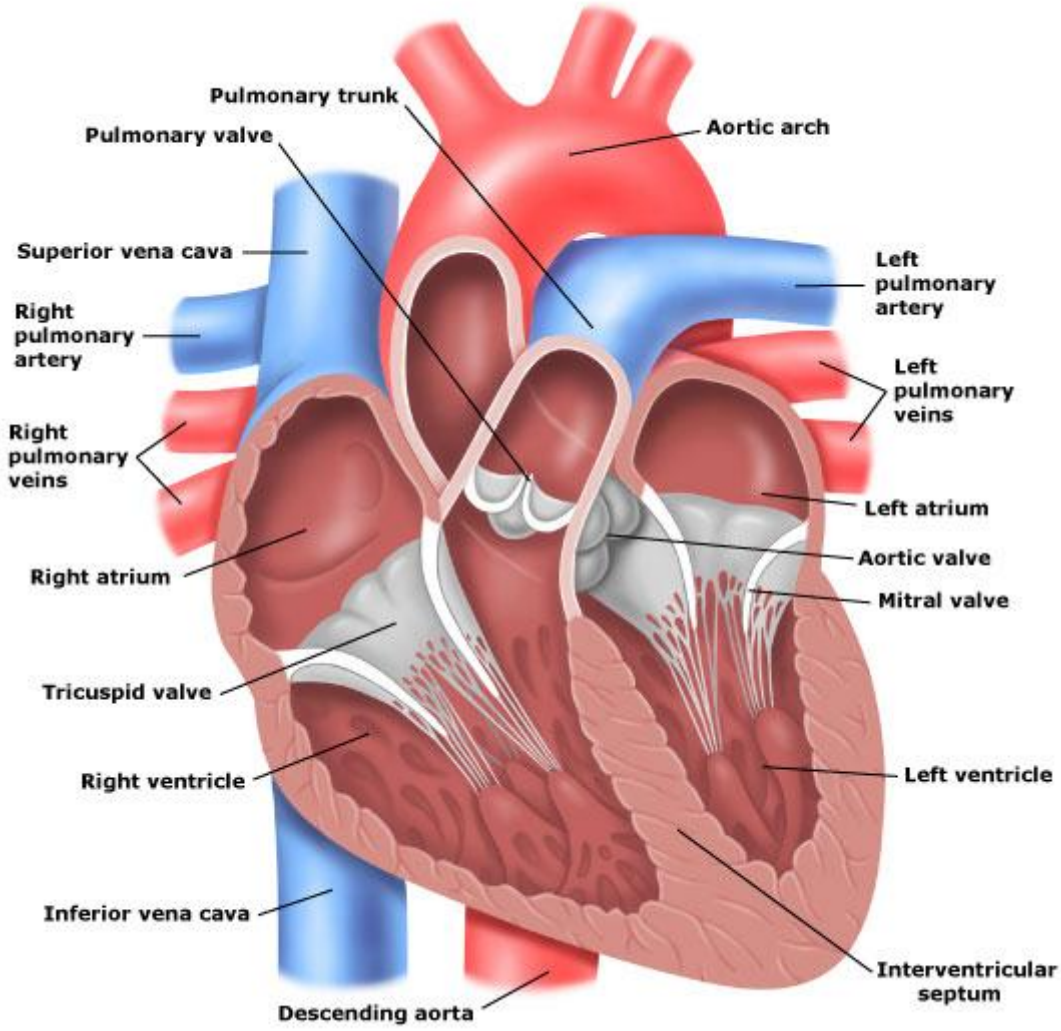

Figure 1.1 Interior view of a human heart.

The main purpose of the heart is to cycle blood throughout the body. The heart contains four chambers to perform this function: the left and right atria, and the LV and the RV [5]. The heart also contains four valves: the tricuspid valve in between the right atrium and the RV, the pulmonary valve connecting the RV and the pulmonary artery, the mitral valve connecting the LV and the left atrium, and the aortic valve in between the LV and the aorta. The mitral valve and the tricuspid valve are connected to the papillary muscle through fibrous strands called chordate tendineae. The wall that separates the LV and RV is called interventricular septum. The walls across the septum are called the free walls. The heart is connected with the circulatory system through arteries which send oxygenated blood out of the heart and veins which return deoxygenated blood back to the heart. The superior vena cava and inferior vena cava are connected to the right atrium. Deoxygenated blood will return to the right atrium from systemic circulation. Blood passes through the tricuspid valve into the RV and ejects through the pulmonary artery into pulmonary circulation. The oxygenated blood is then sent out from the lung into left atrium through left pulmonary veins and flowing into the LV, where the blood will be ejected into the aorta and then into systemic circulation.

The flowing of blood requires contraction of the heart muscles. The heart muscle consists of myocytes, whose primary function is to contract. Both rhythmic and efficient contraction of the heart chambers and appropriate functioning of valves enable a proper functioning heart. A proper functioning heart can be recognized in two parts, the electrical part and the mechanical part.

The electrical changes within myocytes trigger a contraction. An electrocardiogram (ECG) can measure the electrical conduction within the heart, as shown in Figure 1.2. The sinoatrial (SA) node, also known as the pacemaker, located at the posterior wall, generates action

potentials throughout the atria. Action potentials cause the depolarization and contraction of the atria. It can be detected as a P wave in an ECG as shown in Figure 1.2. The sequence of the electric pulses slows down at the atrioventricular (AV) node, which is located at the inferior-posterior of the interatrium wall, allowing for full contraction and depolarization of the atrium before the ventricles start contracting. The action potentials then pass through the AV node into the ventricles triggering ventricular contraction and depolarization. This can be detected as the QRS complex in an ECG. The T wave represents the repolarization of the ventricles. A complete cardiac cycle usually lasts for about 0.8 seconds. During this time the heart cycle is divided into two phases, systole, from the beginning of R wave till the end of T wave, as the ventricles undergo depolarization to repolarization; and diastole, the rest of the cardiac cycle when the heart is resting and filling.

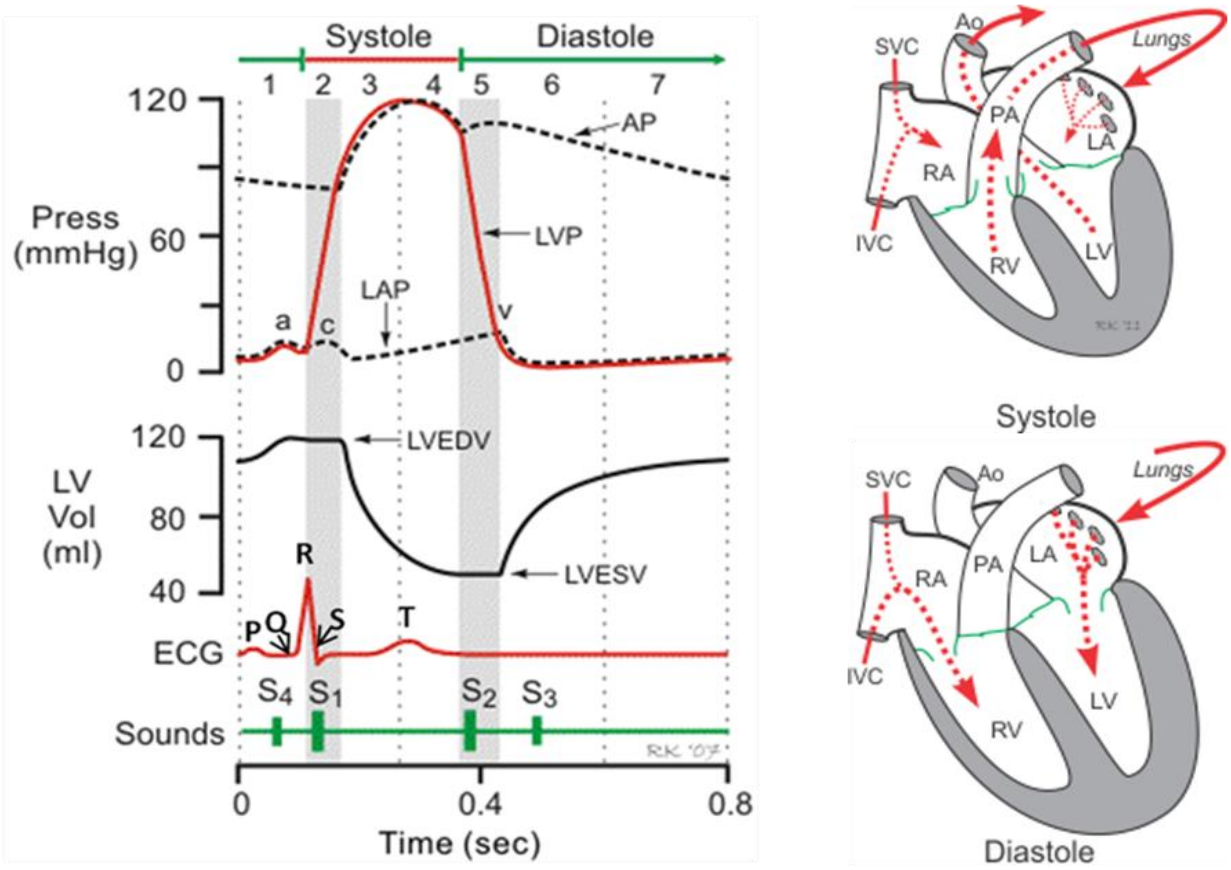

Figure 1.2 Cardiac cycle

The seven phases of the cardiac cycles are, 1, atrial systole; 2, isovolumetric contraction; 3, rapid ejection; 4, reduced ejection; 5, isovolumetric relaxation; 6, rapid filling; 7, reduced filling. [6]

The mechanical properties of the heart are the contraction of the heart muscle and the cooperation of the valves. During diastole, the tricuspid valve opens to allow deoxygenated blood to flow from the right atrium to the RV. At the same time, the mitral valve opens to allow the filling of the LV from the left atrium. During systole, the tricuspid valve closes and the pulmonic valve opens and deoxygenated blood is ejected from the RV and flows to the pulmonary artery which leads to the lungs for oxygen exchange. At the same time, the mitral valve closes and the aortic valve opens to allow ejection of blood from the LV to the aorta; meanwhile, oxygenated blood flows from the lungs through pulmonary veins to the left atrium, and deoxygenated blood returns from the systemic circulation through the superior and inferior

vena cavae to the right atrium. The proper contraction and relaxation of each chamber and also the function of the valves allow for the proper and efficient pumping of the heart. It is noted that, as the papillary muscles contract during systole, they generate pressure on the valve leaflets through the fibrous strands to prevent the valves from opening and leaking blood into the atria. Cardiac pathology such as mitral regurgitation is due to the leaking in the mitral valve to the point that blood fails to fully flow to the aorta and partially flows back to the left atrium, which reduces the effective forward cardiac output and leads to heart failure.

1.2 Heart Diseases

Many heart diseases have been reported to cause heart failure and lead to death. Here are a couple of pathologies that have been studied in the image processing lab.

Hypertension is a medical condition that is associated with elevated systemic arterial blood pressure. This condition is also known as pressure overload. It is mainly caused by increased vascular resistant or/and increased cardiac output. In this condition, the LV enlarges with significantly increased LV mass, which is called concentric remodeling, as shown in Figure 1.3 [7].

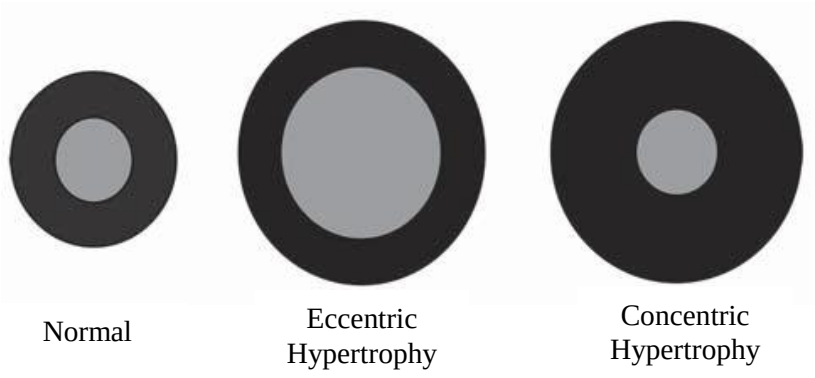

Figure 1.3 Pathological heart remodeling

Pulmonary hypertension is another medical condition where the blood pressure in the pulmonary artery is abnormally increased which causes a higher resistance for the blood to flow into the lungs [8]. This is a heart failure that involves right chambers. cMR can be used as a diagnostic tool not only to provide morphologic information but also functional assessment of the patients with this condition [9].

Heart attack refers to a condition where oxygen-rich blood is blocked from flowing to the heart muscles, causing certain or whole heart muscle damage and death. This is also known as myocardial infarction[10]. People with diabetes have an increased risk of heart attack.

Chronic mitral regurgitation is referred as a long-term vascular disease in which the mitral valve cannot operate properly [11]. As a result, blood is not fully ejected unidirectionally to the aorta and also partially flows back to left atrium. The heart needs to work harder in order to provide enough forward cardiac output. This would cause heart failure in the long term. The LV with a defective valve such as this undergoes eccentric remodeling (see Figure 1.3). The left ventricular volume increases without proportional increase in mass, resulting in a thinner heart wall. This condition is also called LV volume overload. The current guideline of timing for surgery is when the LV ejection fraction > 60% and/or LV end-systolic dimension > 40 mm [12].

1.3 Cardiac Imaging Modalities

Medical imaging modalities can roughly be categorized into two types based on their energy sources: one is using ionizing electromagnetic radiation, such as conventional X-ray and computed tomography (CT) using X rays and positron emission tomography (PET), single-photon emission computed tomography (SPECT) using gamma rays; another is using non-ionizing electromagnetic radiation, such as cMRI using radiofrequency and cardiac

echocardiogram using acoustic energy. Echocardiography, CT, nuclear imaging and cMR are currently the most commonly used imaging modalities in clinical practice.

1.3.1 Echocardiography

Echocardiography, also known as cardiac ultrasound, is the most commonly used tool to evaluate the function and shape of the heart in clinics. A probe with gel on it is placed on the patient's chest and generates a sound wave that travels into the body. Part of the sound wave is reflected by different layers of the tissue and returns to the probe which generates vibration. The vibration is translated into electrical pulses into the ultrasonic scanner and processed into images. It is the easiest, safest and most portable method. Because it is non-invasive and has no side effect, it is widely recommended and used in patients during pregnancy. Echocardiography is usually 2D but 3D echocardiography is possible nowadays. The drawback of this technique is that the images are usually too noisy to produce further detailed analysis.

1.3.2 Computed Tomography

Computed Tomography (CT) utilizes tomography to create a 3D volume of transmission images using 2D X-ray images. They are taken around a single rim of rotation where x-rays are delivered to the body of interest in multiple directions. The different radio-densities of different tissue types enable the generation of a large number of 2D x-ray images, revealing the interior of the body. An imaging computer is used to reformat and reconstruct the 2D images and 3D representation of the structures. CT has become an important imaging tool due to its accuracy and high spatial resolution. However, its radiation dose still remains a safety concern.

1.3.3 Nuclear Imaging

Nuclear imaging is a noninvasive type of medical imaging procedure that injects a type of radioactive material to help the physicians diagnose the condition of a certain disease or the function of the body parts. SPECT is a type of nuclear medicine imaging technique utilizing gamma rays. It requires an injection of a gamma-emitting radioisotope which has been attached to a special radioligand. The radioligand has the chemical binding properties that can bind to certain tissues of interest. This would allow the ligand concentration to be revealed by the gamma camera. SPECT can provide functional information, which has been used in functional brain imaging to analyze brain metabolism and cause of dementia; and in myocardial perfusion imaging (MPI) for assessing ischemic heart disease. It is relatively inexpensive, about $700/scan. PET is another type of nuclear medicine imaging technique using gamma rays. Different from SPECT, PET scanning requires injection of a radiotracer that would emit a positron as it decays. The positron travels in the tissue for a short period of time until it meets an electron, which generates a pair of gamma photons moving towards two opposite directions and detected by the PET scanner simultaneously. PET usually lasts shorter than SPECT because the radiotracer decays rapidly. It provides clearer images which is very important for helping the doctors in the diagnosis of the functioning of tissues and organs. However, it is relatively expensive. A PET scan runs about $3000 while a SPECT scan runs about $400.

1.3.4 Cardiovascular Magnetic Resonance imaging

Cardiovascular Magnetic Resonance imaging (cMR) is a type of imaging modality that utilizes the quantum properties of nuclear spins in the human body. And Hydrogen atom is most frequently used in cMR because it is most abundant (about 63%) and most magnetic resonance sensitive. The acquisition of cMR signals can be categorized in three states: equilibrium state, excitation state and relaxation state. As a proton spins, it generates a small current loop which

generates a small magnetic moment. As an external magnetic field B_0 is applied in Z direction, the protons will align with the field in two different directions, parallel to B_0 in +Z direction and opposite to B_0 in –Z direction, depending on the nuclei energy level and B_0. The net magnetization is called M_0. As the proton has mass, it precesses along Z direction with a Larmor frequency $\omega=\gamma B_0$, γ is gyromagnetic ratio which is constant for protons, equal to 42.58 MHz/Tesla. For a 1.5 T cMR scanner, B_0=1.5 T and ω = 63.87 MHz which is within the radio frequency range. This state is called the equilibrium state. Then the magnetization is excited by another magnetic field B_1 with the same Larmor frequency ω, which is introduced perpendicular to B_0. This energy tips the protons away from the alignment and precess towards the XY direction slowly, generating a flip angle from the alignment. The duration of the radiated frequency (RF) pulse determines the flip angle and the amount of net magnetization. When the transmitter is turned off, the protons will release the energy and return back to the equilibrium state. This procedure is called relaxation. There are two types of relaxation, spin-lattice relaxation, time constant equal to T_1 and spin-spin relaxation, time constant equal to T_2. For spin-lattice relaxation, the protons release the energy to its lattice and T_1 is the time it takes for M_z to recover to 63% of M_0. For spin-spin relaxation, protons interact with each other which interrupts the phase coherence. T_2 is the time it takes for M_{xy} to decay to 37% of M_0. The relaxation time depends on the property of different tissues, which helps generate image contrast between tissues. T_1 scan is using short T_E and short T_R. T_2 scan is using long T_E and long T_R. If a gradient magnetic field is applied along with the main field B_0, a specific region can be selected for imaging, which is called the slice selection.

After collection of the signals, spatial localization is performed, including frequency encoding and phase encoding. After slice selection, a gradient magnetic field is applied to one of

the directions perpendicular to the main field, for example, y direction, such that the phase of protons along y direction is proportional along the gradient field. Then, another gradient magnetic field is applied in a direction perpendicular to the main filed, and the phase encoding gradient field, x direction. The processional frequencies of the proton spins will differ along this gradient field. This is called frequency encoding. The signals from the phase encoding and frequency encoding form a line in k space. The procedure is repeated for the number of the lines in the matrix to form the entire k space. Fourier Transform of the signals and inverse FT yield a 2D image. This procedure is repeated for different slice selection to obtain the entire 3D images.

1.4 cMR Protocols

cMR is superior to other competing cardiac imaging techniques due to its harmlessness to patients and high tissue contrast. There are two typical cMR protocols that are used in this research, cine and tag. The standard protocols are described here and will be used with all participants in the research.

All participants underwent cMR on a 1.5T scanner (Signa, GE Healthcare, Milwaukee, Wisconsin) optimized for cardiac imaging. For cine cMR, ECG-gated, breath-hold steady state free precision technique was used to obtain cine images with standard (2 and 4 Chamber, Long-axis, or 360^0 and Short-axis) views using the following typical parameters: field of view = 40×40 cm, image matrix = 256×128, flip angle = 45^0, T_E = 1.8 ms, T_R = 4 ms, number of cardiac phases = 20, slice thickness = 8 mm without any slice gap. There are particular 10-12 short axis slices that are parallel to each other. Figure 1.4 shows the images at different views from cine cMR with projections from other views.

For tag cMR, a 2D fast gradient recalled spatial modulation of magnetization (FGR-SPAMM) tagging preparation was applied with a tag spacing of 7 pixels to obtain two long-axis

(2 and 4 Chamber view) tagged slices and, on average, 12 short-axis tagged slices per study with following typical parameters: prospective ECG gating, trigger time = 10ms from R wave, slice thickness = 8 mm without any slice gap, flip angle = 10^0, repetition/echo times = 8.0/4.2 ms,

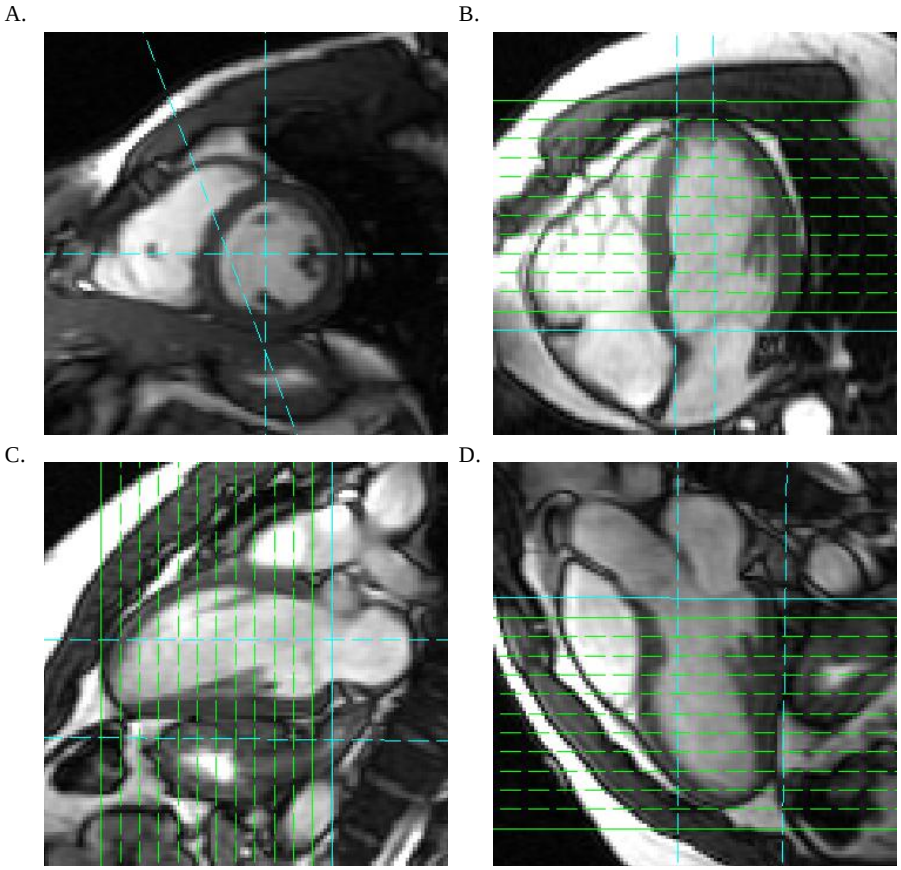

Figure 1.4 Cine MRI slice prescriptions

A. Short axis view with projection of 2 chamber view (vertical), 4 chamber view (horizontal) and long axis; **B**. 4 chamber view with projection of short axis views (13 parallel horizontal lines), 2 chamber and long axis views (2 vertical lines); **C**. 2 chamber view with projection of short axis views (13 parallel horizontal lines) and 4 chamber and long axis views (2 vertical lines); **D**. Long axis view with projection of short axis views (13 parallel horizontal lines), 4 and 2 chamber views (2 vertical lines);

views per segment = 8, typical temporal resolution ~80 ms and number of reconstructed cardiac phase = 20. Figure 1.5 shows the examples of tagged cMR images from a representative subject.

Short axis 4CH 2CH

Figure 1.5 Tagged cMR images of short-axis view, 4CH and 2CH views

The cardiac geometry and function are analyzed using cMR with different protocols for all patients. For local analysis, the heart is segmented into 17 segments according to AHA/ACC [13] (Figure 1.6). Notice that, segment 1 and 2, segment 7 and 8 are separated by anterior RV insertion; segment 3 and 4, segment 9 and 10 are separated by inferior RV insertion.

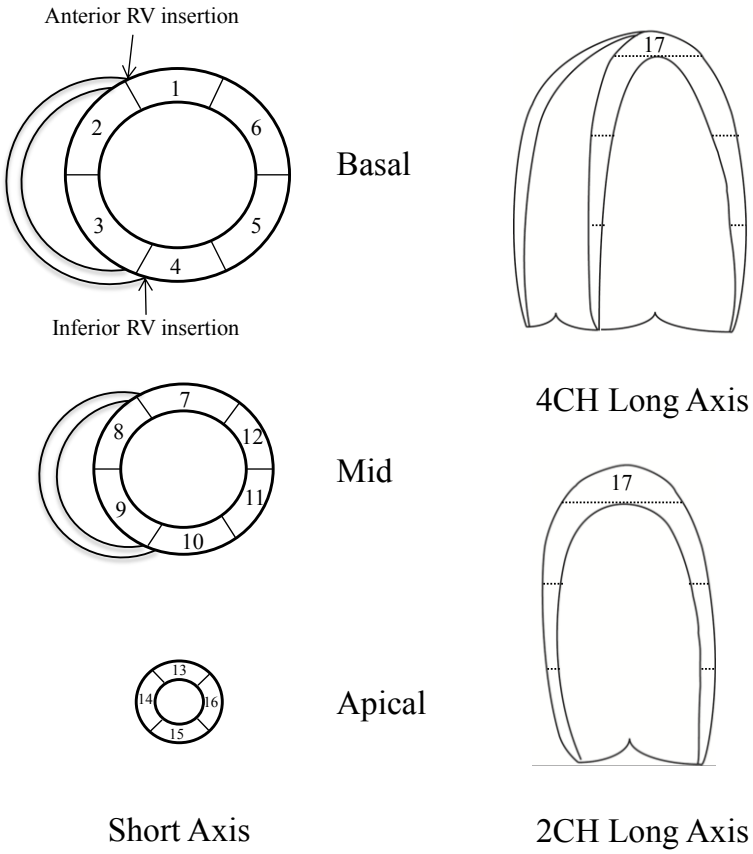

Figure 1.6 Coronary artery territories

Basal segments: 1. Basal anterior; 2. Basal anteroseptal; 3. Basal inferoseptal; 4. Basal inferior; 5. Basal inferolateral; 6. Basal anterolateral;
Mid-cavity segments: 7. Mid anterior; 8. Mid anteroseptal; 9. Mid inferoseptal; 10. Mid inferior; 11. Mid inferolateral; 12. Mid anterolateral;
Apical segments: 13. Apical anterior; 14. Apical septal; 15. Apical inferior; 16. Apical lateral; 17. Apex.

1.5 Content of the Following Chapters

The content of this dissertation is as follows. Chapter 2 presents the study that evaluates the roles of the alterations in the changes in LV volume and geometry in achieving elevated stroke volume in endurance athletes' hearts (marathon runners) and a group of patients with chronic compensated MR. Chapter 3 describes the study that further evaluates the important role that volumetric analysis plays in the determination of severity of MR. Chapter 4 proposes a novel

biventricular active mesh model as well as its implementation. Chapter 5 concludes the work described in earlier chapters.

CHAPTER 2 VENTRICULAR STRUCTURAL REMODELING IN MARATHONERS

The need for accurate assessment of the LV and RV geometric remodeling has become urgent for cardiac diseases, such as mitral regurgitation and pulmonary hypertension. In fact, from our observation of patients with chronic isolated mitral regurgitation, their LV at end-systole (ES) remodels extensively at the apex, manifested by a dilated apex. This has significantly contributed to the increase of the LV ES volume before the changes in LV dimension can be detected. As a result, traditional determination factors of timing for surgery (i.e. LV ejection fraction > 60% and/or LV ES dimension ≤ 40mm [12] measuring at the tip of the papillary muscle) may not be sufficient.

To further assess the importance of apex remodeling in evaluation of cardiac diseases and its significant clinical application, two preliminary clinical studies were conducted. This chapter will introduce the first study which involves the evaluation of the difference in cardiac geometry and function of patients with chronic, compensated MR versus marathon runners, who represent pathologic and physiologic volume overload, respectively. An abstract of this work was accepted by the 2011 American College of Cardiology [14]. The manuscript of this work is ready for submission. My contribution to this work includes conceiving and designing the research hypothesis with Dr. Louis Dell'Italia, generating and/or acquiring study data, analyzing the data using various statistical models, interpreting the data, describing results and conclusions.

2.1 Introduction

Marathoners experience numerous skeletal muscle, pulmonary, and cardiac adaptations in response to endurance training [15-17]. The cardiac remodeling is characterized by commensurate increases in left ventricle (LV) volume and mass that result in an increased stroke volume (SV) [18]. This eccentric cardiac hypertrophy is a putative adaptation to endurance training that is generally thought to enhance physiologic reserve capacity. However, during a marathon run, cardiac troponin T release can reach levels typically diagnostic for acute myocardial infarction [10], particularly in less experienced runners [19], which has raised questions regarding the long-term effects of these repeated events of myocardial damage. In addition, there is controversy regarding the potential pathological consequences of cardiac enlargement among endurance athletes, or the "athlete's heart" [20, 21].

Chronic compensated mitral regurgitation (MR) represents another form of cardiac enlargement manifested by eccentric LV remodeling. Both conditions are associated with an increase in LVSV, which in MR is facilitated by regurgitation through a secondary ejection pathway into the left atrium, while the marathon heart ejects into a relatively compliant vascular bed [22, 23]. Previous studies have utilized echocardiography or cMR to report elevated LV dimensions and/or volumes in both MR and marathoners, respectively [24-28]. These two conditions have also been compared and distinguished by their biochemical and molecular signaling mechanisms [29]. However, changes in LV geometry and mechanics in the marathoners differ from a pathologic form of volume overload.

The question of the "appropriateness or suitability" of cardiac enlargement in the athlete's heart is frequently raised in the athlete who presents for evaluation of an enlarged heart. One of the major factors in defining a physiologic response to a chronic hemodynamic stress is the

adherence to an elliptical LV shape, as opposed to an increase in LV sphericity, which can cause increases in wall stress and myocardial oxygen demand and result in a decrease in LV function or sudden death [24]. A more detailed analysis that defines the deviation from elliptical shape and the effects on maximum shortening and LV twist can uncover important insights into the different consequences of eccentric cardiac hypertrophy due to volume overload. Thus, in the current investigation, we utilize cMR to generate precise three-dimensional (3D) measurements of cardiac geometry and mechanics in comparing LV remodeling in marathoner and chronic MR patients.

2.2 Material and Methods

2.2.1 Study Population

Nineteen marathoners (39±10 years; 47% female), 17 MR patients (46±5 years; 53% female) and 24 control subjects (45±8 years; 50% female) comprised the study population. The control subjects and the marathoners had no history of cardiovascular disease and were not using any prescription medication. Control subjects were not engaged in any aerobic training, with only varying degrees of recreational activities. Marathoner designation was based upon having run 4 full marathons over the prior two years and running an average of 50 miles per week. Chronic isolated MR was defined as at least moderate severity with LV ejection fraction (EF) > 60% based on echocardiogram results in the absence of symptoms or obstructive coronary artery diseases by exercise testing with nuclear perfusion. The study protocol was approved by the University of Alabama at Birmingham Institutional Review Board, and all participants gave written informed content.

2.2.2 cMR

All participants underwent cMR on a 1.5T scanner (Signa, GE Healthcare, Milwaukee, Wisconsin) optimized for cardiac imaging. Electrocardiographically gated, breath-hold, segmented k-space steady state free precession technique was used to obtain cine images with standard (2-, 3- and 4- Chamber, and Short-axis) views using the following typical parameters: field of view 40 ×40 cm, image matrix 256 ×128, flip angle 45^0, repetition/echo times 4/1.8 ms, cardiac phases 20, slice thickness 8 mm without any slice gap.

Endocardial and epicardial contours were manually traced on cine cMR images acquired near end-diastole (ED) and end-systole (ES) by blinded assignment. Volumes were calculated from summated serial short axis volumes and indexed to body surface area (BSA) [24]. Three-dimensional geometric parameters were measured based on the contours using in-house developed software [24]. LV two-dimensional (2D) apex curvatures were computed from endocardial contours drawn on 4-chamber view images using standard formula [30]. Sphericity index was defined as the ratio of LV long-axis length to LV inner diameter [31]. Smaller sphericity index indicates greater sphericity.

Tagged cMR was acquired on the same scanner using the following typical parameters: repetition/echo times 8/4.2 ms, tag spacing 7 mm. Tag lines were tracked [32] and edited, if necessary, by expert users. LVES maximum shortening strain was computed at all wall segments [13] (excluding the apex) by fitting a B-Spline deformation model in prolate-spheroidal coordinates to the tag line data [33]. The reported LV maximum shortening was the average value of all wall segments (excluding the apex). Three-dimensional LVES twist, T, was computed as [34]:

$$T = (\varphi_{apex} - \varphi_{base}) \times (\rho_{apex} + \rho_{base}) / 2L$$

where φ is the LVES rotation angle, ρ is the epicardial radius and L is the distance between the basal and distal slices.

Two-dimensional twist was calculated using the formula above in each timeframe using improved HARP tracking [17], and 2D twist-time curve was constructed and differentiated with respect to time. LV peak early diastolic untwist velocity (^{0}/beat) was defined as the maximum negative derivative of the untwist angle during early diastole normalized to heart rate (HR) (absolute values were used in this study).

2.2.3 LV Work Rate

LV work rate (mmHg × L /min) was defined as follows [35, 36]

$$\text{LV work rate} = \text{LVSV} \times \text{LV-P}_{es} \times \text{HR} /1000$$

Where LV-P_{es} is the LVES pressure, which can be approximated by the mean LV systolic blood pressure P_{mean}, defined as follows:

$$\text{LV-P}_{es} \approx P_{mean} = \frac{2}{3} \times \text{systolic BP} + \frac{1}{3} \times \text{diastolic BP}$$

Both systolic and diastolic BPs were measured by sphygmomanometry with patients in the supine position immediately before and after cMR scanning. The reported systolic and diastolic BPs were the average of pre- and post-cMR scanning values.

2.2.4 Statistical Analysis

One-way analysis of variance (ANOVA) was used to compare groups for each continuous variable, such as LV end-diastolic volume (LVEDV), LV end-systolic volume (LVESV). The Generalized Wald test was performed to compare the categorical variable, percentage of female, among the three groups. Homogeneity of variance was tested using Levene's test. Appropriate data transformation was conducted if the homogeneity assumption was violated. Tukey-Kramer

procedure was performed to control the pairwise comparisons among the groups jointly in order to avoid erroneous Type I error rate inflation. Data are presented here as mean ± standard error (SE), except that age was presented as mean ± standard deviation (SD). A $P<0.05$ was considered statistically significant. All statistical analyses were performed using SAS version 9.2.

2.3 Results

2.3.1 Patient Demographics

The controls, marathoners and MR groups had matched age, percentage of female and body surface area (BSA) (Table 2.1). The marathoners had a lower resting heart rate vs. controls and MR. Both diastolic and systolic BPs did not differ among the three groups. LV work rate did not differ in the marathoners vs. controls while it was significantly higher in MR.

Table 2.1 Baseline Characteristics in Controls, Marathoners and MR

	Control (N=24)	Marathoner (N=19)	MR (N=17)
Age, year	45 ±8	39 ±10	46 ±5
% Females	50	47	53
BSA, m^2	1.91 ±0.17	1.78 ±0.23	1.90 ±0.20
Heart Rate, beats/min	67 ±11	55 ±9*	64 ±11†
Diastolic BP, mm Hg	77 ±9	73 ±10	75 ±9
Systolic BP, mm Hg	123 ±13	114 ±15	118 ±15
LV Work Rate, mm Hg × L/min	613 ±174	544 ±177	789 ±215*†

Values are n or mean ± std. MR: mitral regurgitation; BP: Blood Pressure; LV: Left Ventricle; * $P<0.05$ Marathoners vs. Control, MR vs. Controls; † $P<0.05$ MR vs. Marathoner

2.3.2 Ventricular Volumes

Marathoners and MR had ~ 35% greater LVEDV index (normalized to BSA) and ~ 50% higher LVESV index vs. controls, and LVSV index vs. controls (Table 2.2). LVEF did not differ among the groups. Marathoners had significantly greater LV mass/BSA vs. controls but did not differ between MR and controls. LV mass/volume ratio was significantly higher in MR group vs. controls (P=0.01) and marathoners (P=0.0097). Marathoners had commensurate increases in RVEDV, RVESV and RVSV indices vs. controls; while MR RV volumes did not differ from controls. RVEF was similar in all groups.

Table 2.2 Ventricular Volume and Mass

	Control (N=24)	Marathoner (N=19)	MR (N=17)
LV ED volume index, ml/m^2	69 ±10	92 ±15*	98 ±18*
LV ES volume index, ml/m^2	25 ±7	37 ±8*	36 ±8*
LV stroke volume index, ml/m^2	44 ±7	55 ±7*	62 ±14*
LV ejection fraction, %	65 ±7	60 ±4	63 ±6
LV mass index, gm	52 ±12	62 ±9*	58 ±10†
LV mass/volume, ml/gm	0.76 ±0.18	0.76 ±0.12	0.60 ±0.07*†
RV ED volume index, ml/m^2	72 ±11	104 ±13*	78 ±15†
RV ES volume index, ml/m^2	34 ±8	47 ±8*	35 ±8†
RV stroke volume index, ml/m^2	39 ±8	58 ±8*	43 ±10†
RV ejection fraction, %	54 ±8	55 ±5	55 ±7

Values are mean ± std. MR: mitral regurgitation; LV: Left Ventricle; RV: Right Ventricle; ED: end-diastolic; ES: end-systolic; * P<0.05 Marathoners vs. Controls, MR vs. Controls; † P <0.05 MR vs. Marathoner.

2.3.3 LV Global and Regional Geometry

As shown in Table 2.3, LVED and LVES diameters were significantly increased in MR and marathoners vs. controls, while LVES inner diameter did not differ in marathoners vs. controls (P=0.079).

Table 2.3 LV global geometry

	Control (N=24)	Marathoner (N=19)	MR (N=17)
LV ED diameter, mm	51 ±4	54 ±4*	59 ±4*†
LV ES diameter, mm	36 ±4	38 ±4	39 ±3*
LV ED length, mm	90 ±8	98 ±10*	89 ±10†
LV ES length, mm	71 ±8	76 ±9	67 ±10†
LV ED sphericity index	1.77 ±0.19	1.80 ±0.18	1.53 ±0.16*†
LV ES sphericity index	1.96 ±0.29	1.96 ±0.17	1.71 ±0.20*†
LV ED apex curvature, 1/cm	1.40 ±0.29	1.36 ±0.26	1.00 ±0.31*†
LV ES apex curvature, 1/cm	2.84 ±1.21	2.20 ±0.53	1.70 ±0.43*†

Values are mean ± std. MR: mitral regurgitation; LV: Left Ventricle; ED: End-Diastole; ES: End-Systole; * P<0.05 Marathoners vs. Controls, MR vs. Controls; † P <0.05 MR vs. Marathoners.

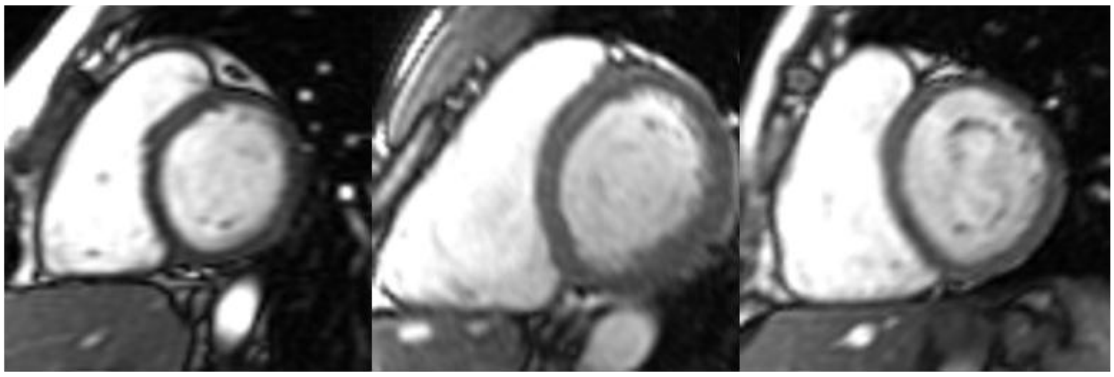

Control Marathoner MR

Figure 2.1 LV and RV cMR short-axis images

Images are taken basal slice just above the tip of the papillary muscle at end-diastole.The marathon and the MR patient have increased LV dimension vs. control. However, the RV size was proportionately increased in the marathoner but did not differ from control in the MR.

However, marathoners had significantly longer LVED and LVES lengths vs. MR. Therefore, marathoners had normal sphericity indices, while MR hearts were more spherical. MR also had significantly lower apex curvatures at both LV ED and ES vs. marathoners and controls, as demonstrated in Figures 2.1 and 2.2.

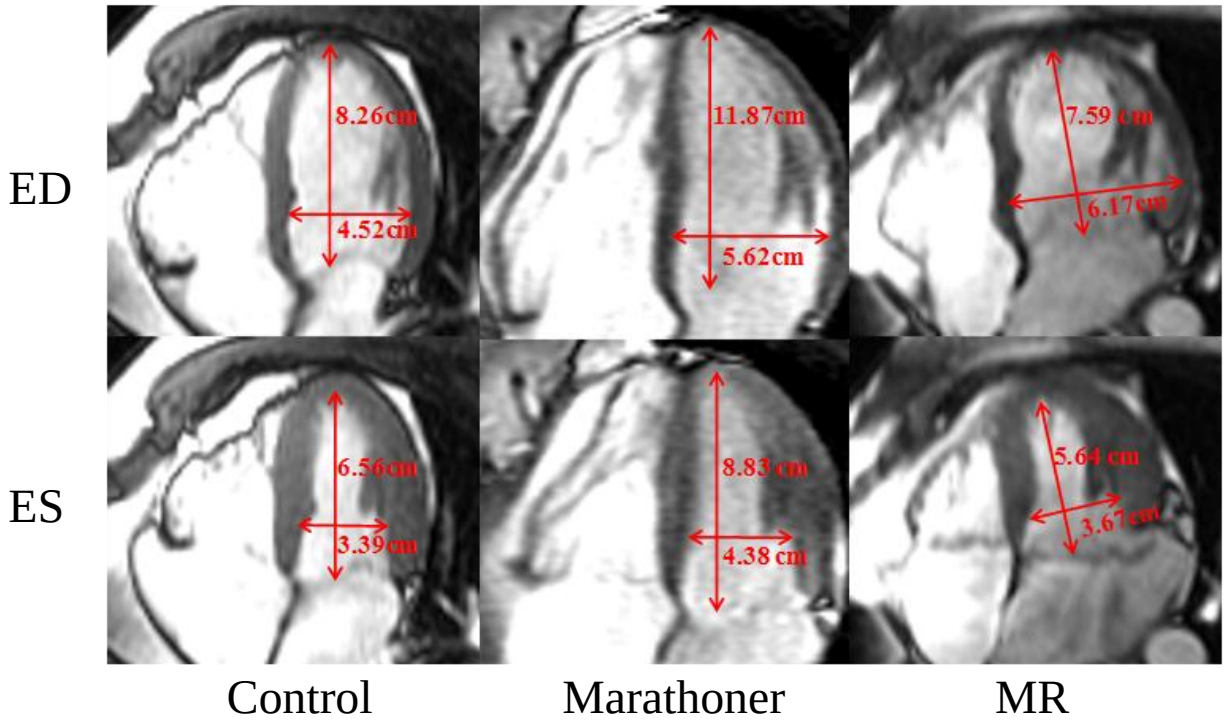

Figure 2.2 LV and RV cMR long-axis images
As opposed to the MR heart, the marathoner's heart has a proportionate increase in both LV and RV lengths and transverse dimensions.

Figure 2.3 shows that LVED and LVES R/T ratios were significantly increased in MR vs. control; while LVES R/T ratio was significantly increased in marathoners vs. controls. LV wall thickness remained normal in the marathoner group; while it was significantly decreased in MR from mid to distal LV vs. controls.

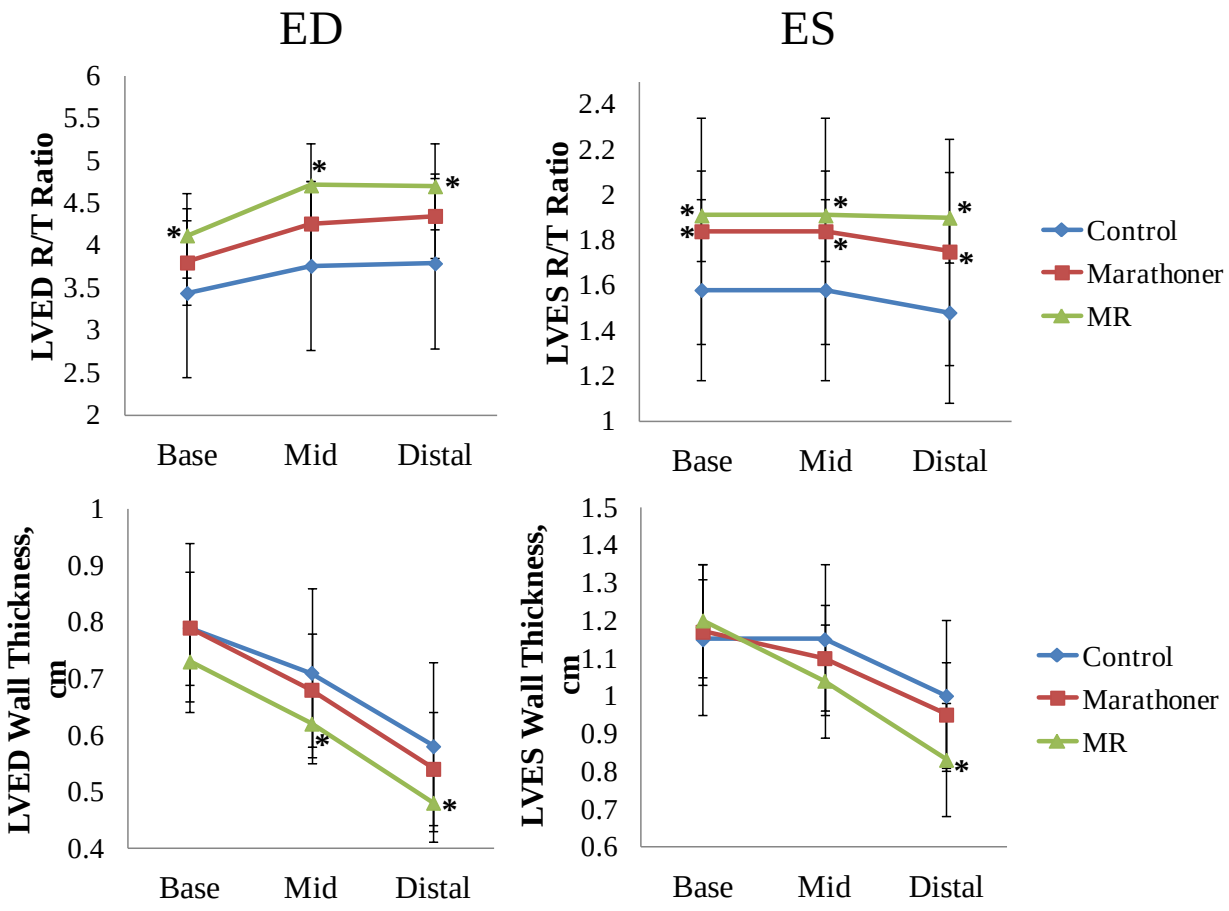

Figure 2.3 Comparisons of LV ED and ES geometric remodeling

The MR group has significantly increased LVED and LVES R/T ratio, while the marathoners' R/T ratio is significantly increased only at ES. The MR group also demonstrates significantly decreased wall thickness at both ED and ES, while the wall thickness remains normal in the marathoners' group. *: P<0.05 Marathoners vs. Controls, MR vs. Controls.

2.3.4 LV Strains Indices

LVES maximum shortening strain did not differ among all groups. LVES twist angle was significantly decreased in marathoner vs. MR and controls (Table 2.4).

Figure 2.4 illustrates the differences in LVES twist among three groups using a 3D color map. This figure demonstrates an overall brighter color (larger twist angle) in the MR vs. dimmer

color (smaller angle) in the marathoner. LV peak early diastolic untwist velocity normalized to HR was not significantly different among all groups (Table 2.4).

Table 2.4 LV Strain parameters

	Control (N=24)	Marathoner (N=19)	MR (N=17)
LV ejection fraction, %	65±7	60±4	63±6
LV ES maximum shortening, %	20.66±2.19	19.48±1.46	21.08±2.42
LV ES twist, ^{0}	4.49±1.01	3.67±1.04*	4.65±0.93†
Peak early diastolic untwist velocity, ^{0}/beat	32±9	27±9	30±13

Values are mean ± std. MR: mitral regurgitation; LV: Left Ventricle; ES: End-Systole; E: mitral valve peak velocity in early diastole; A: mitral valve peak velocity in late diastole; * P<0.05 Marathoners vs. Controls, MR vs. Controls; † P <0.05 MR vs. Marathoners.

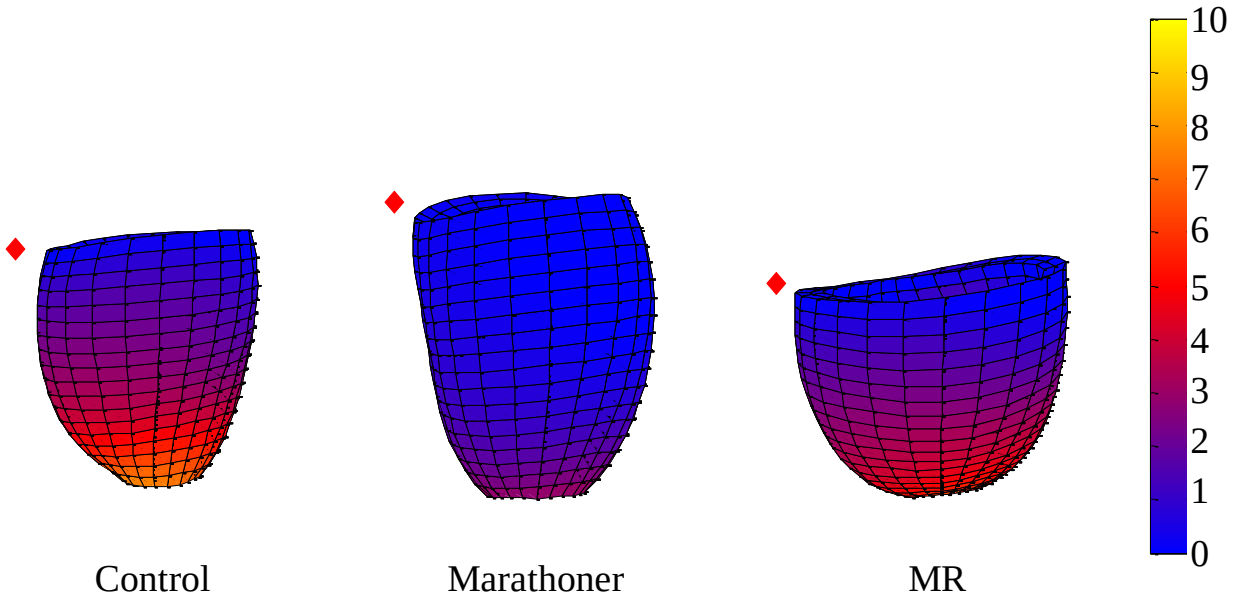

Figure 2.4 LVES twist of three representatives of control, marathoner and MR
The graphic displays LVES twist angle using a color map (range from 0^0 to 10^0). Twist angle in the marathoner's heart is significantly less compared with both control and MR. (red diamond: mid septum)

2.4 Discussion and Conclusions

This work represents the first study to compare 3D LV geometric remodeling and mechanics in marathoners versus chronic compensated MR utilizing cMR and 3D data analysis. In the setting of similar increases in LV volumes and stroke volume, marathoners' hearts maintain a normal LV sphericity and normal wall thickness with lower LV twist, while there is a greater global and regional LV sphericity in the MR hearts.

Marathoners' hearts have lower resting HR, which has been attributed to a higher vagal tone [37]. The 29% regurgitant fraction in MR patients translates into a decrease in forward cardiac output. Thus, excessive adrenergic drive as well as local neurohormonal factors may influence the more spherical remodeling in the MR heart that is not be detected by LV volumes or the commonly reported LVES dimension measured by conventional echocardiography at the tips of the papillary muscles. Further, the marathoner's heart has normal LV wall thickness and mass/volume, which is decreased in MR, along with greater LV sphericity and smaller LV apex curvature at both ED and ES. Taken together, the marathoner's heart maintains the normal elliptical shape with a proportionately higher LV mass, while the MR heart undergoes adverse eccentric remodeling that has been reported to be associated with abnormal extracellular matrix loss along with cardiomyocyte thinning and elongation [38].

The results of the current investigation suggest that cMR-derived indices of 3D geometry provide important insight into the constant as opposed to the intermittent volume stimulus of MR versus marathon runners. Of particular interest, the more spherical LV apex and normal LV length in MR, as opposed to the greater long axis length of the marathoner's heart, lead to loss of an elliptical shape, which is preserved in the marathoners. In addition, the marathoner's heart undergoes parallel increases in RVED and RVES volume indices. Thus, the entire marathoner's

heart is enlarged and elongated, in contrast to the more spherical MR hearts especially at in the distal LV segments and apex.

In the marathoner's hearts during rest, the higher LVESV index has preserved LV wall thickness and LV elliptical shape, which is consistent with an appropriate compensatory increase in LV mass. Despite the smaller ES twist at rest, the marathoner's heart achieves normal LVEF and peak early diastolic untwist velocity through normal maximum shortening. It is of interest that a recent report shows that endurance exercise training is associated with a significant increase in LV twist mechanics during exercise [39].Taken together, the physiological and architectural findings herein support the concept that by adapting to high volume endurance training, marathoners' hearts meet resting cardiac output requirements by operating at a slightly lower percentage of maximum twist capacity vs. controls. This low-demand resting state may be a result of higher resting vagal tone and thus may allow for a greater physiological reserve during the demand of extreme endurance exercise.

The comparison of the marathoners and MR hearts is limited in that the marathoner heart ejects into the high pressure aorta, especially during exercise, while the MR heart ejects into the low pressure left atrium. In patients with aortic regurgitation, in which the excess LV volume ejected into the high pressure aorta, the LV maintains a more elliptical or even conical shape compared to the hearts of MR patients and normal subjects [40]. Nevertheless, the MR heart maintains normal or supranormal ejection indices despite adverse spherical LV remodeling compared to the elliptically-shaped marathoner's heart. Thus, in the evaluation of an "enlarged heart" of an athlete, the assessment of 3D geometry may represent an important tool in determining physiologic vs. pathologic increases in LV volumes.

CHAPTER 3 MAGNETIC RESONANCE IMAGING WITH THREE-DIMENSIONAL ANALYSIS REVEALS IMPORTANT LEFT VENTRICULAR END-SYSTOLIC REMODELING IN ISOLATED MITRAL REGURGITATION

This study was conducted to evaluate the important role that apex remodeling played in the progression of the severity of mitral regurgitation and its significance as an indicator for timing of surgery. An abstract of this work was accepted to the 2011 Science Section of American Heart Association [41]. The manuscript of this work was accepted by *Circulation* [42]. My contribution to this work includes conceiving and designing the research idea with Dr. Louis Dell'Italia and Dr. Mustafa Ahmed, acquiring patients' clinical data, generating patients' cMR data, analyzing the data using various statistical models, interpreting the data, describing results and conclusions, corresponding to the Statistical Reviewer's questions.

3.1 Introduction

Mitral regurgitation (MR) is a frequent form of valvular disease, representing an important public health burden in the US. An estimated 2–2.5 million people were affected in the year 2000, a number expected to double by 2030 due to population growth and aging [43-45]. Isolated MR from myxomatous degeneration of the mitral valve results in a relatively low pressure form of volume overload, due to excess volume being ejected through a secondary ejection pathway into left atrium. Forward cardia`c output in MR is preserved by an increase in left ventricular (LV) stroke volume, mediated by augmentation of LV preload (end-diastolic volume), decreased afterload due to the relatively low pressure ejection pathway in to the left

atrium, and an increase in adrenergic drive. These mechanisms may serve to preserve LV ejection fraction (EF), even in the face of increasing LV end-systolic (ES) dimension (D), volume and LVES wall stress over time. This may explain why despite adherence to current guideline recommendations[12, 46] post-operative LV dysfunction is not uncommon, and is associated with increased morbidity and mortality[24, 45].

The mechanisms involved in the transition to irreversible cardiomyocyte damage in chronic isolated MR remain elusive. This is compounded by the fact that symptoms of heart failure may be very subtle and LV function and geometry may change significantly in the absence of symptoms. Thus, the success of adherence to echocardiographic guidelines is limited by the requirement of very close surveillance, which has most likely contributed to the recent reports that patients with isolated MR are not receiving timely surgery, even with advances in surgical repair and minimally invasive surgery[47, 48]. Studies have reported a decrease in LVEF post mitral valve repair for isolated MR[45, 49-55], utilizing echocardiography with geometric assumptions based on LV dimensions for LVEF measurements. These findings have resulted in a body of evidence supporting recommendation for early surgery in the controversy regarding management of asymptomatic patients with severe MR [49, 56-58].

It is important to note that echocardiographic follow-up studies in MR have utilized the standard LVESD measured at the tips of the papillary muscles. We hypothesize that extensive LV apical remodeling in MR hearts, beyond the base and tips of the papillary muscles, contributes to an increasing LVES volume (LVESV) that is not appreciated by measuring the LVESD alone. Therefore, in the current investigation, we utilize cMR and three-dimensional (3D) data analysis to quantitate global and regional LV geometry and function in patients with isolated MR.

3.2 Methods

3.2.1 Study Population

Ninety-four patients with moderate to severe MR were recruited from June, 2005 to September, 2010 at the University of Alabama at Birmingham. All patients referred for surgery had LVEF>60% and almost all had LVESD <40mm by referral echocardiography studies, and need for surgery was based on conservative clinical judgment of the cardiologist and cardiovascular surgeon at the tertiary referral center. MR severity was documented qualitatively on echocardiogram/Doppler studies as well as quantitatively on cine and tagged cMR in all cases. All patients had coronary angiography before surgery to rule out significant coronary artery disease. Patients with evidence of significant aortic valve disease or concomitant mitral stenosis were excluded. Thirty-five patients with severe isolated MR (mitral regurgitant volume 57 ±34 ml, mitral regurgitant volume fraction 40 ±16 %) secondary to degenerative mitral valve disease were referred for corrective mitral valve (MV) surgery. All patients underwent cMR before surgery and 12 months after surgery. cMR was also performed in 51 control volunteers (mean age 44 ±14 years, median age 42 years, age range 20 to 70 years) who had no prior history of cardiovascular disease and were not taking any cardiovascular medications. The study protocol was approved by the Institutional Review Boards of University of Alabama at Birmingham and Auburn University. All participants gave written informed content.

3.2.2 Surgery

Thirty-five patients underwent MV repair while six patients underwent MV replacement. MV surgery was performed through a median sternotomy and employed standard hypothermic cardiopulmonary bypass and cold blood cardioplegia. MV replacement was performed using standard techniques. A variety of methods were used to repair the MV including leaflet resection,

chordal replacement, or a combination of each, and these patients had implantation of a flexible annuloplasty ring. The adequacy of repair was assessed by intraoperative transesophageal echocardiography. Only the thirty-five patients who underwent mitral valve repair were analyzed in this study.

3.2.3 Magnetic Resonance Imaging

Cine cMR

Cine cMR was performed on a 1.5-T MRI scanner (Signa, GE Healthcare, Milwaukee, Wisconsin) optimized for cardiac imaging. Electrocardiographically gated breath-hold steady-state free precision technique was used to obtain standard (2-, 3-, and 4-chamber long axis and serial parallel short-axis) views using the following typical parameters: slice thickness of the imaging planes 8 mm, field of view 40cm, scan matrix 256 × 128, flip angle 45 °, repetition/echo times 3.8/1.6 ms).

3D LV geometric parameters were measured from endocardial and epicardial contours manually traced on cine magnetic resonance images acquired near end-diastole (ED) and ES. The contours were traced to exclude the papillary muscles. The contours at ED and ES were then propagated to the rest of the timeframes using a dual propagation technique [59]. LV volumes were computed by summing up the volumes defined by the contours in each short axis slice multiplied by slice thickness. These volumes were referred to as measured volumes in the current study. LV volume-time curve was constructed and differentiated with respect to time to obtain the peak early filling rate [59].

The contour data at ED and ES were transformed to a coordinate system aligned along the long-axis of the LV and converted to a prolate spheroidal coordinate system as described previously[28]. The prolate spheroidal coordinate system has one radial coordinate (λ) and two

angular coordinates (μ, θ). Cubic B-spline surfaces, $\lambda_{endo}(\mu, \theta)$ and $\lambda_{epi}(\mu, \theta)$, were fit to the λ coordinates of the endocardial and epicardial contours for each time frame. Each surface used 12 control points in the circumferential direction (θ) and 10 control points in the longitudinal direction (μ). The control points of each surface were computed to minimize the following error function,

$$\epsilon = \sum_{k} [\lambda(\mu_k, \theta_k) - \lambda_k]^2 + \gamma S(\lambda)$$

where γ is a weight set to 0.1. The first term in the error function is the squared difference between the contour points, λ_k, and the corresponding surface points, $\lambda(\mu_k, \theta_k)$. The second term is a smoothing function, which penalizes the bending energy of the surface,

$$S(\lambda) = \int_{\Omega} \left(\frac{\partial^2 \lambda}{\partial \mu^2}\right)^2 + 2\left(\frac{\partial^2 \lambda}{\partial \mu \, \partial \theta}\right)^2 + \left(\frac{\partial^2 \lambda}{\partial \theta^2}\right)^2 d\Omega$$

where Ω is the domain of the surface. 3D endocardial circumferential curvatures were then computed using standard formulas [30] at the wall segments [13] as previously defined (excluding the apex).

Two-dimensional (2D) apex curvatures were computed as the average of apex curvatures calculated from endocardial contours drawn on 4-chamber view image and 2-chamber view image using standard formula [30]. Sphericity index was defined as the ratio of LV long-axis length to LV inner diameter [31].Smaller sphericity index indicates greater sphericity. 3D wall thickness was computed at all wall segments [13] (excluding the apex) by measuring the 3D distance from a point on the epicardial surface to the closest point on the endocardial surface along a line perpendicular to the epicardial surface. Radius of curvature to wall thickness ratio

(R/T) was computed by the reciprocal of the product of the endocardial circumferential curvature and 3D wall thickness.

Tagged cMR

Tagged cMR were acquired on the same scanner using the following typical parameters: repetition/echo times 8/4.2 ms, tag spacing 7 mm, trigger time 10 ms from R wave, flip angle 10^0 and temporal resolution ~80 ms. Tag lines were tracked[32] and edited, if necessary, by expert users. LVES maximum shortening strain was computed at all wall segments (excluding the apex) by fitting a B-Spline deformation model in prolate-spheroidal coordinates to the tag line data[33].

3.2.4 Bullet Formula

LVESV (ml) was also calculated based on LVESD (mm) and LVES length (cm) using the Bullet formula [60, 61] as following,

$$\text{LVESV} = 0.83 \times \pi \times \left(\frac{\text{LVESD}}{20}\right)^2 \times \text{L}$$

where L is the length of LV measured from apex to the tip of the papillary muscle. This volume was referred to as calculated volume in the current study.

3.2.5 Statistical Analysis

Student's two sample t test (for continuous variables) and Fisher's exact test (for categorical variables) were conducted to compare the control group (n=51) and the MR group (n=94) in demographic (such as systolic blood pressure), geometric (such LVEDV, LVESV) and functional variables (such as peak early filling rate).

Regression analyses between LVESV and LVESD were performed in controls and MR. Model adequacy checking showed that the model was not linear for either groups. Therefore, square root transformation was performed to the control group which eliminated the non-

linearity problem. For the MR group, square root transformation did not resolve the non-linearity problem. Thus, cubic root transformation was performed with which the test showed proof of linearity of the model. Student's pair t test was performed to compare the measured LVESV by summing up the volumes defined by contours multiplied by slice thickness versus calculated LVESV by the Bullet formula. Correlation analysis was also performed to test the association between the difference of measured and calculated LVESV and 3D distal LV circumferential curvature.

One-way analysis of variance (ANOVA) was used to perform group-wise comparisons among controls and MRs with LVESD < and ≥37mm (corresponding to > mean + 1 standard deviation of LVESD of the control group; moreover, mean LVESD in the MR group is equal to 37mm). The P values of all pair-wise differences were adjusted using the Tukey-Kramer procedure.

Comparisons of the cMR variables among controls and MR before and 12 months after surgery were performed using a mixed model via PROC MIXED. The repeated measures of the MR patients before and after surgery were accounted for by an assumed compound symmetry correlation structure. To avoid inflating the probability of a Type I error, the Bonferroni-Holm step-down test procedure was utilized to adjust the significance level accordingly.

Model adequacy checking was performed for all models. Linearity was checked by plotting the model residuals versus the dependent variable to look for any curve band or nonlinear pattern. Shapiro-Wilk test was performed for normality test. Log transformation, square root or cubic root transformation were performed if there were outliers, if the normality assumption was not valid, or if the homogeneity assumption was violated as appropriate. If the data transformation could not resolve the outlier problem, Wilcoxon's rank-sum test (for two

groups' comparison) or Kruskal-Wallis test (for more than two groups' comparison) was performed.

Barnard's test [62, 63] was used to compare the post-operative incidence of LV dysfunction (defined as LVEF<50%) in patients with pre-operative LVESD <37mm vs. patients with pre-operative LVESD ≥ 37mm.

All data were presented as mean ± standard deviation (SD). A $P<0.05$ was considered statistically significant. We also conducted a general linear model for LV functional parameters to adjust for age and systolic BP using analysis of covariance. Age and systolic BP were considered as covariates. All statistical analyses were performed using SAS version 9.2.

3.3 Result

3.3.1 Clinical Characteristics

Clinical and cMR characteristics of the control subjects and 94 MR patients are outlined in Table 3.1. The two groups had a similar age range (20-70 and 25-76 years, respectively). However, the MR group was significantly older than the control. There were no significant differences in body surface area (BSA) and gender between the two groups. Heart rate, systolic and diastolic blood pressures (BP) were also similar in the two groups.

Table 3.1 Baseline demographic and cMR characteristics of controls and MR patients

	Control (n=51)	MR (n=94)
Age, year	44 ±14	54 ±11*
Age range, year	20-70	25-76
% Female	53	38
Body Surface Area, m^2	1.91 ±0.24	1.92 ±0.22
Heart rate, beats/min	67 ±12	68 ±11
Systolic BP, mm Hg†	118 ±13	124 ±15
Diastolic BP, mm Hg†	75 ±10	76 ±9
LVEDV index, ml/m^2†	69 ±10	105 ±24*
LVESV index, ml/m^2†	25 ±6	41 ±13*
LVSV index, ml/m^2†	44 ±7	64 ±16*
LVEF, %	64 ±6	61 ±7*
LVED dimension, mm	49 ±4	58 ±6*
LVES dimension, mm†	32 ±4	37 ±6*
LVED length, cm	8.82 ±0.81	8.99 ±0.91
LVES length, cm	6.82 ±0.86	6.93 ±0.82
LV ED Mass index, g†	50 ±10	64 ±17*
LVEDV/Mass, ml/g†	1.45 ±0.38	1.68 ±0.34*
Peak early filling rate, ml/sec†	378 ±110	518 ±240*

Values are mean ±SD. BP: blood pressure; LV: left ventricle; EDV: end-diastolic volume; ESV: end-systolic volume; EF: ejection fraction; *: $P < 0.05$ MR vs. controls; †: log transformation was performed.

3.3.2 cMR-Derived Variables in Controls and MR Patients

As expected, MR patients had significant increases in LVEDV, LVESV, and LV stroke volume (SV) indices (volumes normalized to BSA), as well as higher LVED and LVES dimensions compared to controls. However, there was no difference in LV lengths at both ED and ES in MR patients vs. controls. cMR-derived LVEF was significantly different between the two groups. LV mass index and LVEDV/mass ratio were significantly increased in MR vs. controls. Peak early filling rate was significantly higher in MR group vs. controls ($P < 0.0001$). Figure 3.1 (A) shows two representative examples from a control subject and a MR patient. Both hearts had the same LVESD (37mm) and similar LVES length; however, the MR LV had marked spherical remodeling demonstrated by the color coded circumferential curvature grid from base to distal LV depicted by lesser circumferential curvature (red) in the MR and greater circumferential curvature in the control (yellow). The LVESV of the MR heart was 85ml and that of the normal heart was 49ml. Figure 3.1 (B) demonstrates LV remodeling in MR as compared to control.

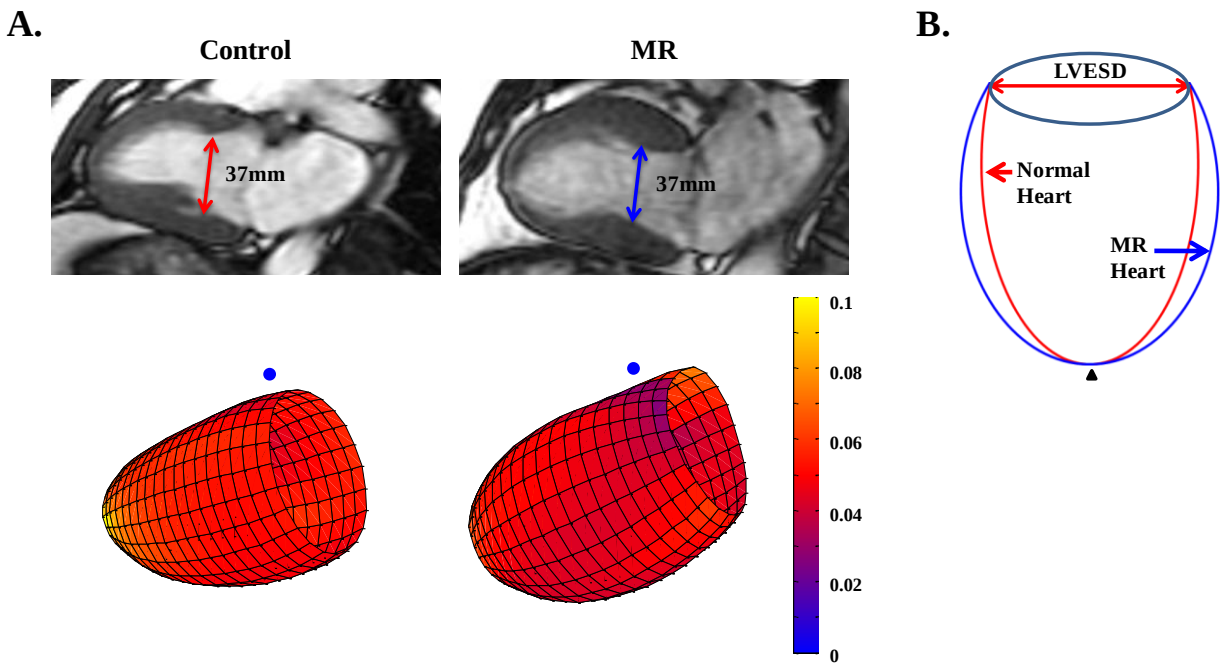

Figure 3.1 Description of MR LV remodeling

(A) Representative LV end-systolic (ES) with two chamber view (top row) and 3-dimensional surface representations (bottom row) using color scales of LVES endocardial surface circumferential curvature (1/mm) from a control subject and a MR patient; **(B)** Systematic simulation of MR LV remodeling with respect to control. The MR heart has the same LVES dimension and similar long axis length as control. However, there is lesser curvature from the mid to distal LV segments represented by a dimmer red color in the MR patient vs. control (brigher yellow color). These changes in the MR patient contribute to a more spherical LV remodeling and a larger LVES volume. Blue dot: mid-septum; black triangle: apex.

Figure 3.2 demonstrates the relation between LVESV and LVESD in the MR (A) and control groups (B). In the MR group, this relation was cubic ($LVESV = (2+0.06\times LVESD)^3$, $P<0.0001$) whereas this relation was quadratic in controls ($LVESV = (2.68+0.12\times LVESD)^2$, $P<0.001$). Of particular interest, LVESV calculated based on LVESD using the Bullet formula demonstrated no significant difference from the measured LVESV by summing the serial short axis images in controls. However, the Bullet formula significantly underestimated LVESV in the MR group. This difference between the measured LVESV and the calculated LVESV in MR was

significantly negative-correlated with the 3D circumferential curvature at distal LV (ρ=-0.25, P=0.01), as shown in Figure 3.2 (C).

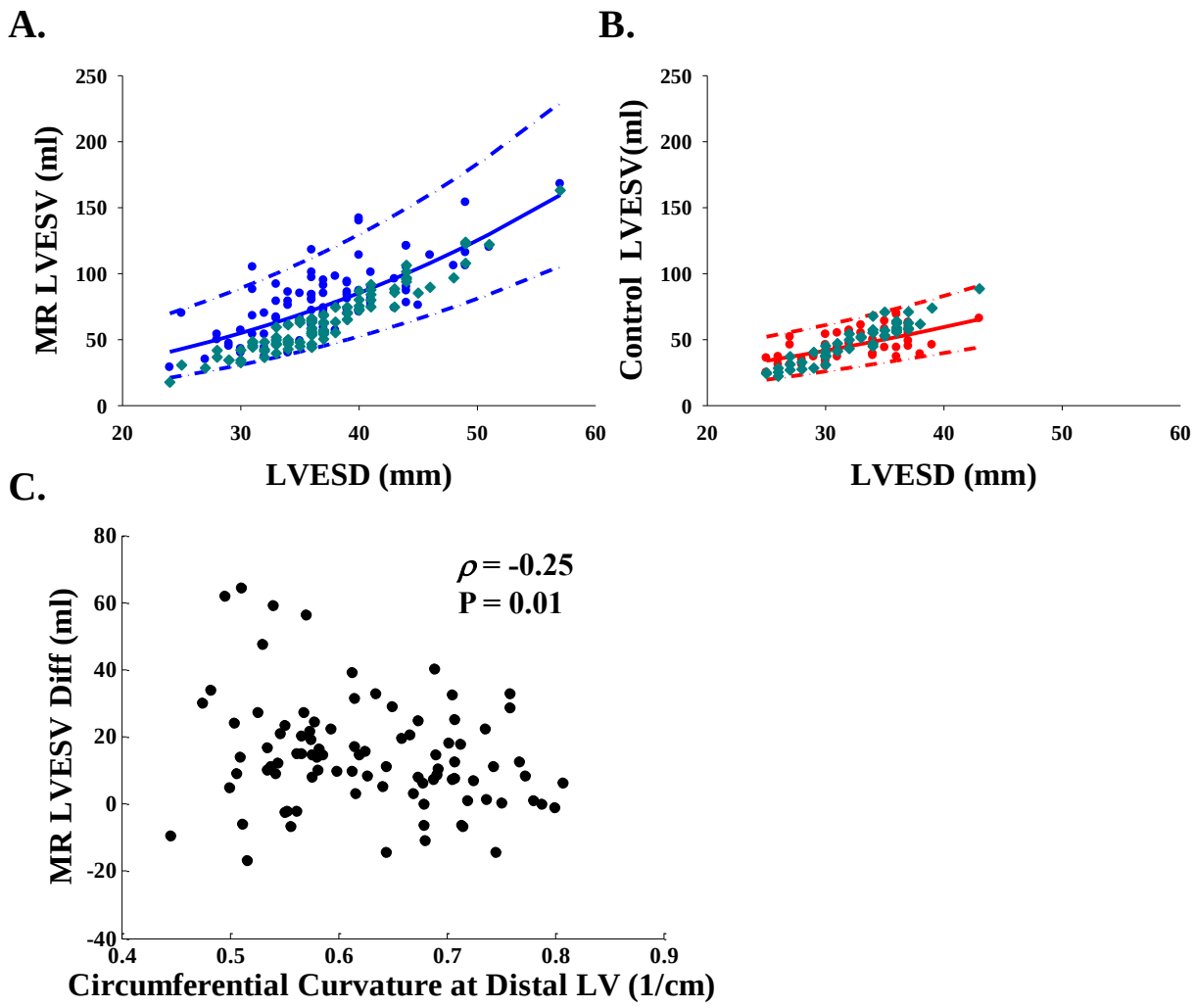

Figure 3.2 Correlation between LVESV and LVESD

The solid lines represent the fitted model for the LVESD vs. LVESV relation with 95% confidence intervals (dash lines), which is cubic in MR patients (n=94) and quadratic in controls (n =51). Data of calculated LVESV using the Bullet formula are shown as dark cyan points in (A) and (B). The difference between the measured LVESV from summated short axis images and calculated LVESV from Bullet formula in MR were plotted in **(C)** vs. LVES circumferential curvature at distal LV with correlation analysis result.

3.3.3 Effect of LVESD on Baseline LV Geometry and Function

All 94 MR patients were divided into two groups: 1) LVESD <37 mm, n=48 and 2) LVESD ≥37mm, n=46. The cut-off LVESD of 37mm was selected corresponding to > mean + 1 standard deviation of LVESD of the control group; Moreover, the mean LVESD of MR was equal to 37mm. Table 3.2 shows the comparisons between controls, and the two MR groups in LVES length, volume, global and 2D apical sphericity. With LVESD < 37mm, there was no increase in length; however, LVESV, LV global and 2D apical sphericity were significantly higher than controls. With LVESD ≥37mm, LVESV was further increased while the apex curvature remained similarly lower than controls; with no commensurate increase in LV length, LV global sphericity was further increased.

Table 3.2 LV Geometry in MR patients with LVESD < 37 mm and ≥ 37 mm

	Control (n=51)	MR	
		LVESD<37mm (n=48)	LVESD≥37mm (n=46)
LVES length, cm	6.81±0.86	6.73±0.87	7.14±0.69†
LVES sphericity index	1.95±0.26	1.82±0.23*	1.64±0.21*†
LVES volume index, ml/m^2	25±6	34±9*	48±13*†
2D LV apex curvature, 1/cm‡	2.93±1.13	1.89±0.48*	1.84±1.54*

Values are mean±SD. *: P<0.05 MR patients with LVESD<37 mm vs. Controls, MR patients with LVESD≥37 mm vs. Controls; †: P<0.05 MR patients with LVESD≥37 mm vs. MR patients with LVESD<37 mm; ‡: log transformation was performed.

Figure 3.3 demonstrates the differences in 3D LV geometry, and maximum shortening from base, mid, and distal LV at ED and ES among controls, MR with LVESD< and ≥37mm.

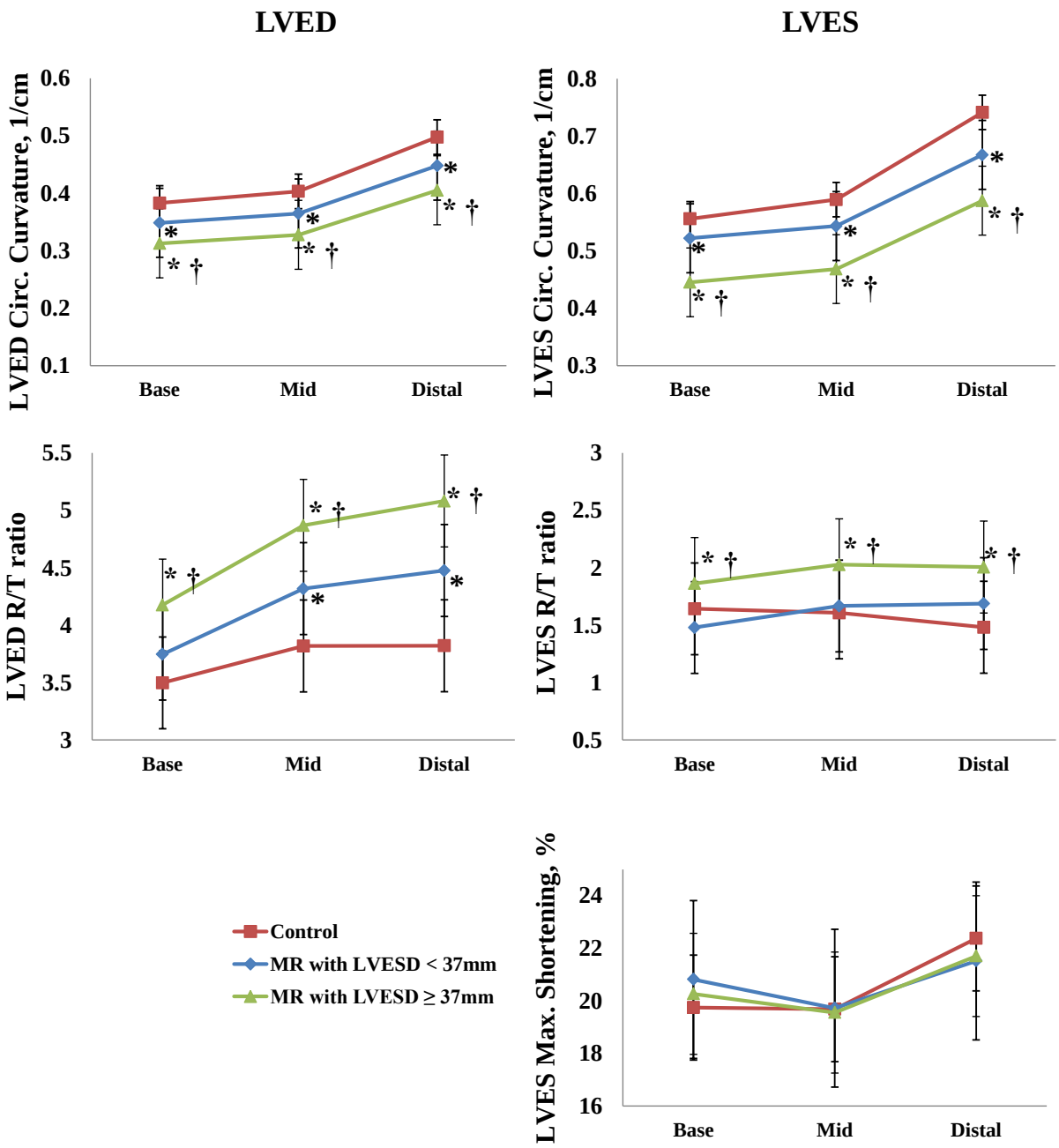

Figure 3.3 Comparisons of geometry and shortening in controls vs. MR

Three-dimensional LVED (left column) and LVES (right column) geometry with maximum shortening in the controls (n=51) and MR patients (n=94) divided into those with LVESD <37 mm and LVESD ≥37 mm. These data demonstrate progressive global LVED and LVES remodeling in both groups of MR patients compared to controls. However, LV maximum shortening remains normal or even supra-normal in both MR groups. *: P<0.05 MR with LVESD<37mm vs. Controls, MR with LVESD≥37mm vs. Controls; †: P<0.05 MR with LVESD≥37mm vs. MR patients with pre-operative LVESD<37 mm. Base, basal segment of the heart; Mid, middle segment of the heart; Distal, distal apex segment of the heart.

In the MR patients, LVED circumferential curvature decreased and R/T ratio increased from base to distal LV vs. controls. These changes were more significant in MR ESD≥37mm than in MR ESD<37mm. In MR patients with LVESD ≥37mm, LVES circumferential curvature was significantly lower at LV base (0.44±0.04), mid (0.47±0.05), and distal LV (0.59±0.08) compared with MR ESD <37mm and controls (P<0.0001 for base, mid and distal LV). LVES R/T ratio was significantly increased in MR ESD ≥37mm (1.86±0.4 at base, 2.03±0.4 at mid and 2.01±0.5 at distal LV) compared with both MR ESD <37mm (1.48±0.3 at base, 1.67±0.4 at mid and 1.69±0.4 at distal LV, P<0.0001) and controls (1.64±0.4 at base, 1.61±0.4 at mid, 1.48±0.4 at distal LV, P<0.0001). However, in MR ESD<37mm, LVES R/T ratio did not differ from control at all segments. There were no significant differences among all three groups in LV maximum shortening strain after being adjusted for age and systolic BP.

3.3.4 LV Geometry and Function following MV repair

Table 3.3 shows the clinical characteristics of controls, pre-operative MR, and 12 months post-operative MR patients. The mean age of the surgical MR group was significantly higher and the percentage of females was significantly smaller in MR group vs. controls. Therefore, comparisons of LV functional parameters among the groups were adjusted for an age effect. Controls and surgical MR patients before and after surgery had matched BSA, heart rate, systolic and diastolic BP. Before surgery, 20 patients were in New York Heart Association (NYHA) functional class I (57%), 14 patients were in NYHA class II (40%) and 1 patients were in NYHA class III (3%).

Table 3.3 Clinical characteristics of surgical patients with MV repair

	Control (n=51)	MR	
		Pre-operative (n=35)	Post-operative (n=35)
Age, year	44±14	53±11*	54±11*
% Female	53	20*	20*
Body surface area, m^2	1.9±0.24	2.00±0.24	1.98±0.23
Heart rate, beats/min	67±12	71±11	69±10
Systolic BP, mm Hg‡	118±13	124±15	121±11
Diastolic BP, mm Hg	75±10	78±8	76±10
LV ED volume index, ml/m^2‡	69±10	112±24*	80±18*†
LV ES volume index, ml/m^2‡	25±7	45±13*	38±14*†
LV SV volume index, ml/ m^2‡	44±7	67±16*	42±8†
LV EF, %	64±7	61±7*	54±8*†
LV ED dimension, mm‡	49±4	60±7*	51±6*†
LV ES dimension, mm‡	32±4	39±6*	36±7*†
LV ED mass index, g/m^2	50±10	67±14*	57±13*†
LV ED volume/mass, ml/g	1.45±0.38	1.70±0.35*	1.45±0.38†
LV ES R/T ratio‡	1.48±0.40	1.84±0.60*	1.78±0.68*
Peak early filling rate, ml/sec‡	378±110	632±270*	285±96*†

Values are n or mean±SD. BP: blood pressure; R/T ratio: radius /wall thickness measured at distal LV; *: P<0.05 pre-operative MR vs. Controls, post-operative MR vs. Controls; †: P<0.05 post-operative MR vs. pre-operative MR; ‡: log transformation was performed.

One year after the surgery, all but one patient were classified as NYHA class I while one was NYHA class II. LVED dimension, LVEDV index, LV mass index were significantly decreased post-operatively but remained greater than controls. LVEDV/mass returned to normal control level. Similarly, LVESD and LVESV index decreased post-operation but remained significantly greater than controls. Peak early filling rate was significantly increased prior to surgery and returned to normal level after surgery. LVEF was decreased post-operatively compared to both controls and pre-operative MR.

3.3.5 Recovery after Surgery in MR Patients with LVESD < and ≥ 37 mm

The 35 surgical MR patients who underwent mitral valve repair were divided into two groups based on pre-operative LVESD < or ≥37mm. Figures 4 and 5 demonstrate the recovery of LV geometry after surgery at ED (Figure 4) and ES (Figure 5) in the MR patients. In MR with pre-operative LVESD <37mm, LVED circumferential curvature was decreased prior to and returned to normal after surgery. LVES circumferential curvature was decreased near distal LV prior to and normalized after surgery. LVED R/T ratio was normal before and after surgery, while LVES R/T ratio at base was significantly below normal but recovered after surgery. In MR patients with LVESD≥37mm, LVED and LVES circumferential curvatures were decreased prior to and improved after surgery, but remained below normal at ES. In contrast, the LVED R/T ratio returned to normal while LVES R/T ratio remained above controls after surgery.
Figure 6 shows the change in maximum shortening after surgery in the MR patients with LVESD < and ≥37mm. Although in MR ESD<37mm, LVES R/T ratio did not differ from controls before and after surgery, maximum shortening was significantly decreased from mid to distal LV after surgery. In MR ESD≥37mm, LVES maximum shortening was decreased at all levels after surgery.

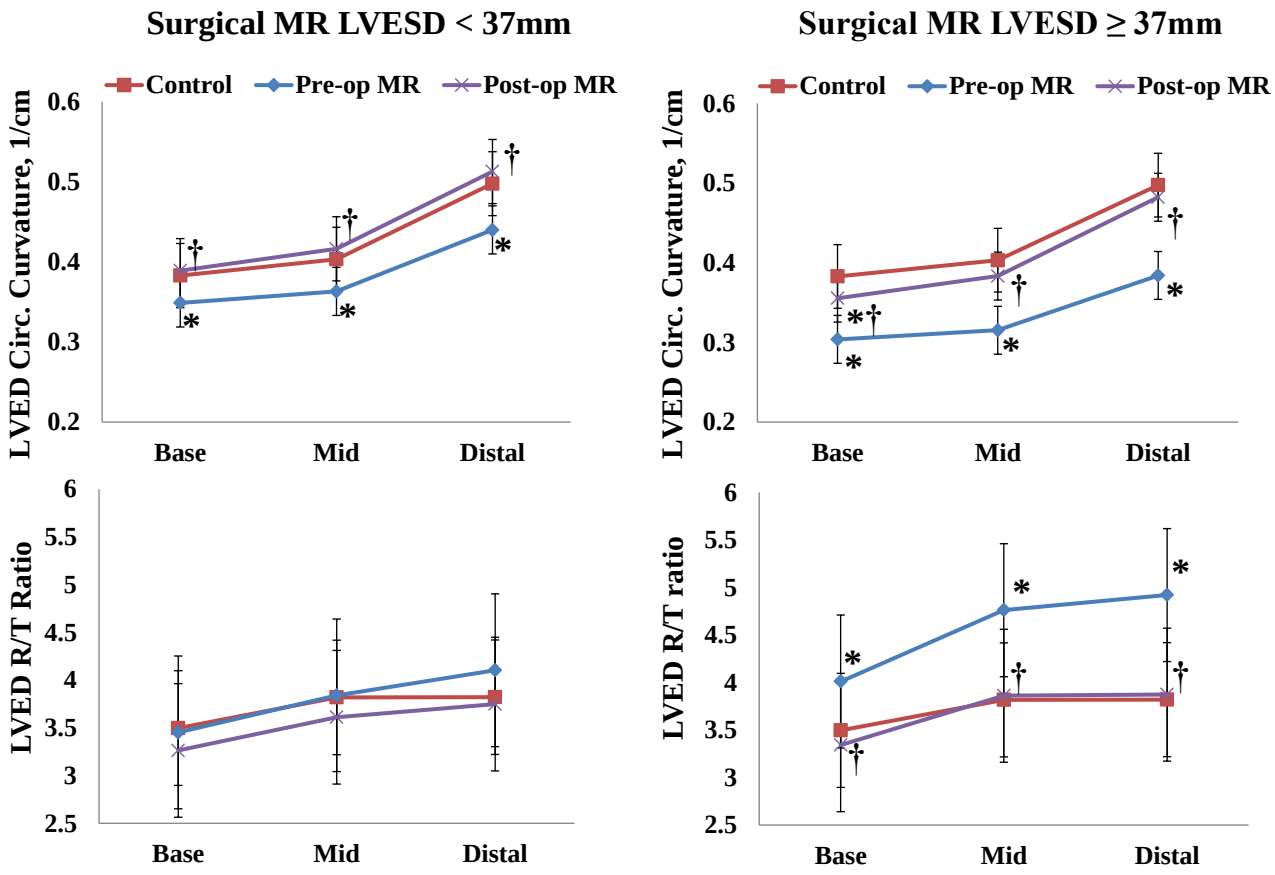

Figure 3.4 Comparisons of geometry in controls vs. surgical MR at ED

Comparison of LV end-diastolic (ED) geometric remodeling in controls and in surgical MR patients with pre-operative LVESD < and ≥ 37mm before and after surgery demonstrate progressive LV remodeling at ED in the two MR groups and their recovery after surgery. LVED R/T ratio is normalized after surgery in both MR groups. Circumferential curvatures in MR LVESD<37mm are normalized after surgery while in MR LVESD≥37mm, circumferential curvatures are increased yet not normalized. *: P<0.05 pre-operative MR vs. Controls, post-operative MR vs. Controls; †: P<0.05 post-operative MR vs. pre-operative MR.

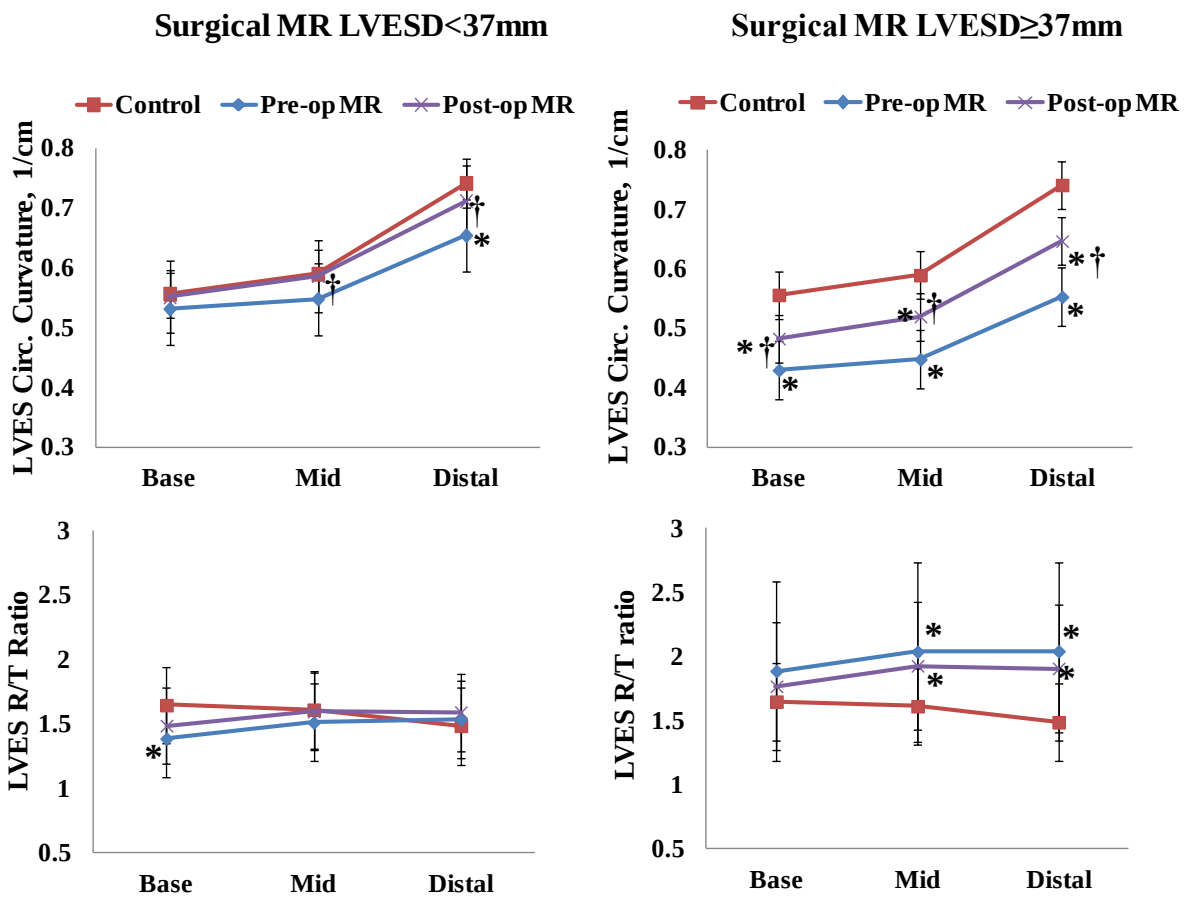

Figure 3.5 Comparisons of geometry in Controls vs. surgical MR at ES

Comparison of LV end-systolic (ES) geometric remodeling in controls and in surgical MR patients with pre-operative LVESD < and ≥ 37mm before and after surgery demonstrate progressive LV remodeling at ES that is not normalized after surgery in the MR patients with pre-operative LVESD ≥37mm, while it is normalized after surgery in MR patients with pre-operative LVESD <37mnm. *: P<0.05 pre-operative MR vs. Controls, post-operative MR vs. Controls; †: P<0.05 post-operative MR vs. pre-operative MR.

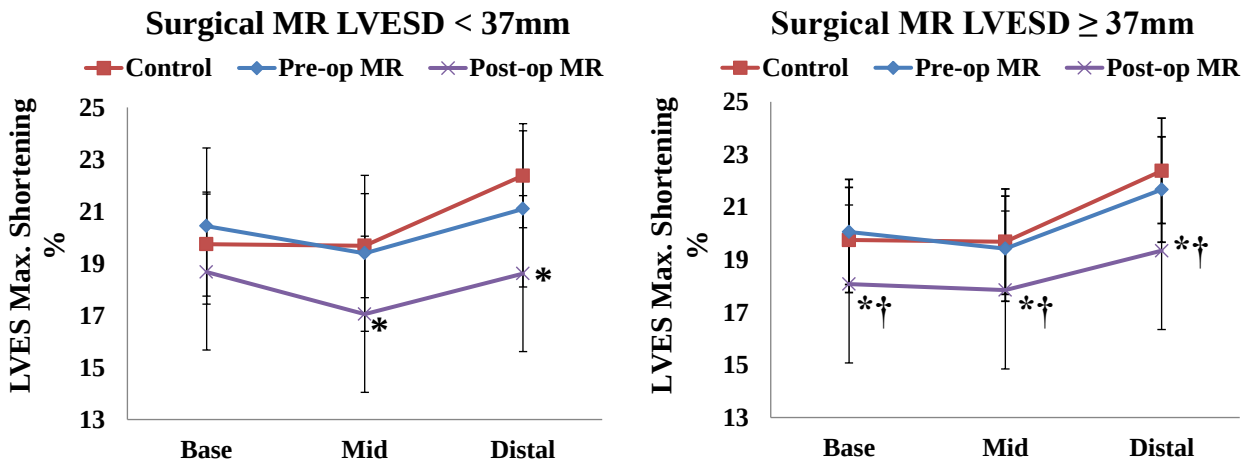

Figure 3.6 Comparisons of LVES maximum shortening in controls vs. surgical MR Comparison of LV end-systolic (ES) maximum shortening in controls and in surgical MR patients with pre-operative LVESD < and ≥ 37mm before and after surgery demonstrate that maximum shortening is decreased below normal in both groups of MR patients except that LVES maximum shortening is preserved at the base in patients with pre-operative LVESD <37 mm. *: P<0.05 pre-operative MR vs. Controls, post-operative MR vs. Controls; †: P<0.05 post-operative MR vs. pre-operative MR.

3.3.6 Incidence of Post-operative LV Dysfunction

Table 3.4 shows that among the 35 surgical MR patients, 11 patients (31%) had post-operative LV dysfunction (defined as LVEF<50%). Two of them had pre-operative LVESD <37mm while night of them had pre-operative LVESD≥37mm. The incidence of post-operative LV dysfunction in MR ESD<37mm (14%) was lower than that in MR ESD≥37mm (43%, P=0.0616). There were ten surgical MR patients in LVESD range of 37 to 40mm and two of them (20%) had post-operative LV dysfunction.

Table 3.4 Stratification of pre-operative LVESD for post-operative LV dysfunction

Post-operative	Pre-operative LVESD	
	<37 mm	≥37 mm
Total, n	14	21
LVEF<50%, n	2	9
Incidence of LV dysfunction, %	14%	43%*

*: P = 0.0616 MR patients with pre-operative LVESD ≥37mm vs. MR patients with pre-operative LVESD <37mm;

3.3.7 Supplementary Analysis

Although all patients in the current study had LVEF>60% and most of them had LVESD<40mm by referral echocardiography. However, using cMR based, 40% of patients have an LVEF < 60%. Therefore, to further emphasize the idea of this paper, supplementary analysis of patients that had cMR determined LVEF>60% are provided.

Table 3.5 Clinical characteristics of surgical patients with mitral valve repair and cMR-derived LVEF > 60% prior to surgery

	Control (n=51)	MR	
		Pre-operative (n=20)	Post-operative (n=20)
Age, year	44±14	54±8*	55±8*
% Female	53	15*	15*
Body surface area, m^2	1.9±0.24	2.01±0.23	2.01±0.21
Heart rate, beats/min	67±12	68±10	70±11
Systolic BP, mm Hg	118±13	125±13	124±12
Diastolic BP, mm Hg	75±10	77±9	79±9
LV ED volume index, ml/m^2	69±10	112±24*	76±14†
LV ES volume index, ml/m^2	25±7	39±10*	33±9*†
LV SV volume index, ml/ m^2	44±7	73±16*	44±8†
LV EF, %	64±7	65±4	57±7*†
LV ED dimension, mm	49±4	59±7*	49±5†
LV ES dimension, mm	32±4	37±5*	34±7*
LV ED mass index, g/m^2	50±10	70±13*	56±11†
LV ED volume/mass, ml/g	1.45±0.38	1.62±0.26	1.41±0.35†
LV ES R/T ratio	1.48±0.40	1.65±0.54	1.71±0.65
Peak early filling rate, ml/sec	378±110	686±273*	288±91†

Values are n or mean±SD. BP: blood pressure; R/T ratio: radius /wall thickness measured at distal LV; *: P<0.05 pre-operative MR vs. Controls, post-operative MR vs. Controls; †: P<0.05 post-operative MR vs. pre-operative MR. Comparison results were adjusted for age.

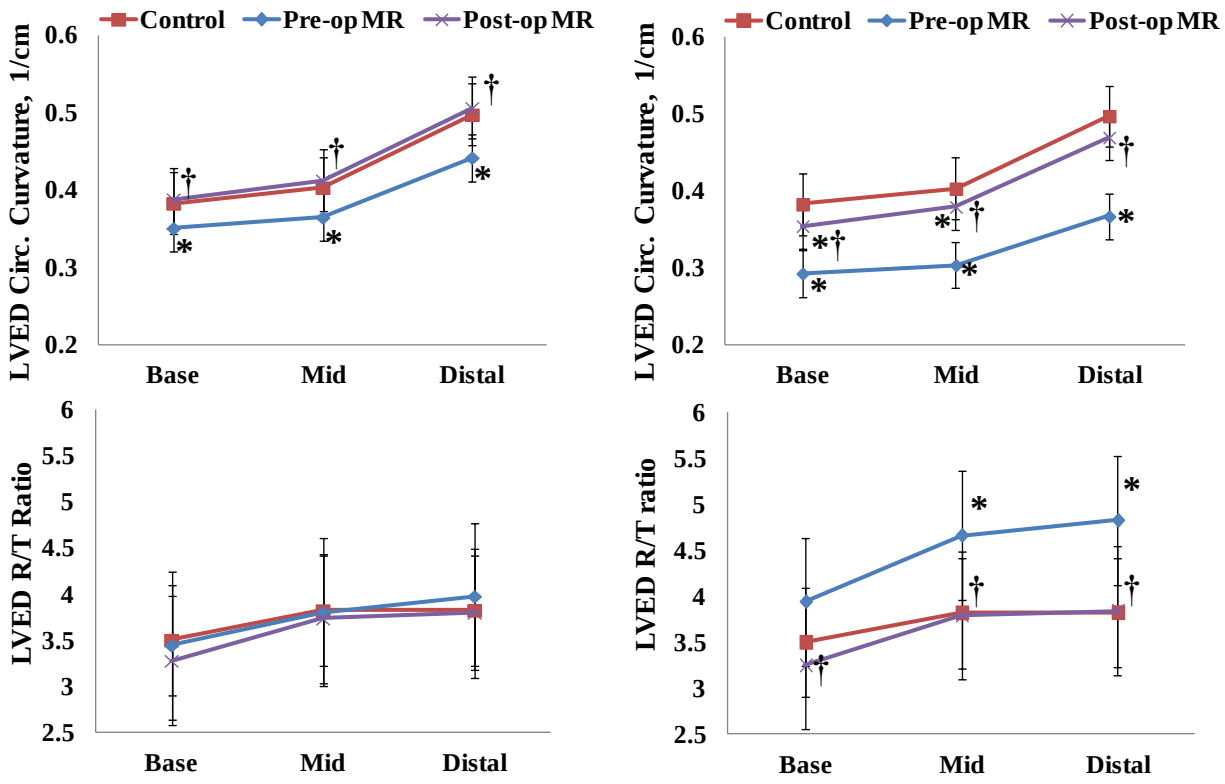

Figure 3.7 Comparisons of geometry in controls vs. surgical MR (LVEF>60%) at ED
Comparison of LV end-diastolic (ED) geometric remodeling in controls and in surgical MR patients (patients with cMR-derived LVEF<60% prior to surgery are excluded) with pre-operative LVESD < and ≥ 37mm before and after surgery demonstrate progressive LV remodeling at ED in the two MR groups and their recovery after surgery. LVED R/T ratio is normalized after surgery in both MR groups. Circumferential curvatures in MR LVESD<37mm are normalized after surgery while in MR LVESD≥37mm, circumferential curvatures are increased yet not normalized. *: P<0.05 pre-operative MR vs. Controls, post-operative MR vs. Controls; †: P<0.05 post-operative MR vs. pre-operative MR.

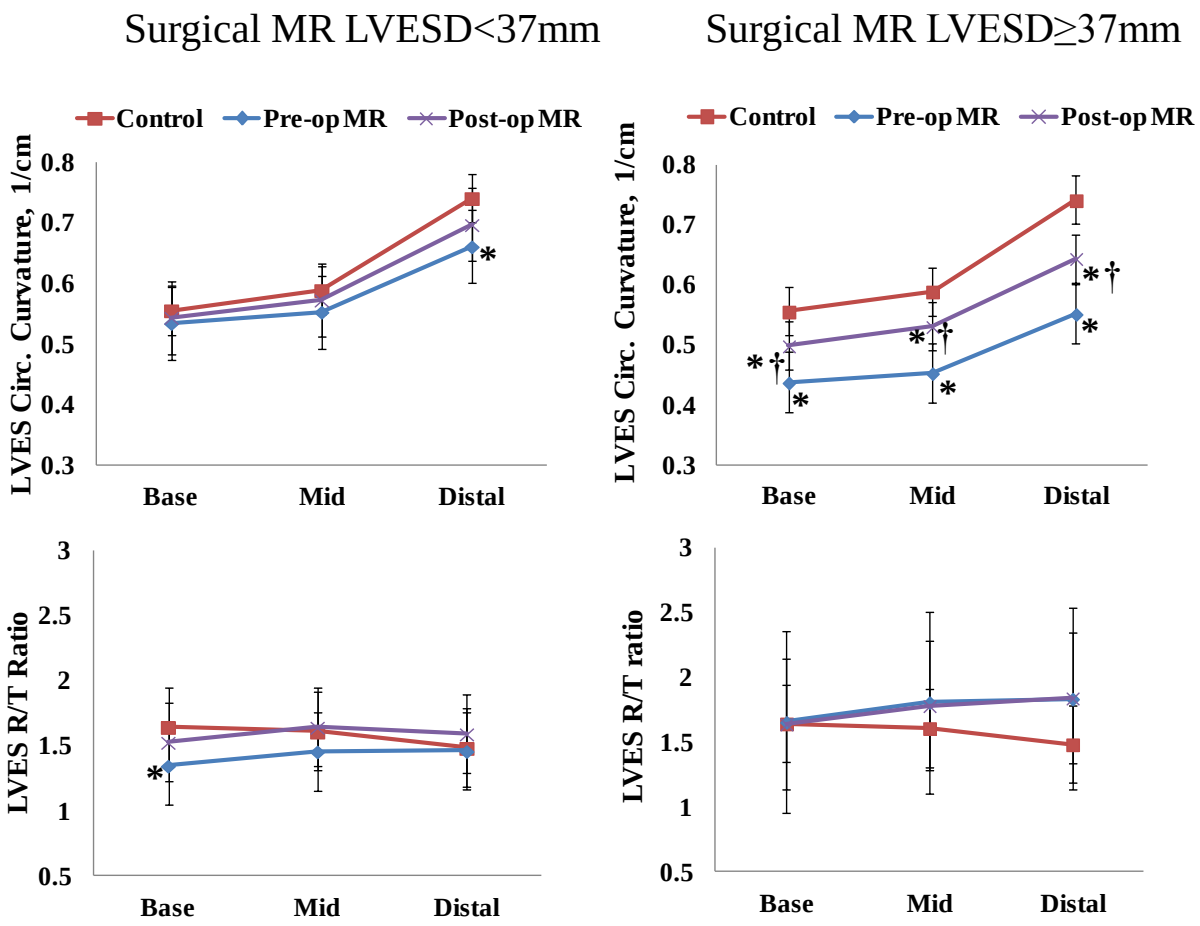

Figure 3.8 Comparisons of geometry in controls vs. surgical MR (LVEF>60%) at ES
Comparison of LV end-systolic (ES) geometric remodeling in controls and in surgical MR patients (patients with cMR-derived LVEF<60% prior to surgery are excluded) with pre-operative LVESD < and ≥ 37mm before and after surgery demonstrate progressive LV remodeling at ES that is not normalized after surgery in the MR patients with pre-operative LVESD ≥ 37mm, while it is normalized after surgery in MR patients with pre-operative LVESD<37mnm. *: P<0.05 pre-operative MR vs. Controls, post-operative MR vs. Controls; †: P<0.05 post-operative MR vs. pre-operative MR.

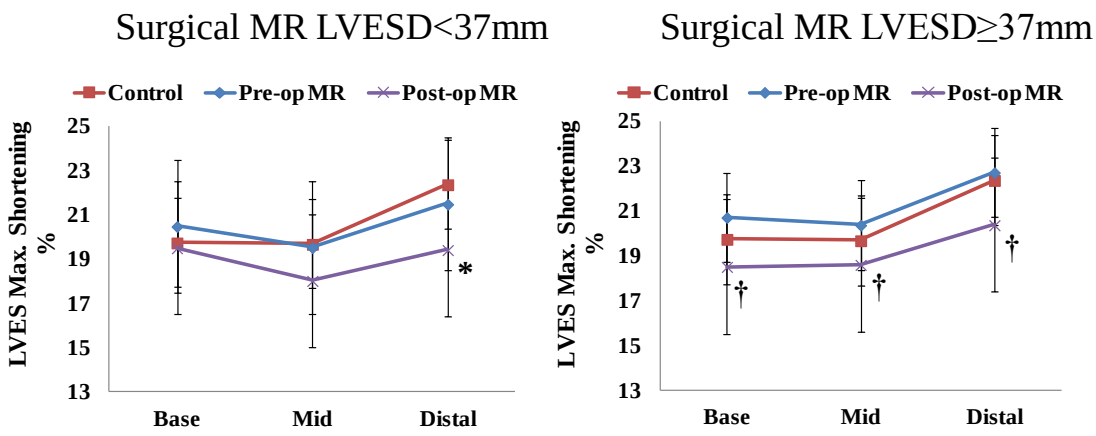

Figure 3.9 Comparisons of maximum shortening in controls vs. surgical MR (LVEF>60%) Comparison of LV end-systolic (ES) maximum shortening in controls and in surgical MR patients (patients with cMR-derived LVEF<60% prior to surgery are excluded) with pre-operative LVESD < and ≥ 37mm before and after surgery demonstrate that maximum shortening is decreased below normal in both groups of MR patients. Moreover, LVES maximum shortening in patients with pre-operative LVESD ≥37 mm is significantly decreased post-operatively vs. pre-operatively. *: P<0.05 pre-operative MR vs. Controls, post-operative MR vs. Controls; †: P<0.05 post-operative MR vs. pre-operative MR.

3.4 Discussion

A major finding of the current investigation is that LVESD, although commonly used to assess the extent of LV remodeling in patients with isolated MR, does not accurately reflect the extent of LV remodeling, largely due to spherical LV remodeling from mid to apical LV. Furthermore, conservative management of patients with isolated MR based on standard dimensions was associated with significant decrease in LVEF and maximum strain post MV repair. In comparison to a group of control subjects with similar age range, the relation of LVESD to LVESV is cubic in MR in contrast to a quadratic relation in controls, indicating a greater increase in LVESV per unit of LVESD in MR as compared to controls. The Bullet formula, which is commonly used to calculate LV volumes, significantly underestimates MR LVESV based on the LVESD measured at the tips of the papillary muscles. The extra volume can be attributed to the extensive LV mid-to-distal spherical remodeling, which is not accounted

for in the Bullet formula. The importance of this finding is that while LVESD remains below the accepted target of 40 mm for surgical intervention of isolated MR, its associated LVESV can range as high as twice that of the normal controls. This finding therefore identifies a volumetric parameter (LVESV) that more suitably characterizes overall LV remodeling in isolated MR.

The variance in LVESV in MR is attributed to LV mid to apical spherical remodeling that is evident even in the patients with LVESD below 37mm; however, LVES R/T ratio remains normal suggesting a more compensated hypertrophy in this group. It is of interest that even with an increase in LVESV in the MR ESD ≥37mm group, there is not a commensurate LV elongation, which is consistent with a more global spherical LV remodeling. This is also associated with an increase in the LVES R/T ratio at all LV segments from base to distal LV, a marker of increased wall stress. Despite this progression of adverse LV remodeling, maximum shortening from the base to distal LV remains normal in both groups. This finding is in agreement with the known favorable loading conditions of an increase in LV preload and excessive adrenergic drive [63, 64] combined with a facilitation of ejection through a secondary ejection pathway into left atrium in isolated MR.

In an attempt to determine the functional importance of these geometric changes in isolated chronic MR, we evaluate LV geometry and function in 35 patients from this cohort before and one year after mitral valve repair. All patients are within current echocardiographic guidelines for mitral valve surgery for chronic MR. Nevertheless, LVEF are significantly decreased after surgery, despite normalization of the LVEDV/mass ratio. It is important to note that the decrease in LVEF and LV maximum strain from pre- to post-operative values persists in patients with cMR-derived LVEF > 60% prior to mitral valve repair. The incidence of post-operative LV dysfunction, defined as LVEF<50%, occurs in about 1/3rd of these patients. In particular, the

incidence of post-operative LV dysfunction with LVESD≥37mm is greater than that with LVESD<37mm (P=0.0616). It is important to note that in MR patients with LVESD≥37mm, LVES R/T ratio remains ~30% above normal from mid to distal LV post-surgery. In addition, LV maximum shortening is decreased below normal from base to distal LV after surgery. Furthermore, in MR patients with LVESD<37 mm, the extent of spherical LV remodeling prior to surgery is associated with a significant decrease in LV maximum shortening after surgery. We have recently reported the finding of excessive cardiomyocyte oxidative stress, myofibrillar degeneration, and lipofuscin accumulation, which collectively may result in irreversible cardiomyocyte dysfunction in patients with pre-operative LVEF >60% [24]. Taken together, the presence of adverse LV remodeling prior to MV surgery is associated with decreased maximal shortening one year after surgery.

Dujardin et al. [65] have demonstrated an exponential correlation between LVESD and LVESV using echocardiography, especially for enlarged ventricles. The current study utilizes cMR with 3D analysis and determines that the relation between LVESV and LVESD is cubic in MR and quadratic in controls. Apical spherical remodeling appears to occur prior to a significant change being detected at the base. Thus, severely elevated LVES volume can occur prior to LVES dimension reaching 40 mm. In support of a volumetric analysis in isolated MR, Ozdogan et al. [66] and Cawley et al. [67] have also suggested that the use of a geometry independent volume assessment using cMR is preferred for LVEF measurement in timing of surgery.

The current study is limited in that follow-up of patients is only one year in a small number of patients. Previous reports in patients with aortic regurgitation and aortic stenosis demonstrate that there is continued improvement for years following surgery [68, 69]. Despite a small sample size, this represents a homogeneous population who do not have evidence of coronary artery

disease by coronary angiography. All patients being referred for surgery had LVEF>60% and almost all had LVESD <40mm by referral echocardiography studies and need for surgery was based on conservative clinical judgment. Subsequent cMR and 3D analysis uncover some patients with LVEF<60%, highlighting the need for a more comprehensive volumetric analysis of LV remodeling. Finally, while we are convinced that the surrogate outcome of LVES volume will be strongly related with the important clinical outcomes, it is clear this question can only be addressed in a clinical trial testing the comparative effectiveness of LV dimensions versus cMR- or 3D echo-derived LV volume on clinical outcomes.

The results of the current study uncover greater LV remodeling that contributes to higher LVES volume and corresponds with decreased LV shortening strain after surgery, suggesting that simple geometry-based assessments of volume may underestimate LV dysfunction in isolated MR. The current investigation demonstrates the potential for high variability of spherical remodeling from the LV mid to apex, beyond the conventional point of LVESD measurement, that contributes to the increase of LVES volume. Importantly, this adverse LV remodeling prior to surgery is associated with a reduction in maximum shortening. These results suggest that a more detailed geometric LV analysis and volume-based assessment at ES provide a superior evaluation of extent of LV remodeling and may serve as a better marker for optimal timing of surgery in the patient with isolated MR in order to maximally preserve post-operative LV function.

CHAPTER 4 MYOCARDIAL SURFACE MODELING USING CINE CMR

4.1 Introduction

Measurements of cardiac geometry, such as volume and curvature, in response to volume or pressure overload are significantly important for clinical decision making. The results of the study of marathoners versus MR patients indicate that the geometry remodeling in the MR patients, especially the apex remodeling, differs from that of geometry remodeling in the Marathoners even though they both have similar elevated global end-systolic (ES) volume and dimension measured at the tip of the papillary muscle. The results of the study of pre and post-surgical MR patients also demonstrate the importance of three-dimensional (3D) volumetric analysis in evaluating the remodeling and severity of MR patients.

Despite the promise of cMR, approaches for quantifying cardiac geometry remain problematic. When using myocardial surface models for measuring left ventricular (LV) curvatures, which are typically based on cylindrical, spherical or prolate spheroidal coordinate systems, difficulties occur due to the existence of a singularity at the apex of the LV. Also, these surface models usually require a symmetry that is not applicable in the complex right ventricle (RV). Additionally, systolic translocation of the RV atrio-ventricular annulus is greater than that of the LV, resulting in unequal LV and RV stroke volumes (SV) calculated from simply summing volumes of each short axis cMR slice multiplied by the slice thickness. In the results of the study of marathoners versus MR patients, the SV measurements in the RV and LV did not match (see Table 2.2).

Research on developing surface modeling has been reviewed comprehensively by Frangi et al. [70]. These methods have been well developed and are rather mature in terms of providing most parameters measurements needed in clinical use.

The prerequisite of myocardial surface modeling was the delimitation of the endocardial and epicardial boundaries of the heart. A typical cine study had four groups with four typical views, short axis, 2-chamber, 4-chamber and LVOT. The group with short-axis view usually contained 10 to13 slices, while the groups with 2-chamber, 4-chamber and LV outflow tract (LVOT) views generally had one slice each. Typically, each slice had 20 timeframes, lasting for a cardiac cycle. Therefore, there were about 320 images per cine study per subject. Manually contouring all the images could be extremely tedious. Besides, the results of manual contouring suffered from inter-user variability. As a result, there have been techniques devoted to automatic segmentation in order to minimize the user interaction [71-80]. Petitjean et al. recently reviewed the segmentation methods using cMR short-axis images [81]. However, there were a couple of issues that prevent the pursuit of ideal automatic segmentation. First of all, the images could be badly misregistered.

The cine cMR acquisition used standard ECG-gated, breath-hold steady state free precession technique. The subjects were required to hold their breath during an acquisition of 1 to 4 slices. The position of the heart might be slightly different after each breath hold, which could cause the slices acquired during different breath-holds to be misregistered. Secondly, image quality and noise might introduce error into the segmentation. Thirdly, there were papillary muscles attaching to the ventricular wall near end-systole which should be included in the endocardium contours. The papillary muscles were obvious at end-diastolic timeframe. However, as the heart contracts, the papillary muscles merged into the heart wall. Therefore, it

was difficult to distinguish them from the actual heart wall muscle. As a result, the endocardium segmentation result could recognize the papillary muscles as a heart wall muscle and exclude them in the contours.

In conclusion, to our best knowledge, there were no methods that have successfully solved the above-mentioned problems and provided accurate automatic segmentation. Therefore, in this research, contours from ED and ES were drawn manually, rather than automatically, and by experts who had no knowledge of the subject's pathology. If time series analysis was required, the contours at ED and ES were propagated to the rest of the time frames using the dual contour propagation method [59] developed in-house, and surface modeling of the heart chambers were applied to the 3D binary segmentations that were generated from the contours.

For the rest of this section, previous research on myocardium surface generation will be reviewed. These methods can be mainly categorized into two types: coordinate-based surface modeling and non-coordinate-based surface modeling.

4.1.1 Coordinate-Based Surface Modeling

It is well known that in normal humans and in most pathologies, the LV of the heart has a regular shape which can be approximated with a spherical topology. Some surface modeling techniques for the LV utilized this feature as the prerequisite information to construct the 3D surface of the LV [82-86]. Bardinet et al.[82] fitted a superquadric model to a set of 3D contour points and then utilized free-form deformation [87] to take local deformations into account. This model was further extended for motion tracking [88]. Han et al.[83] employed a generalization form of superquadric model, namely hyperquadric model to fit the 3D range data. Huang et al. [84] proposed a new surface matching technique for spherical harmonic model which employed the rotational properties of the spherical harmonic basis function to establish the correspondence

between surfaces. Abdallah et al. [85] also reconstructed the LV surface based on spherical harmonic model using SPECT image data. A triangulated surface was first constructed from segmented image data and uniformly parameterized [89, 90]. Then a rotation invariant 3D shape descriptor was extracted using abstract harmonic analysis and shift theorem [91-93]. The problem with superquadrics was their doubly symmetric crossing [86] which could limit their ability to represent an irregular shape family. Coppini et al. [94] modeled the LV as a closed thin elastic surface and the sparse contour data as a set of radial springs bouncing on the surface. The surface constructing process embedded the knowledge of spherical topological shape of the LV in the neural network implementation.

Rather than utilizing spherical topology, general cylinder and prolate spheroidal coordinate based models have also been developed. Goshtasby et al. [95] utilized a generalized cylinder to fit to the 3D data points which were obtained from intensity threshold based auto-segmentation. Hunter et al. [96] first introduced the use of a prolate spheroidal coordinate system for cardiac image segmentation. They further utilized this coordinate system to describe the geometry of the heart [97] and constructed a finite element model [98] with prolate spheroidal coordinates to describe the mechanical and electrical behavior of the heart. Vallet et al [99] was motivated by this work and developed a new formulation for segmentation using 3D cardiac echocardiography images. Young et al. [100] fitted a finite-element model to data obtained from biplane coronary cine angiograms to construct an epicardial surface. Bicubic hermite basis functions were employed to interpolate the prolate spheroidal geometric parameters.

Matheny et al. [101] performed a comparison among different harmonic functions, such as prolate spheroidal, oblate spheroidal, and cylindrical harmonics, on how well they represented

different geometries. They concluded that the four-dimensional spherical harmonics function best fitted the LV of the heart.

Rather than utilizing different harmonic functions, Staib et al. [86] proposed a parametric Fourier model of the surface which was a uniform shape representation that described the entire shape. The surface was further deformed to a particular shape of interest by applying the probability distribution model to the parameters of the representation. A similar Fourier descriptor was described by Tello et al. [102]. Stalidis et al. [103] further employed the Fourier decomposition and wavelet decomposition to construct a deformable spatiotemporal parametric model.

4.1.2 Non-Coordinated-Based Modeling

Compared to surface modeling methods that implemented the prior knowledge of anatomical shape, surface modeling techniques that did not use polar coordinate systems nor assume a regular, spherical shape of the heart are attractive to our research problem. These methods did not try to construct a parametric description of the surface. Instead, they constructed the surface simply from the planar contours, a set of arbitrary 3D contour points, or binary segmented image data.

A number of different mesh generation methods have been developed [104, 105] with advantages and disadvantages. Connecting contour methods [106, 107] used consecutive slices with triangles. However, triangulation from planar contours usually suffered from branching, tiling, or corresponding problems [108]. Marching cubes [109] used a logical cube created from eight pixels between two consecutive slices. By moving the logical cube, the surface of an object was located. The interaction between the segmented images and the cube generated an index which corresponded to a triangulated cube listed in the pre-calculated table as shown in Figure

4.1 [109]. The normal of the triangles were calculated by linear interpolating the normal of the eight cube vertexes which were obtained using central differences. Gouraud sharing was used to render the surface. The results were verified using CT, MR images and SPECT images.

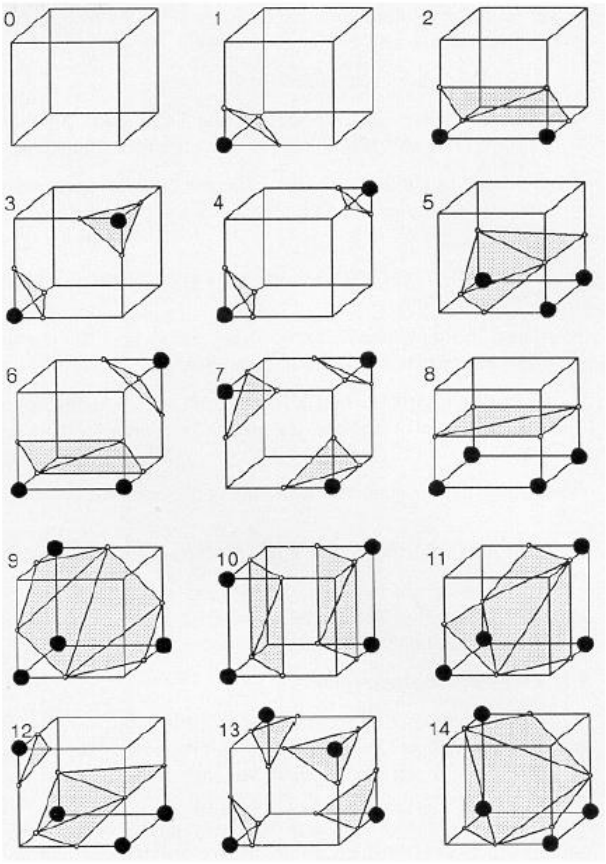

Figure 4.1 Triangulated cubes for marching cubes algorithm
Figure source [109]

The problem with using marching cubes in cMR was that the voxels in cMR were strongly anisotropic. The in-plane resolution of the image was typical 1.5 mm while the out-of-plane resolution (slice thickness) was usually 8 mm, a few times lower than in-plane resolution. Without additional processing, the generated mesh would suffer evident terracing artifacts. Figure 4.2 illustrates the terracing effects by generating the triangulated surface of a RV using marching cubes. Additional processing to improve the triangulation included reducing the

number of triangles [110], further improving the marching cubes by developing a marching triangle [111], or performing triangle simplification [112]. Other mesh quality improvement methods, such as smoothing, optimization or decimation have been employed along with marching cubes [113].

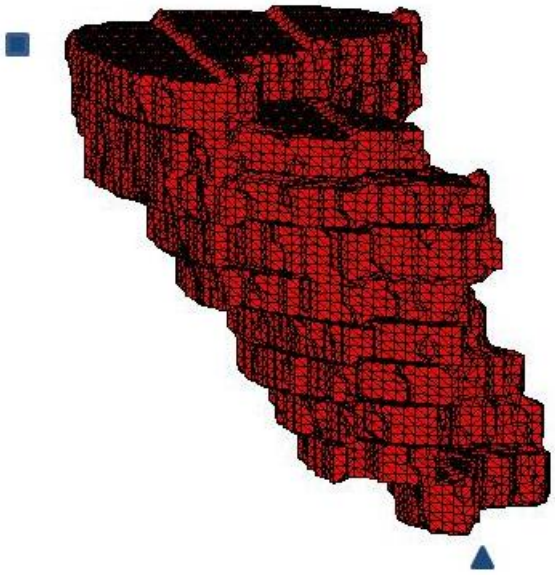

Figure 4.2 Illustration of the terracing effects by marching cubes
Blue square: RV free wall; blue triangle: RV apex

The marching cubes algorithm was modified to better fit myocardium surfaces. Lotjonen et al. [114] modified the marching cubes algorithm by first generating a surface topology using marching cubes, then searching the Voronoi polygons [115] for triangle nodes on the surface. In the end, the triangulation was completed by connecting the neighboring Voronoi areas. Peiro et al. [116] built an implicit surface using a radial basis function [117] then used the marching cubes algorithm to triangulate the surface. The quality of the triangulated mesh was further improved by standard mesh modification techniques through curvature adaption [118]. Gibson [119] proposed the surface net concept to deal with terracing artifacts. In this method, the surface net was first created using marching cubes, then the surface nodes were relaxed to reduce an

energy measure in the links; however, the nodes were constrained within its original surface cube to ensure a faithful topology. The energy function was defined as the sum of the squared lengths of all the links in the surface net. A smoothed surface net was then triangulated, and a distance map was generated by calculating the distance of the pixels to their nearest triangles. Although this method was meant for solving the terracing problem in generating meshes from binary-segmented data, the problem still persisted.

Skrinjar et al. [120] proposed a mesh generation technique using cardiac MR short axis images by mapping a pre-meshed sphere with close-to-equilateral triangles to the surface of the segmented object using the gradient field of solution of the Laplace's equation between the sphere and the boundary of the object. A stopping function for the mapping was defined using a pseudo-thin plate spline model [121]. The result was compared to the surface generated by marching cubes [109]. The comparison result showed that the average in-slice distance between the meshes generated by the two methods were very close while the surface generated by Skrinjar was much smoother. The advantage of this method was that it did not assume a regular, spherical shape of the heart and it could be applied to objects with any shape. Moreover, this method significantly reduced the terracing problems that could be caused by the short axis cMR images. However, generating a triangulated mesh of a myocardial surface using Skrinjar's method could take more than two hours. Therefore, this method was too time-consuming for clinical use and many research applications. Furthermore, it was difficult to control the smoothness of the generated surface to balance the need for fitting the contours versus the need for generating a smoothly-varying heart surface.

4.1.3 Conclusion

Surface generation techniques from segmented image data have been well explored. For those techniques that constructed the surfaces with prior knowledge of the anatomical shape using a non-Cartesian coordinate system, the surfaces were usually represented parametrically such as using harmonic functions, Fourier descriptor, etc. The shapes were usually obtained through minimizing an energy cost function which was composed of an internal regularization term and an external attraction potential, in an iterative manner. The advantage of these parametric models was that the essential information of the object could be represented in a compact form. However, the regular and symmetric property of the model could limit its ability to model irregular shapes, such as the RV. The RV was especially different from the LV in terms of its cardiac function and shape. The RV was more of a crescent shape which is neither symmetric nor regular. As a result, these techniques which assumed the ellipsoidal shape of the chamber would fail to precisely model the RV. In addition, according to our observations and experience, the use of 3D non-Cartesian coordinate systems to model the surface usually resulted in a singularity at the apex of the model, which prevented the concise measurements at the apex. And measurement of the apex remodeling was clinically important for certain heart diseases as described in Chapters 2 and 3. Moreover, it was difficult to determine how many control points are sufficient in the final model using these techniques.

A category of surface modeling techniques to construct a triangulated surface mesh was also reviewed. Contour-based triangulation suffered from tiling and terracing problems even after an optimization procedure was applied. Also, the position of the triangles could not be determined arbitrarily. Even though topologically and geometrically corrected triangulation methods could ease this problem, due to the high gap between in-plane resolution and out-of-plane resolution in cMR images, terracing was still a problem for most techniques.

4.2 Motivation

In order to generate surfaces for myocardium without the concerns of singularities and asymmetric shapes, the triangulated mesh model proposed by Skrinjar et al [120], which can model irregular shapes, can be utilized. The idea of the triangulated mesh model was to map a pre-meshed sphere with close-to-equilateral triangles to the surface of the segmented object using the gradient field of solution of the Laplace's equation between the sphere and the boundary of the object. The advantage of this method was that it does not assume a regular, spherical shape of the heart and it could be applied to objects with any shape. Therefore, this method could be utilized to model the surfaces of both the LV and RV. However, generating a triangulated mesh of a myocardial surface using the Skrinjar's method could take over two hours depending on the user-defined parameters. Therefore, this method was too time-consuming to fulfill a real-time surface generation task. Furthermore, using Skrinjar's method, it was difficult to control the surface smoothness, which was a problem when there were contour mis-registration errors.

In order to resolve the efficiency problem of Skrinjar's method, the famous statistical deformable model, active shape model (ASM), was utilized as a post processing technique. Since ASM was applied on triangulated meshes in this study, we called it active mesh model (AMM). Since Skrinjar's method could generate myocardial meshes that were consistent from subject to subject, this makes it particularly well suited for AMM. By utilizing AMM, Skrinjar's method only needed to run on a small set of training subjects, as opposed to every subject. A new mesh out of the training set was generated using AMM in less than 20 seconds. Moreover, utilizing AMM could help reduce inter-user variability and manual contour errors by controlling the deformed new mesh within the constraints of the training set. Since the RV wall was much

thinner compared with the LV wall and having a more complex shape, the determination of the RV wall was usually difficult and subjective [122]. Moreover, the atrio-ventricular margin of the ventricle was hard to determine, which made the selection of basal slice for the RV uncertain. Figure 4.3 illustrates the orientation of the basal RV in relation to the LV.

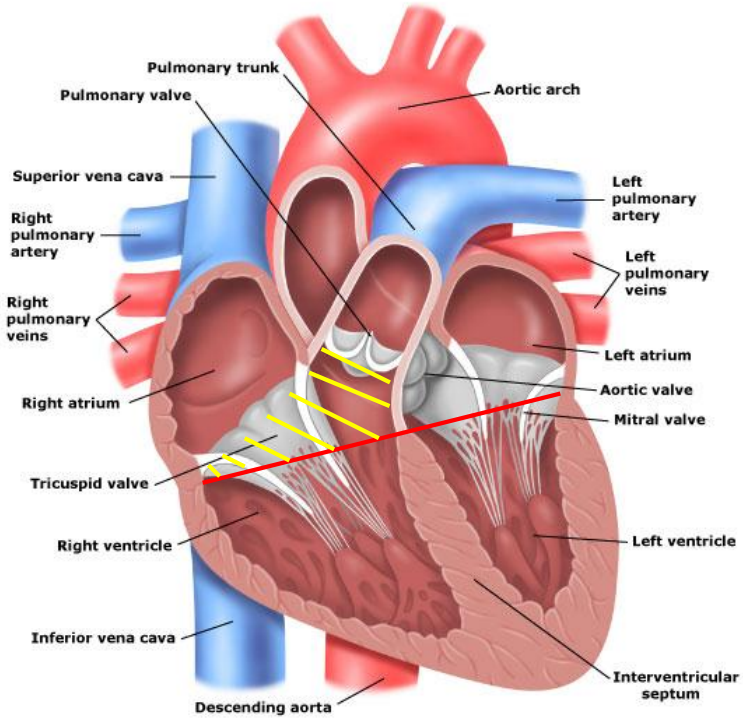

Figure 4.3 Illustration of the interior heart with RVOT highlighted
Yellow shadow: region of RVOT; Red line: orientation of the short axis slice; RVOT: right ventricle outflow tract.

The RV outflow tract (RVOT) as shown in yellow was part of the RV and the accuracy in contouring RVOT affected the resulting RV volume largely. However, the orientation of the RV outflow tract (RVOT) as shown in yellow was different from the conventional orientation of the LV short axis slices as shown in a red line. Therefore, it was difficult to outline the RVOT in the short axis view. If the contours of the subjects in the training set were accurately performed by cardiologists and double checked by peers, the constraints would help ensure the precise construction of the RV surface.

Therefore, in this study, we utilize a modification of Skrinjar's method and AMM to achieve the following main goals: 1) to fit a smooth surface for both LV and RV, including the LV apex and RV base; 2) to accomplish real-time surface generation with significant computational efficiency; 3) to derive clinical useful parameters for LV and RV based on the constructed meshes.

The major contribution of this work includes:

- Three dimensional distance maps are constructed from the short axis contours and long axis contours independently and merged together to construct an isotropic binary segmentation which provides complete information of the ventricle, including the base and the apex.
- A new smoothing function is embedded to Skinjar's method to improve control over the triangulated surface smoothness.
- To better utilize the advantage of AMM and limit the effect caused by the small sample size in the training set, the point distribution models are constructed separately for different ventricles (LV/RV) with different pathology (such as normal or mitral regurgitation).
- To construct the point distribution model, mesh vertex correspondence in the training set is predefined on the sphere before the generation of the meshes. The generated meshes are further aligned to construct the mean mesh.
- The proposed model is applied to three groups of subjects, including normal subjects, mitral regurgitation (MR) patients and pulmonary hypertension (PH) patients. Cardiac geometric and functional parameters are derived from the generated meshes and the model is validated in various ways.

The rest of this chapter is organized as follows. Skrinjar's method is reviewed in detail in Section 4.3, followed by the review of research in statistical deformable models in Section 4.4. In Section 4.5, the proposed biventricular active mesh model is described in detail. It is followed by experimental results in Section 4.6, discussion in Section 4.7 and conclusions in Section 4.8.

4.3 Skrinjar's Method

Skrinjar's method mapped vertex points from a sphere, which could be perfectly tessellated with equilateral triangles, to any surface that was topologically equivalent to a sphere. The procedure of Skrinjar's Method is summarized in Figure 4.4 [120] using a 2D example.

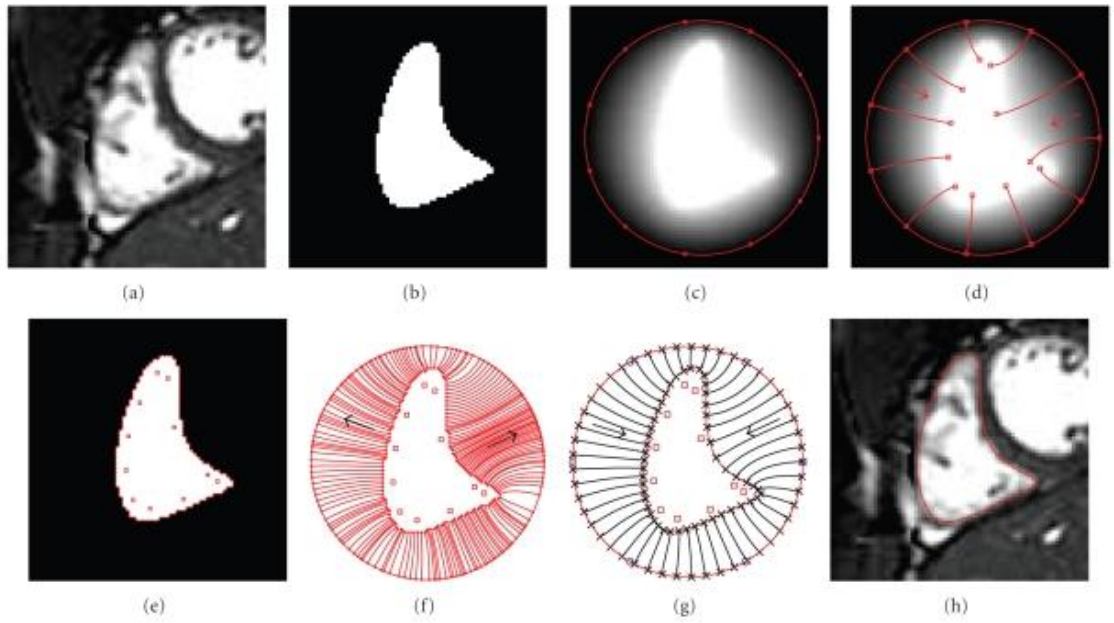

Figure 4.4 Summery of Skrinjar's Method[120]

A stack of short axis images (usually 12-17 parallel slices with 256×256 pixels, 1.4 mm in-plane resolution and 8.0 mm out-of-plane resolution) were first segmented manually (Figure 4.4(b)). Then an anisotropic 3D segmentation was constructed from the slice segmentations. A pre-triangulated sphere [123, 124] was generated centered at the segmentation with a radius of R equal to the maximum distance from the center to the boundary of the 3D segmentation. The

boundary points ($\mathbf{r}_b$, b=1,…,B) were identified as the midpoint between two neighboring voxels with different labels (i.e. one voxel is in the object and one is not).

The mapping of points from the sphere to the object was governed by the Laplace's equation,

$$\Delta u = 0 \tag{4.1}$$

which was solved on the domain between the sphere and the surface of the object. u was equal to 0 on the sphere and was equal to 1 on the object surface. Points on the sphere were mapped to the object surface along the gradient of u,

$$\frac{d\mathbf{r}(t)}{dt} = \nabla u(\mathbf{r}(t)) \tag{4.2}$$

The solution to Equation 4.1 was

$$u(\mathbf{r}) = \sum_{m=1}^{M} c_m f_{\mathbf{s}_m}(\mathbf{r}) \tag{4.3}$$

where $\mathbf{s}_m$, m = 1, . . . ,M, were the locations of M singularities (defined below) and c_m, m=1,…,M were the corresponding coefficients (defined below) and $f_s(\mathbf{r})$ was defined as,

$$f_{\mathbf{s}}(\mathbf{r}) = \frac{1}{\sqrt{|\mathbf{r}|^2 - 2|\mathbf{r}||\mathbf{s}| + |\mathbf{s}|^2}} - \frac{R}{\sqrt{|\mathbf{s}|^2|\mathbf{r}|^2 - 2R^2|\mathbf{r}||\mathbf{s}| + R^4}} \tag{4.4}$$

which satisfied the following:

$$\lim_{\mathbf{r}\to\mathbf{s}} f_{\mathbf{s}}(\mathbf{r}) = \infty \tag{4.5}$$

$$f_{\mathbf{s}}(\mathbf{r})|_{|\mathbf{r}|=R} = 0 \tag{4.6}$$

$$\Delta f_{\mathbf{s}} = 0 \tag{4.7}$$

The gradient of $f_{\mathbf{s}}$ was then derived as

$$\nabla f_{\mathbf{s}} = \frac{\partial f_{\mathbf{s}}}{\partial \mathbf{r}} = \frac{\mathbf{s}-\mathbf{r}}{(|\mathbf{r}|^2 - 2|\mathbf{r}||\mathbf{s}| + |\mathbf{s}|^2)^{3/2}} + \frac{R(|\mathbf{s}|^2\mathbf{r} - R^2\mathbf{s})}{(|\mathbf{s}|^2|\mathbf{r}|^2 - 2R^2|\mathbf{r}||\mathbf{s}| + R^4)^{3/2}} \tag{4.8}$$

The *M* singularity points were defined by first uniformly distributing the *M* points on the sphere. In order to locate the *M* singularities within the object, a regular-shape, discrete lattice was defined to enclose the sphere. The segmentation was resampled on the regular-shaped lattice to obtain an isotropic segmentation. The isotropic segmentation was then eroded twice. The domain on the lattice between the sphere and the eroded segmentation was defined as Ω_{eroded}. The Laplace's equation was then solved numerically on Ω_{eroded}. This solution was defined as u_{discrete}. The *M* points on the sphere were then propagated from the sphere to the eroded segmentation along the gradient of u_{discrete} using the fourth-order Runge-Kutta method [125]. This procedure is illustrated in Figure 4.4(c, d, and e).

The coefficient c_m in Equation 4.3 was solved as a constant, *c*, to avoid negative coefficients for the singularities. The value of *c* was obtained by solving the following equation,

$$\frac{\partial O}{\partial c} = 0 \tag{4.9}$$

where O was defined as $O = \frac{1}{2}\sum_{b=1}^{B}[u(\mathbf{r}_b) - 1]^2$, which led to the close form solution of *c*,

$$c = \frac{\sum_{b=1}^{B} d_b}{\sum_{b=1}^{B} d_b^2} \tag{4.10}$$

where $d_b = \sum_{m=1}^{M} f_m(\mathbf{r}_b)$.

Ideally, the propagation should stop at $u\big(\mathbf{r}(t)\big) = 1$. However, since the object was defined by a discrete, 3D segmentation and u was a continuous function defined on a continuous domain, the propagation was instead stopped as $u\big(\mathbf{r}(t)\big)$ reached a value defined by a stopping function which was represented by a pseudo-thin plate spline model *S* [121],

$$S(\hat{\mathbf{p}}_b) = \alpha_0 + \sum_{k=1}^{K} \alpha_k \psi(\hat{\mathbf{p}}_b \cdot \hat{\mathbf{q}}_k), \qquad b = 1, \ldots, B \tag{4.11}$$

where $\hat{\mathbf{p}}_b$ was the unit vector of a point on the sphere corresponding to the boundary point $\mathbf{r}_b$ on the object and was obtained by propagating the boundary point $\mathbf{r}_b$ from the object to the sphere along -∇u (see Figure 4.4 (f)). *K* was the user-defined number of control points. $\hat{\mathbf{q}}_k$ was the unit vector of the control point on the sphere (as shown in blue dots in Figure 4.4 (g)). ψ was defined in [121] with m=2. The coefficients $\alpha_0, \ldots, \alpha_K$ were determined by minimizing $\sum_{b=1}^{B}[S(\hat{\mathbf{p}}_b) - u(\mathbf{r}_b)]^2$, which led to the close form solution of $\alpha_0, \ldots, \alpha_K$,

$$\begin{bmatrix} \alpha_0 \\ \alpha_1 \\ \vdots \\ \alpha_K \end{bmatrix} = (G^T G)^{-1} G^T \begin{bmatrix} u(\mathbf{r}_1) \\ u(\mathbf{r}_2) \\ \vdots \\ u(\mathbf{r}_B) \end{bmatrix} \tag{4.12}$$

where *G* was

$$G = \begin{bmatrix} 1 & \psi(\hat{\mathbf{p}}_1 \cdot \hat{\mathbf{q}}_1) & \ldots & \psi(\hat{\mathbf{p}}_1 \cdot \hat{\mathbf{q}}_K) \\ 1 & \psi(\hat{\mathbf{p}}_2 \cdot \hat{\mathbf{q}}_1) & \ldots & \psi(\hat{\mathbf{p}}_1 \cdot \hat{\mathbf{q}}_K) \\ \vdots & \vdots & & \vdots \\ 1 & \psi(\hat{\mathbf{p}}_B \cdot \hat{\mathbf{q}}_1) & \ldots & \psi(\hat{\mathbf{p}}_B \cdot \hat{\mathbf{q}}_K) \end{bmatrix} \tag{4.13}$$

Finally, *V* vertices were uniformly distributed on the sphere. For any vertex on the sphere **v**, the vertex was propagated to the object using Equation 4.2 and stopped when $u(\mathbf{r}(t)) = S(\mathbf{v}/|\mathbf{v}|)$ as shown in Figure 4.4 (g).The 2D version of the generated mesh is shown in Figure 4.4 (h).

The steps of Skrinjar's method are now summarized as follows:

1. Preprocessing
    a. Segment the object in each short axis slice;
    b. Construct an anisotropic 3D segmentation from the slice segmentations;
    c. Identify boundary points $\mathbf{r}_b$, b=1,…, B;
    d. Construct a sphere that surrounds the anisotropic 3D segmentation.

2. Define singularity points
    a. Define a discrete, regularly-shaped lattice that encloses the sphere;
    b. Resample the segmentation on the regularly-shaped lattice;
    c. Erode the segmentation twice;
    d. Define Ω_{eroded} as the points on the lattice that are inside the sphere but not in the eroded segmentation;
    e. Numerically solve the Laplace's equation on Ω_{eroded}; Call this solution u_{discrete};
    f. Choose M (the number of singularity points);
    g. Define M uniformly-distributed points on the sphere;
    h. Propagate the M points from the sphere to the eroded segmentation in the direction of u_{discrete}; Call the points on the eroded segmentation the singularity points s_m.
3. Analytically solve the Laplace's equation
    a. Compute c using Equation 4.10;
    b. Define u using c and s_m.
4. Define the stopping function S
    a. Propagate each boundary point ($\mathbf{r}_b$) to the sphere in the direction of $-u$; Label the resulting points on the sphere as $\mathbf{p}_b$, compute their unit vectors $\widehat{\mathbf{p}}_b$;
    b. Choose K (the number of control points);
    c. Define K uniformly-distributed points on the sphere, and compute the control point unit vectors $\widehat{\mathbf{q}}_k$, k=1,…,K;
    d. Compute the coefficients $\alpha_0, \ldots, \alpha_K$ using Equation 4.12.
5. Mesh the segmentation
    a. Choose V (the number of mesh vertices);

b. Define V uniformly-distributed points on the sphere; Label these points on the sphere as **v**;

c. Propagate the vertex points, **v**, from the sphere to the surface using Equation 4.2;

d. Stop when $u(\mathbf{r}(t)) = S(\mathbf{v}/|\mathbf{v}|)$.

4.4 Statistical Deformable Model

In this section, we review the literature on active shape models (ASM) and an overview of how they work.

4.4.1 Previous Research

Statistical deformable models have been developed for myocardium segmentation purposes [70]. The most famous methods among them are active shape model (ASM) [78] and active appearance model (AAM) [79]. ASM utilized a point distribution model (PDM) to search for image border. Representative points (such as boundary points) of the images in the training set were first labeled. All shapes were then aligned using a modification of the Procrustes analysis [126] until the mean shape converged. PDM of the training set was defined as the mean shape and a weighted sum of the first user-defined *t* modes of the eigenvectors computed from the covariance matrix from the point-to-point correspondence using principle component analysis (PCA) [127]. The weight parameter vector, **b**, was limited to be within three standard deviation of the mean. By varying **b**, the variability in the training set could be captured. These constraints were then applied in ASM for image searching. The assumption of using PCA was that the cloud of data points in the training set was close to an ellipsoidal shape. This assumption could be less restrictive if the sample size was large [127].

Many algorithms have been utilized to modify ASM for image searching [128]. Instead of using PCA, an independent component analysis (ICA)-based statistical shape model was

proposed [129]. Both PCA and ICA had their applications and strengths [130]. Also AAM improved ASM in terms of taking the gray level variation into consideration which was good at modeling appearance. This model was useful for tracking and image recognition [131].

Besides ASM and AAM, other techniques for modeling spatial variability have been developed. Parametric Gaussian shaped distribution [132] modeled the distribution of the landmark points using a parametric distribution function while non-parametric spatial landmark probability distributions [133] modeled their distribution using a nonparametric function. Moreover, probabilistic atlas [134] built a spatial probability distribution function.

4.4.2 Active Shape Model (ASM)

Given a set of N training shapes, $\mathbf{m}_i$ was a vector denoting the V boundary points of the ith shape in the set $\mathbf{m}_i=[x_{i0}; y_{i0}; z_{i0}; x_{i1}; y_{i1}; z_{i1}; \ldots x_{iV\text{-}1}; y_{iV\text{-}1}; z_{iV\text{-}1}]$, $i=1,\ldots N$. These shapes were aligned using the Procrustes analysis. Then the mean shape $\bar{\mathbf{m}}$ of the training set was defined as

$$\bar{\mathbf{m}} = \frac{1}{N}\sum_{i=1}^{N} \mathbf{m}_i \tag{4.14}$$

And the point distribution model (PDM) describing the variance of the training set was defined as

$$\mathbf{m} = \bar{\mathbf{m}} + \mathbf{\Phi b} \tag{4.15}$$

where $\mathbf{\Phi}$ was a matrix containing the first t eigenvectors calculated by PCA over the covariance matrix $\boldsymbol{S} = \frac{1}{N}\sum_{i=1}^{N}(\mathbf{m}_i - \bar{\mathbf{m}})(\mathbf{m}_i - \bar{\mathbf{m}})^{\mathrm{T}}$. The vectors in $\mathbf{\Phi}$ were mutually orthogonal and of unit length. The first t eigenvectors were corresponding to the first t eigenvalues $\lambda_1 \geq \lambda_2 \geq \cdots \geq \lambda_t$. t was selected such that $\frac{\lambda_1+\lambda_2+\cdots+\lambda_t}{\lambda} \times 100\% = \rho$. The total information in the covariance matrix was represented by λ, while the user-defined ρ was the percentage of information contained in

the first *t* eigenvectors. ρ was selected such that $\mathbf{\Phi}$ contained the most information with the least number of eigenvectors. The shape parameter vector, **b**, controlled the variation of the new shape. The value of **b** was defined within certain limit such that the resulting shape was consistent with the training set. In general, b_k could be defined as $|b_k| \leq \pm 3\sqrt{\lambda_k}$, where λ_k was the *k*th eigenvalue.

ASM utilized PDM in Equation 4.15 to generate new mesh out of the training set by adjusting the vertices along the gradient of the potential image and updating the parameters **b** within the allowable limit.

4.5 Proposed Biventricular Active Mesh Model

In this section, a novel active mesh generation technique is proposed. An overview of the proposed method is shown in Figure 4.5. First of all, a set of training subjects is randomly selected. Then a 3D segmentation is generated from the contours of both short axis and long axis for each subject. Thirdly, a triangulated mesh is constructed by adapting Skrinjar's surface generation technique (Skrinjar's Method) and implementing it with additional improvement using a new smoothing function. Fourthly, a point distribution model (PDM) is constructed based on the training meshes. Finally, new test subjects are randomly selected and a biventricular active mesh model is applied to deform PDM to fit each of the test subjects.

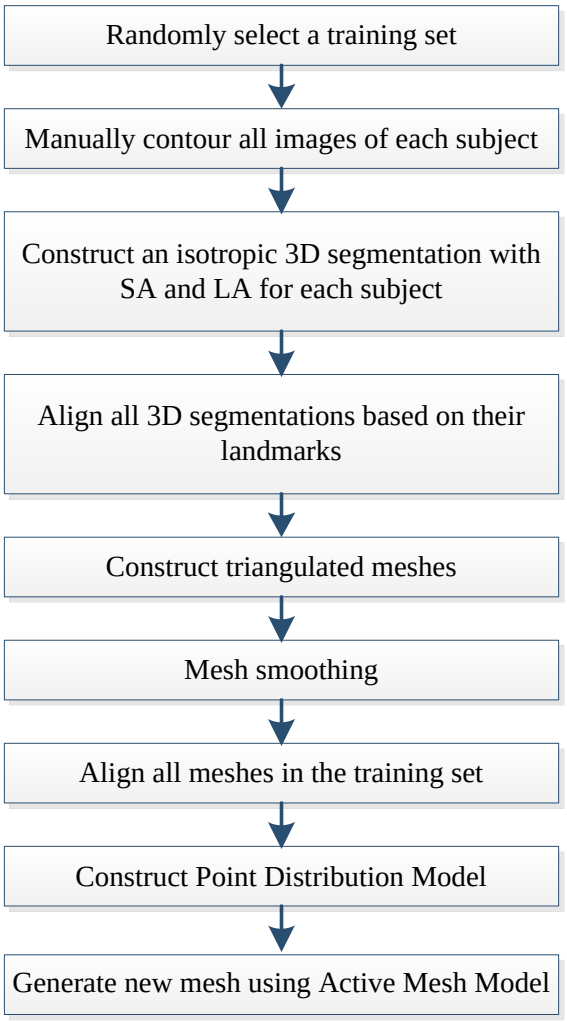

Figure 4.5 Biventricular active mesh model generation procedure

In Section 4.5.1, the procedure of generating the triangulated mesh on the LV of a normal subject is given. In Section 4.5.2, the procedure of generating the active mesh model based on the normal training set is described. In Section 4.5.3, cardiac geometric and functional analyses using the generated meshes are described.

4.5.1 Triangulated Mesh Generation and Smoothing

A training set with *N* normal subjects is randomly selected. LV contours on the ED and ES timeframes are drawn by experts using an in-house semi-automatic contouring tool with closed B-splines.

4.5.1.1 *3D Isotropic Binary Segmentation*

To construct a triangulated mesh with minimum terracing and maximum gray level information in the apex, a 3D isotropic binary segmentation is constructed utilizing both short axis and long axis contours.

Given a study with 10-13 parallel short axis contours, one long axis contour with 4 chamber view, one long axis contour with 2 chamber view, and one long axis contour with LV outflow tract (LVOT) view, a bounding box is first computed based on all contours. Then for the parallel short axis contours, a 2D distance map is computed for each slice based on the Euclidean distance of the pixels to the contour. The distance of the pixels inside the contour is defined negative while the distance of the pixels outside the contour is defined positive. Linear interpolation is then performed on all 2D distance maps to obtain a 3D short axis distance map within the bounding box.

For long axis contours, a 2D distance map is also computed for each slice. The intersection line between the 4 chamber long axis contour and the 2 chamber long axis contour is selected as the center axis. As illustrated in Figure 4.6, for any point, **c**, within the bounding box, a rotation axis going through **c**, perpendicular to the center axis is made. By rotating the rotation axis to **c**'s nearest image slices (Slice A and Slice B), angular interpolation is performed to determine the distance of **c**, *d*(**c**),

$$d(\mathbf{c}) = \frac{\theta_b}{\theta} d(\mathbf{a}) + \frac{\theta_a}{\theta} d(\mathbf{b}) \tag{4.16}$$

where $\theta = \theta_a + \theta_b$. *d* (**a**) and *d* (**b**) are the distance of pixels **a** and **b** defined in their 2D images.

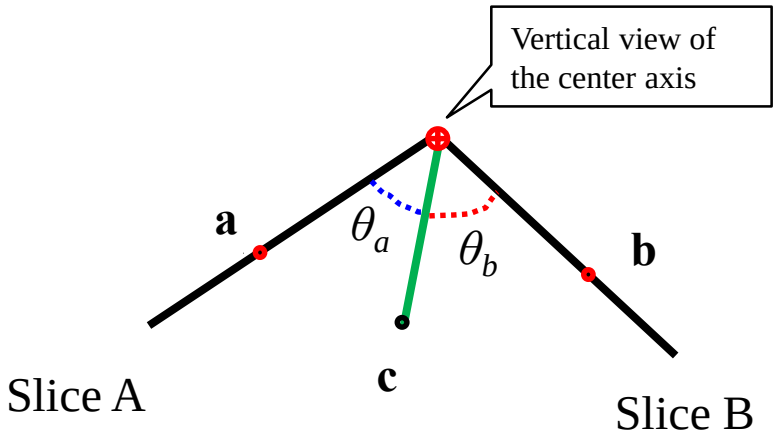

Figure 4.6 2D illustration of the angular interpolation
c is a random point within the bounding box. Slice A and B are the nearest neighbors of point **c**. Green line is the rotation axis. Point **a** and **b** are the projections of point **c** onto slice A and B by rotating the rotation axis on the center axis.

Both long axis and short axis 3D distance maps are merged based on a minimum distance. Finally a 3D binary segmentation is obtained by a certain distance threshold. The generated 3D segmentation is not only isotropic but also contains the information of apex. Figure 4.7 shows examples of a LV and a RV 3D segmentation.

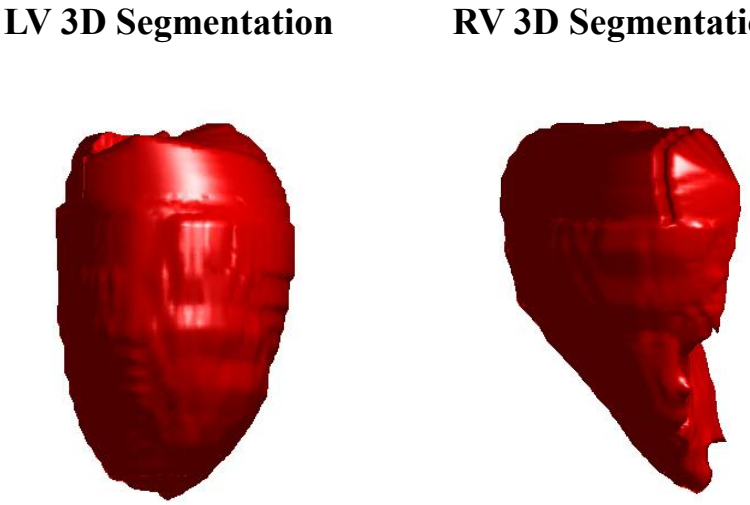

Figure 4.7 A typical LV and RV epicardium 3D segmentations

For studies that only have three slices with long-axis view, there are usually only two long-axis slices with RV view, i.e. the slice with the 4 chamber view (black block) and the slice with

LVOT view (gray block) as shown in Figure 4.8. Since RV is not of symmetric regular shape and the rotation axis is not going through the center of RV, only points in between the two slices with RV view can be accurately interpolated using angular interpolation. The rest of the points in the bounding box cannot be interpolated correctly.

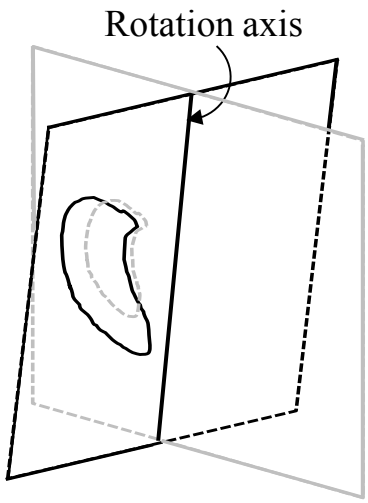

Figure 4.8 Illustration of the intersection between 4CH view slice and LVOT slice
Black slice: long axis with 4Chamber view; Gray slice: long axis with LVOT view. Contours within the slices represent the RV.

Therefore, the 3D segmentations of RV for these studies are generated using only short axis contours. However, if the short axis contours do not cover the RV all the way to the RV apex, the information at RV apex will be missing. To complete the 3D RV segmentation with RV apex, one extra contour is added to the RV apex landmark and parallel to the existing short axis contours. The RV apex landmark is defined on the long axis slice with 4 chamber view. Take the short axis contour that is closest to the RV apex landmark and shrink the contour towards its center to one third of its original size. Transform the contour and RV apex landmark from their image coordinates to fitting coordinates in which the short axis contours are perpendicular to the *z* axis. Then move the contour along the *z* axis to where the RV apex

landmark is located. Figure 4.9 shows a result of this process. The 3D segmentation of the RV is generated based on this new set of contours.

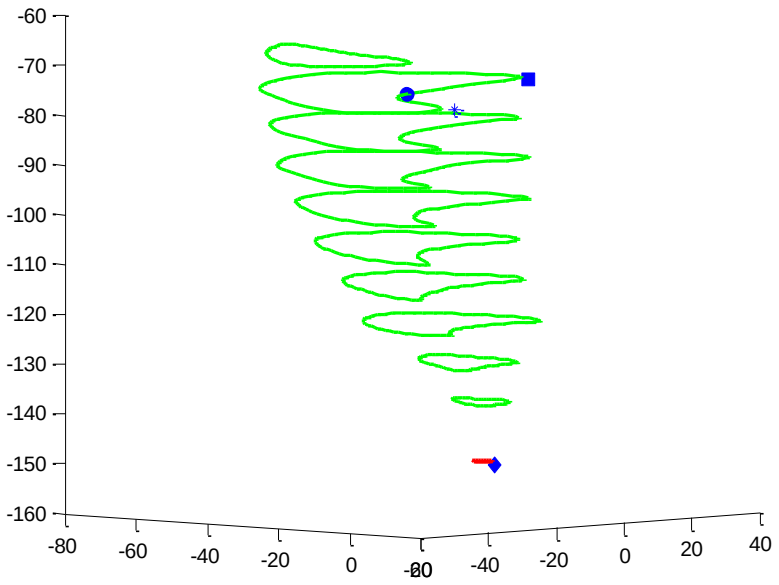

Figure 4.9 Result of adding extra RV short axis contour
*: RV inferior insertion; ■: RV anterior insertion; ●: Mid septum; ◆: RV apex; green lines: original RV short axis contours; red line: extra RV contour

4.5.1.2 *Smoothing Function*

The advantage of Skrinjar's method was that it generates high-quality triangles. As a result, the terracing problem in the generated surfaces of cMR images with anisotropic pixel resolution was reduced. In our research, this method is adapted and implemented with some improvements. The surface generation procedure is applied to isotropic 3D image segmentations to further reduce terracing effects. Also, in order to account for the smooth and continuous property of the heart surface, a surface smoothing function is proposed utilizing the angles between the surface normals.

According to Skrinjar's method, the vertices are mapped from the sphere to the object based on a stopping function *S* (Equation 4.11). Since the heart's surface is smooth and uniform

in texture, it is very important to map the vertices to the object with smooth surface curvature. The smoothness of the surface can be detected by the dramatic change of the surface normals on each vertex. As a result, a smoothing function for the mapping is proposed which incorporates the surface normal,

$$E = E_{boundary} + \gamma E_{curv} \tag{4.17}$$

where the $E_{boundary}$ represents the mapping error between the vertices to the boundary approximated by the stopping function *S*. The E_{curv} term controls the smoothness of the surface. The tuning parameter, γ, controls the impact of the E_{curv} term. The value of γ is studied and the result is presented in Section 4.6.2.2.

$E_{boundary}$ is defined as follows:

$$E_{boundary} = \frac{1}{V}\sum_{v=1}^{V}\left\|u\left(\mathbf{r}_v(t)\right) - S(\widehat{\mathbf{r}_v(0)})\right\|^2 \tag{4.18}$$

where *V* is the number of vertices on the sphere.

E_{curv} is defined as follows,

$$E_{curv} = \frac{1}{V}\sum_{v=1}^{V}\left((\frac{1}{L}\sum_{l=1}^{L}(1 - \mathbf{n}_v \cdot \mathbf{n}_l)\right) \tag{4.19}$$

where $\mathbf{n}_v$ is the unit vector of the normal of the *v*th vertex and $\mathbf{n}_l$ is the unit vector of the normal of *l*th vertex in the one-ring neighborhood of the *v*th vertex as shown in Figure 4.10. *L* is the number of vertex in the one-ring neighborhood of *v*th vertex. The normal of a vertex is calculated as the weighted sum of the unit normal of the triangles in its one-ring neighborhood as shown in Figure 4.10, assuming *L*=5. The weights are commonly suggested to be equal to the inverse of the distance from the vertex to its neighborhood triangle centers, respectively [135]. The normal of the *v*th vertex is then calculated as

$$\mathbf{n}_v = \frac{\sum_{l=1}^{L} w_l \mathbf{n}_l}{\| \sum_{l=1}^{L} w_l \mathbf{n}_l \|} \tag{4.20}$$

$\frac{1}{V}$ and $\frac{1}{L}$ are the normalization terms that normalize the smoothing function such that it is independent from the number of vertex.

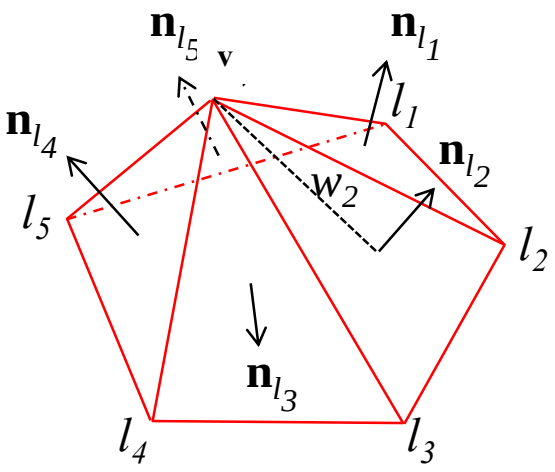

Figure 4.10 Illustration of the one ring neighborhood of a vertex v

Thus, the propagation of the vertices will be along the gradient of *u* and will stop when the smoothing function *E* is minimized.

4.5.2 Active Mesh Model (AMM)

In our research, the active mesh model (AMM) is an adaption and implementation of ASM on triangulated meshes. The correspondence of vertices among the training meshes are predefined on the sphere before the generation of triangulated meshes. The generated training meshes are further aligned to construct the point distribution model (PDM). The 3D segmentation of a new subject in the test set is generated and AMM utilizing PDM is then applied to search for the boundary of the 3D segmentation with the constraints of the shapes of training samples.

4.5.2.1 *Point Distribution Model Generation*

To generate a PDM from a training set, a mesh is generated for each subject in the training set and aligned with meshes from other subjects so the PDM only characterizes differences in shape and not differences in position and orientation. The quantities $\bar{\mathbf{m}}$ and $\mathbf{\Phi}$ defined in Section 4.4.2 are then computed from the aligned meshes. This alignment procedure consists of two steps. First, the landmarks and contour points for each subject are aligned to a common coordinate system. This alignment step is called pre-alignment. A segmentation and mesh is then generated for each subject using the procedure in Section 4.5.1. Each mesh is then aligned a second time to a common coordinate system (called post-alignment) and the quantities $\bar{\mathbf{m}}$ and $\mathbf{\Phi}$ are computed. Details of these steps are described below.

4.5.2.1.1 Pre-Alignment and Segmentation

For each training subject, four landmarks, anterior RV insertion, inferior RV insertion, mid-septum and LV apex are allocated. All landmarks and contour points are transformed from the scanner coordinates to a coordinate system (called fitting coordinates) with the *z* coordinate running from apex to base and the *x* coordinate running through the anterior RV insertion into the LV wall.

Let $\mathbf{L}_i$ be a 4 by 3 matrix describing the four landmarks of the *i*th subject in the set in fitting coordinates. Each row contains the coordinates of a landmark. The mean landmark matrix $\bar{\mathbf{L}}$ is calculated as the mean of all landmark matrices $\mathbf{L}_i, i = 1,,,,N$ in the set. $\mathbf{L}_i$ is then aligned to $\bar{\mathbf{L}}$ by the rotation matrix $\mathbf{R}_i$ and the translation vector $\mathbf{o}_i$ such that $\sqrt{\frac{1}{4}\sum_{j=1}^{4}\left\|\mathbf{R}_i\left(\mathbf{l}_{ij}^T - \mathbf{o}_i\right) - \bar{\mathbf{l}}_j^T\right\|^2}$ is minimized. $\mathbf{R}_i$ and $\mathbf{o}_i$ are calculated using Kabsch algorithm [136]. $\mathbf{l}_{ij}$ is the *j*th row of the *i*th landmark matrix $\mathbf{L}_i$ and $\bar{\mathbf{l}}_j$ is the *j*th row of $\bar{\mathbf{L}}$. Let this new coordinates be the aligning

coordinates. Define P_i as the number of contour points of the *i*th subject in the training set, and define $\boldsymbol{P}_i$ as a P_i by 3 matrix containing the contour points in fitting coordinates. Each row of $\boldsymbol{P}_i$ contains the coordinates of a contour point. $\boldsymbol{P}_i$ is then transformed to the aligning coordinates by the same rotation and translation used to align the landmark points. i.e. $\widehat{\mathbf{P}}_i = (\mathbf{R}_i(\mathbf{P}_i^T - \mathbf{O}_i))^T$, where $\mathbf{O}_i = [\mathbf{o}_i, \mathbf{o}_i, \dots, \mathbf{o}_i]$, a 3 by P_i matrix. The 3D segmentation of the *i*th subject is then constructed (Section 4.5.1.1) based on the contours in the aligning coordinates $\widehat{\mathbf{P}}_i$.

It is important to note that the above transformation is a rigid body transformation. The contour points and the resulting 3D segmentation of each subject are not scaled or deformed. The purpose of this procedure is to align the segmentations that are used to generate meshes, such that the generated meshes are consistent from subject to subject with matching vertices.

4.5.2.1.2 Mesh Generation and Post-Alignment

A sphere with unit radius is nearly uniformly sampled with *V* user-defined vertices using the algorithm in [123, 124]. The triangulation on the sphere is constructed using Delaunay triangulation [137]. This unique pre-triangulated sphere is then used for all aligned segmentations with various radiuses equal to the maximum distance from the center to the boundary of the 3D segmentations to generate the triangulated surfaces. Therefore, the generated triangulated meshes are pre-aligned with matching vertices $\mathbf{v}_1$ to $\mathbf{v}_V$.

As all triangulated meshes are generated for the training set, these meshes are aligned to each other using Procrustes analysis. The quantities $\bar{\mathbf{m}}$ and $\boldsymbol{\Phi}$ are calculated according the Section 4.4.2. ρ is selected such that $\boldsymbol{\Phi}$ contains the most information with the least number of eigenvectors. In our study, $\rho = 98\%$. The PDM of this training set is then defined as $\mathbf{m} = \bar{\mathbf{m}} + \boldsymbol{\Phi}\mathbf{b}$.

4.5.2.2 *Active Mesh Model-Deformation of PDM to a New Object*

Having generating the flexible PDM, we deform the PDM to fit a subject not in the training set. LV endocardium contours on the ED and ES timeframes are drawn using the semi-automatic contouring tool with closed B-splines developed in-house. Four landmarks, anterior RV insertion, inferior RV insertion, mid-septum and LV apex are allocated. All landmarks and contour points are transformed from the scanner coordinates to the pre-alignment coordinate system with the procedure described in Section 4.5.2.1.1. From the contours in pre-alignment coordinates, a bounding box, a 3D distance map and a 3D segmentation of the new subject are generated using the method described in Section 4.5.1.1.

Once the 3D segmentation is generated, the deformation procedure, as shown in Figure 4.11, is applied to generate a new mesh. In Figure 4.11 and the following description, define **r** and **x** as $3V\times1$ arrays obtained by vertically stacking the 3 by 1 vertex points $\mathbf{v}_i$, i=1,.., V. Define the operator $T\{\mathbf{r}|\, s, \theta, \mathbf{o}\}$ as the operation of scaling, rotating, and translating each vertex in **r** by s, θ, and **o** respectively.

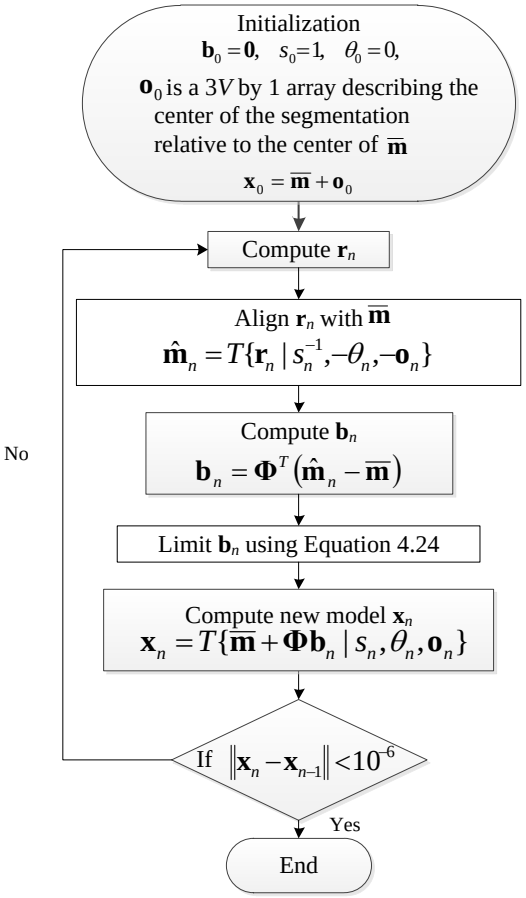

Figure 4.11 Active mesh deformation flow chart

- Initialization

Set $\mathbf{b}_0 = \mathbf{0}$, $s_0 = 1, \theta_0 = 0$, the model is initialized as $\mathbf{x}_0 = \bar{\mathbf{m}} + \mathbf{o}_0$, where $\mathbf{o}_0 = [o_{0_x}, o_{0_y}, o_{0_z}, \ldots, o_{0_x}, o_{0_y}, o_{0_z}]^T$, a 3$V$ by 1 vector and V is the number of vertices. $[o_{0_x}, o_{0_y}, o_{0_z}]$ is the center of the segmentation relative to the center of $\bar{\mathbf{m}}$. The center of $\bar{\mathbf{m}}$ is computed as the mean of all vertices in $\bar{\mathbf{m}}$. To compute the center of the segmentation, the boundary points of the segmentation are identified. The boundary points are defined as the midpoint between two neighboring voxels with different labels (i.e. one voxel is in the object and one is not). The center of the segmentation is computed as the mean of all boundary points.

- Compute $\mathbf{r}_n$

$\mathbf{r}_n$ is computed by moving each vertex in $\mathbf{x}_n$ along its normal vector to minimize the distance to the segmentation. Let $\mathbf{x}_{n_i}$ be the *i*th vertex in $\mathbf{x}_n$, $\mathbf{n}_{n_i}$ be its corresponding normal vector and $d(\mathbf{x})$ be the distance from the point $\mathbf{x}$ to the nearest point on the segmentation. $\mathbf{r}_{n_i}$ is given by

$$\mathbf{r}_{n_i} = \mathbf{x}_{n_i} + t^* \mathbf{n}_{n_i}, \qquad i = 1, \dots V \tag{4.21}$$

where

$$t^* = \arg\min_t d\left(\mathbf{x}_{n_i} + t\mathbf{n}_{n_i}\right) \tag{4.22}$$

The minimization is performed by discretizing *t* and doing an exhaustive search.

- Align $\mathbf{r}_n$ to $\bar{\mathbf{m}}$

Compute s_n, θ_n and $\mathbf{o}_n$ using the Procrustes analysis such that $\hat{\mathbf{m}}_n = T\{\mathbf{r}_n | s_n^{-1}, -\theta_n, -\mathbf{o}_n\}$ is best conformed to the mean shape $\bar{\mathbf{m}}$.

- Update $\mathbf{b}_n$

Recall the PDM $\mathbf{m} = \bar{\mathbf{m}} + \mathbf{\Phi}\mathbf{b}$. We wish to find $\mathbf{b}_n$ such that $\hat{\mathbf{m}}_n \approx \bar{\mathbf{m}} + \mathbf{\Phi}\mathbf{b}_n$, which yields

$$\mathbf{b}_n = \mathbf{\Phi}^T(\hat{\mathbf{m}}_n - \bar{\mathbf{m}}) \tag{4.23}$$

since $\mathbf{\Phi}^T = \mathbf{\Phi}^{-1}$.

By referring to [78], the model parameter vector $\mathbf{b}_n$ is controlled within an allowable limit, i.e.

$$b_{n_k} = \begin{cases} 3\sqrt{\lambda_k} & \text{for } b_k > 3\sqrt{\lambda_k} \\ -3\sqrt{\lambda_k}, & \text{for } b_k < -3\sqrt{\lambda_k} \\ b_k & \text{others} \end{cases} \qquad k = 1,2, \dots, t \tag{4.24}$$

where *t* is the number of eigenvectors contained in $\mathbf{\Phi}$.

4.5.3 Cardiac Geometric and Functional Analyses

Once the mesh is constructed, global parameters such as volume, stroke volume can be calculated. Regional parameters such as wall curvatures can be calculated for morphological analysis. Most importantly, the mesh can describe the shape of the LV and the shape of the RV. The apex of the LV is also well represented.

4.5.3.1 *Volume Computation*

Denote the vertices of the *i*th triangle face on the mesh as $\mathbf{v}_{i1}$, $\mathbf{v}_{i2}$, and $\mathbf{v}_{i3}$ and the mean of all vertices on the mesh as $\mathbf{v}_4$. $\mathbf{v}_{i1}$, $\mathbf{v}_{i2}$, and $\mathbf{v}_{i3}$ and $\mathbf{v}_4$ form the *i*th tetrahedron of the mesh. The volume of the mesh is computed as the sum of the volumes of the tetrahedrons formed by the mesh. For the LV mesh, the center of the mesh $\mathbf{v}_4$ is commonly within the mesh, all formed tetrahedrons are enclosed by the mesh. However, since the RV mesh has a concave region (the septal wall) and a convex region (the free wall), the center of the mesh could possibly be out of the mesh. If that is the case, the tetrahedrons with triangle faces pointing out of the direction of the center $\mathbf{v}_4$ will include both in-mesh volume and out-of-mesh volume and the tetrahedrons with triangle faces pointing towards the direction of the center $\mathbf{v}_4$ are out of the mesh. Volume out of the mesh should not account for the volume of the mesh. In order to avoid overestimating the volume of the mesh by including the volume out of the mesh, signed tetrahedron volumes are computed instead[138]. The sign of the *i*th tetrahedron volume is determined by whether the *i*th triangle face is pointing towards the direction of the center $\mathbf{v}_4$, if so, the sign of the volume is negative, if not, the sign of the volume is positive. In such a way, the out-of-mesh volume of the tetrahedrons with triangle faces pointing out of the direction of the center $\mathbf{v}_4$ will be cancelled out by the negative volume of the tetrahedrons that are out of the mesh.

The volume *V* of the mesh is then computed as the sum of the signed volume of all tetrahedrons constructed by the mesh:

$$V = \sum_{i=1}^{T} \frac{(\mathbf{v}_{i1} - \mathbf{v}_4) \cdot ((\mathbf{v}_{i3} - \mathbf{v}_{i1}) \times (\mathbf{v}_{i2} - \mathbf{v}_{i1}))}{6} \tag{4.25}$$

where T is the number of tetrahedrons formed by the triangle faces on the mesh.

4.5.3.2 *Compute Regional Curvature*

Regional surface curvature is a critical parameter in the analysis of ventricular remodeling. Research on curvature computation of an underlying smooth surface represented by a triangulated mesh has been explored in the past [139-142]. In this section, a method for computing regional curvature from a triangulated mesh is presented. First, general theory on curvature computation is presented in Section 4.5.3.2.1. Then, how circumferential and longitudinal curvatures are computed in the LV and RV are presented in Section 4.5.3.2.2.

4.5.3.2.1 Curvature Theory

Given a vertex **v** on a triangulated mesh, the maximum curvature, $k_1(\mathbf{v})$, and the minimum curvature, $k_2(\mathbf{v})$, of **v** are called the principle curvatures, and the corresponding tangent directions, $\mathbf{e}_1$and $\mathbf{e}_2$, are called the principle directions. Let $k(\mathbf{v}, \mathbf{t})$ denote the curvature along the any tangent direction, **t**, of **v**. $k(\mathbf{v}, \mathbf{t})$ can be calculated using the Euler formula,

$$k(\mathbf{v}, \mathbf{t}) = k_1(\mathbf{v}) \cos^2 \theta_{\mathbf{t}} + k_2(\mathbf{v}) \sin^2 \theta_{\mathbf{t}} \tag{4.26}$$

where $\theta_{\mathbf{t}}$ is the angle between **t** and $\mathbf{e}_1$.

The algorithm of principle curvatures estimation on triangular mesh by Dong et. al [141] is implemented to estimate the principle curvatures and principle directions of each vertex on the triangulated mesh. Given a vertex, **v**, with unit normal vector, **n**, the vertices $\mathbf{v}_l$, l=1,.., L are located in the one-ring neighborhood of **v** on the triangulated mesh and are very close to **v** (See Figure 4.10). $\mathbf{n}_l, l = 1, \ldots L$ be their corresponding normal vectors. Let $\mathbf{t}_l$ denote the normalized

projection of vector $\mathbf{v}_l - \mathbf{v}$ on to the tangent plane at $\mathbf{v}$, i.e. $\mathbf{t}_l = \frac{(\mathbf{v}_l-\mathbf{v})-\langle \mathbf{v}_l-\mathbf{v},\mathbf{n}\rangle \mathbf{n}}{\|(\mathbf{v}_l-\mathbf{v})-\langle \mathbf{v}_l-\mathbf{v},\mathbf{n}\rangle \mathbf{n}\|}$, where $\langle \cdot, \cdot \rangle$ denotes the dot product. The curvature $k(\mathbf{v}, \mathbf{t}_l)$ can be approximated by $k(\mathbf{v}, \mathbf{v}_l - \mathbf{v})$ as [141],

$$k(\mathbf{v}, \mathbf{t}_l) \approx k(\mathbf{v}, \mathbf{v}_l - \mathbf{v}) = -\frac{\langle \mathbf{v}_l - \mathbf{v}, \mathbf{n}_l - \mathbf{n} \rangle}{\| \mathbf{v}_l - \mathbf{v} \|^2}, \qquad l = 1 \dots L \tag{4.27}$$

To compute the principle curvatures and principle directions at vertex $\mathbf{v}$, we first assume a random tangent direction, $\mathbf{t}_d$, at $\mathbf{v}$ as the principle direction $\hat{\mathbf{e}}_1$ and $\hat{\mathbf{e}}_2 = \frac{\hat{\mathbf{e}}_1 \times \mathbf{n}}{\|\hat{\mathbf{e}}_1 \times \mathbf{n}\|}$, as shown in Figure 4.12.

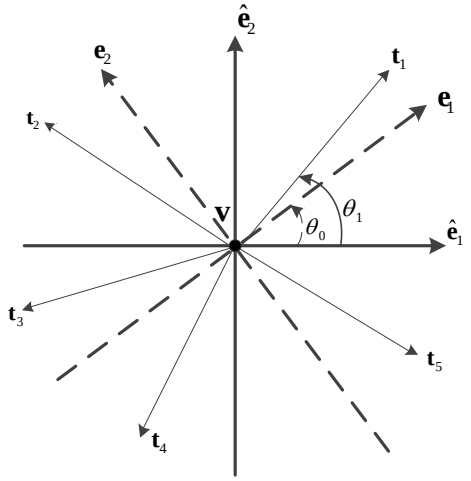

Figure 4.12 The coordinate system on the tangent plane of vertex v

Assuming θ_0 is the angle between $\hat{\mathbf{e}}_1$ and $\mathbf{e}_1$, $\theta_{\mathbf{t}_l}$ is the angle between $\mathbf{t}_l$ and $\hat{\mathbf{e}}_1$, $k(\mathbf{v}, \mathbf{t}_l)$ can be estimated as using Equation 4.26,

$$k(\mathbf{v}, \mathbf{t}_l) = k_1(\mathbf{v}) \cos^2(\theta_{\mathbf{t}_l} - \theta_0) + k_2(\mathbf{v}) \sin^2(\theta_{\mathbf{t}_l} - \theta_0), \quad l = 1 \dots L \tag{4.28}$$

which can be rewritten as

$$k(\mathbf{v}, \mathbf{t}_l) = \mathrm{a} \cos^2 \theta_{\mathbf{t}_l} + b \cos \theta_{\mathbf{t}_l} \sin \theta_{\mathbf{t}_l} + c \sin^2 \theta_{\mathbf{t}_l}, l = 1, \dots, L \tag{4.29}$$

where,

$$\begin{cases} a = k_1(\mathbf{v})\cos^2\theta_0 + k_2(\mathbf{v})\sin^2\theta_0 \\ b = 2(k_2(\mathbf{v}) - k_1(\mathbf{v}))\cos\theta_0 \sin\theta_0 \\ c = k_1(\mathbf{v})\sin^2\theta_0 + k_2(\mathbf{v})\cos^2\theta_0 \end{cases} \tag{4.30}$$

Let $a = k(\mathbf{v}, \mathbf{t}_d)$, and estimate $k(\mathbf{v}, \mathbf{t}_l), l = 1, \ldots, L$ using Equation 4.27. The constants b and c can be calculated by the least square method. Upon the known constants, the principle curvatures and principle directions can be solved according to Equation 4.30 as

$$\begin{aligned} k_1(\mathbf{v}) &= \frac{(a+c)}{2} + \sqrt{\frac{(a+c)^2}{4} - ac + \frac{b^2}{4}} \\ k_2(\mathbf{v}) &= \frac{(a+c)}{2} - \sqrt{\frac{(a+c)^2}{4} - ac + \frac{b^2}{4}} \\ \mathbf{e}_1 &= \cos\theta_0\, \hat{\mathbf{e}}_1 + \sin\theta_0\, \hat{\mathbf{e}}_2 \\ \mathbf{e}_2 &= \cos\theta_0\, \hat{\mathbf{e}}_2 - \sin\theta_0\, \hat{\mathbf{e}}_1 \end{aligned} \tag{4.31}$$

where $\theta_0 = \frac{1}{2}\arcsin\left(\frac{b}{k_2(\mathbf{v}) - k_1(\mathbf{v})}\right)$.

4.5.3.2.2 Computation of LV and RV Curvatures

To calculate the circumferential and longitudinal curvatures, the corresponding circumferential and longitudinal directions of each vertex need to be defined.

For a LV mesh, the triangulated mesh is transformed from the scanner coordinates (*x, y, z*) to the prolate spheroidal coordinates $(\theta, \varphi, \lambda)$ using the following relations.

$$\begin{aligned} x &= f\sinh\lambda\sin\varphi\cos\theta \\ y &= f\sinh\lambda\sin\varphi\sin\theta \\ z &= f\cosh\lambda\cos\varphi \end{aligned} \tag{4.32}$$

where $\lambda \in [0, \infty), \varphi \in [0, \pi], \theta \in [0, 2\pi)$ and f is the focal radius.

As shown in Figure 4.13, the circumferential direction of each vertex is defined as along θ and the longitudinal direction is along φ.

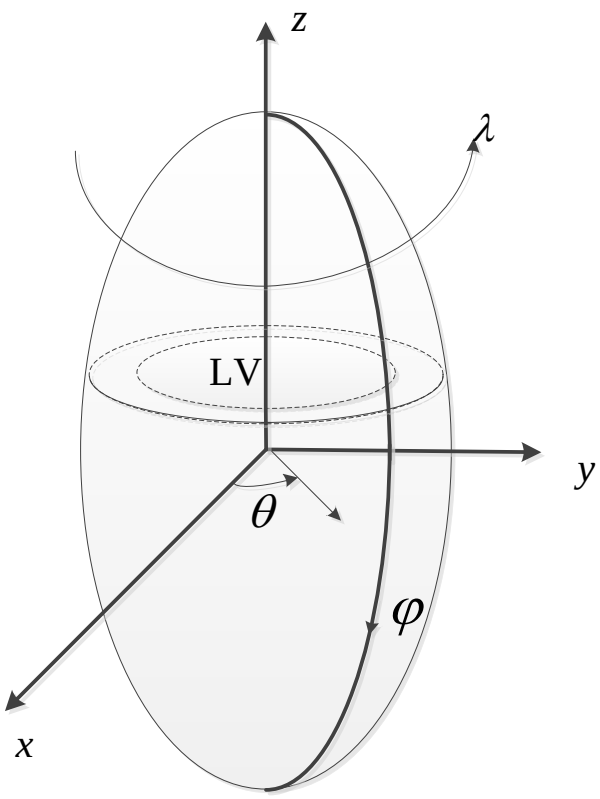

Figure 4.13 Illustration of the LV location in the prolate spheroidal coordinates

For RV mesh, since the RV is not of regular symmetric shape, the circumferential and longitudinal directions are defined differently, as shown in Figure 4.14, referring to [143]. A landmark **q** is located at the origin of aorta, in the right posterior of the annulus fibrosus and closely posterior to the right coronary artery. A landmark **p** is located at the apex of the left ventricle. Figure 4.14 (B) shows the location of **p** and **q** in the 2D image slice with LV long axis view and RV out flow tract view. For any vertex **v** with unit surface normal **n**, let **m** be the unit surface normal of plane (**v**, **p**, **q**) at **v**. The unit longitudinal direction **l** of **v** is then defined as $\mathbf{l} = \mathbf{n} \times \mathbf{m}$ and the unit circumferential direction **c** of **v** is defined as $\mathbf{c} = \mathbf{l} \times \mathbf{n}$.

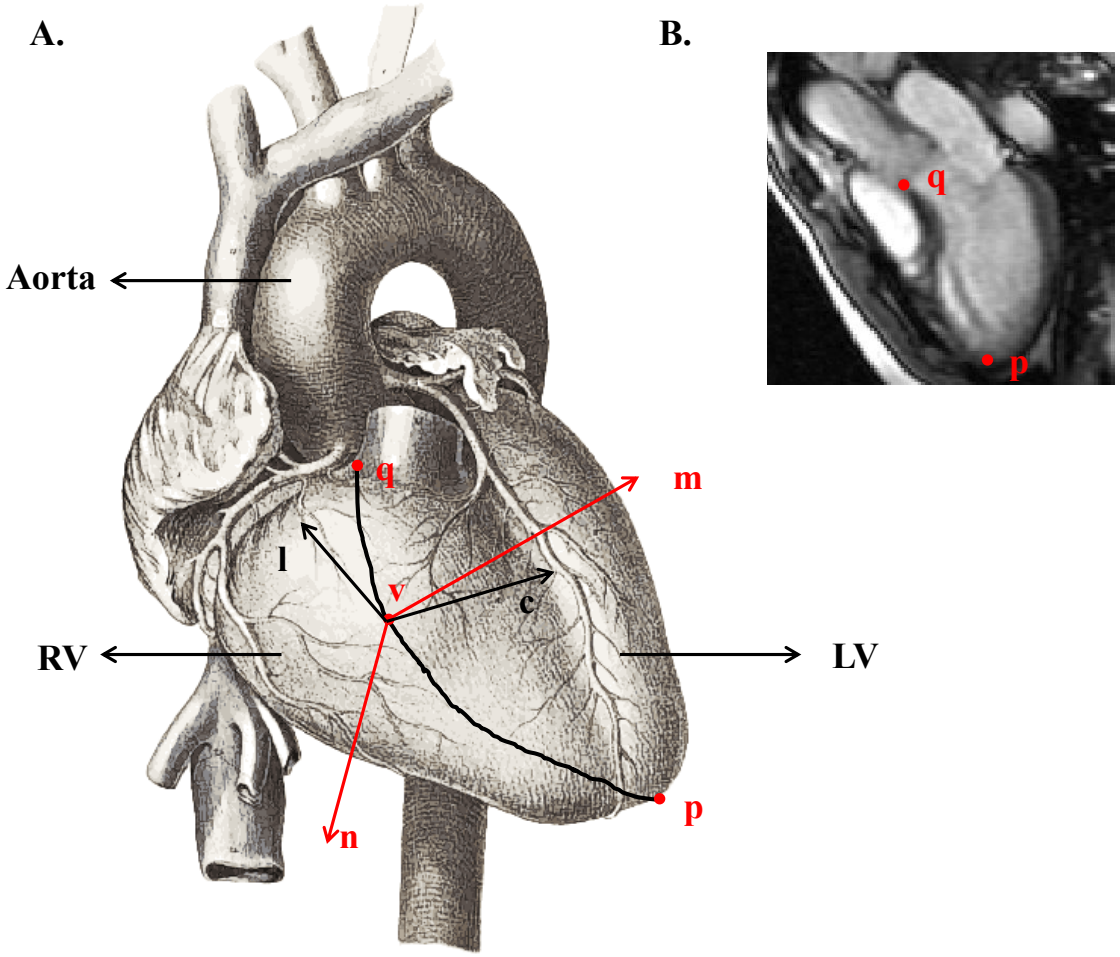

Figure 4.14 Local coordinates on the RV free wall

Heart is adapted from
"http://www.wpclipart.com/medical/anatomy/heart/heart_medical_image.png.html"

For any vertex **v**, the circumferential and longitudinal directions of that vertex in the prolate spheroidal coordinates are defined as $\mathbf{t}_c$ and $\mathbf{t}_l$. The angle between the maximum principle direction $\mathbf{e}_1$ and the circumferential direction $\mathbf{t}_c$ is denoted as $\theta_{\mathbf{t}_c}$ and the angle between the maximum principle direction $\mathbf{e}_1$ and the longitudinal direction $\mathbf{t}_l$ is denoted as $\theta_{\mathbf{t}_l}$. Therefore, the circumferential curvature $k(\mathbf{v}, \mathbf{t}_c)$ of the vertex **v** is calculated as

$$k(\mathbf{v}, \mathbf{t}_c) = k_1(\mathbf{v}) \cos^2 \theta_{\mathbf{t}_c} + k_2(\mathbf{v}) \sin^2 \theta_{\mathbf{t}_c} \quad (4.33)$$

The longitudinal curvature $k(\mathbf{v}, \mathbf{t}_l)$ is calculated as

$$k(\mathbf{v}, \mathbf{t}_l) = k_1(\mathbf{v}) \cos^2 \theta_{\mathbf{t}_l} + k_2(\mathbf{v}) \sin^2 \theta_{\mathbf{t}_l} \tag{4.34}$$

where $k_1(\mathbf{v})$ and $k_2(\mathbf{v})$ are the principle curvatures of vertex **v**.

Besides circumferential and longitudinal curvatures, the surface curvedness at vertex **v** is also defined as

$$k_{curv}(\mathbf{v}) = \sqrt{\frac{k_1^2(\mathbf{v}) + k_2^2(\mathbf{v})}{2}} \tag{4.35}$$

The LV and RV meshes are further split into segments. The LV segments have been defined in [13] and widely used as a standard; but the RV segments have not been officially defined and commonly implemented. In order to define the RV segments, the RV mesh is first transformed to the same prolate spheroidal coordinates as the LV of the same subject, as shown in Figure 4.15 A. Then RV segments are defined on the RV free wall as shown in Figure 4.15 B. Three levels of RV segments, base, mid and apex are defined. The apex level of the RV is corresponding to the distal level of the LV. The basal and mid levels of the RV coincide with the basal and mid levels of the LV. On the RV basal and mid levels, three segments are equally distributed while on the RV apex level, two segments are equally distributed.

Once the segments are defined on the mesh, the vertices can be allocated to each segment. Figure 4.16 shows an example of vertices on a RVED endocardial mesh allocated in each RV segment. The curvature of each segment is calculated as the average curvature of the vertices allocated in that segment.

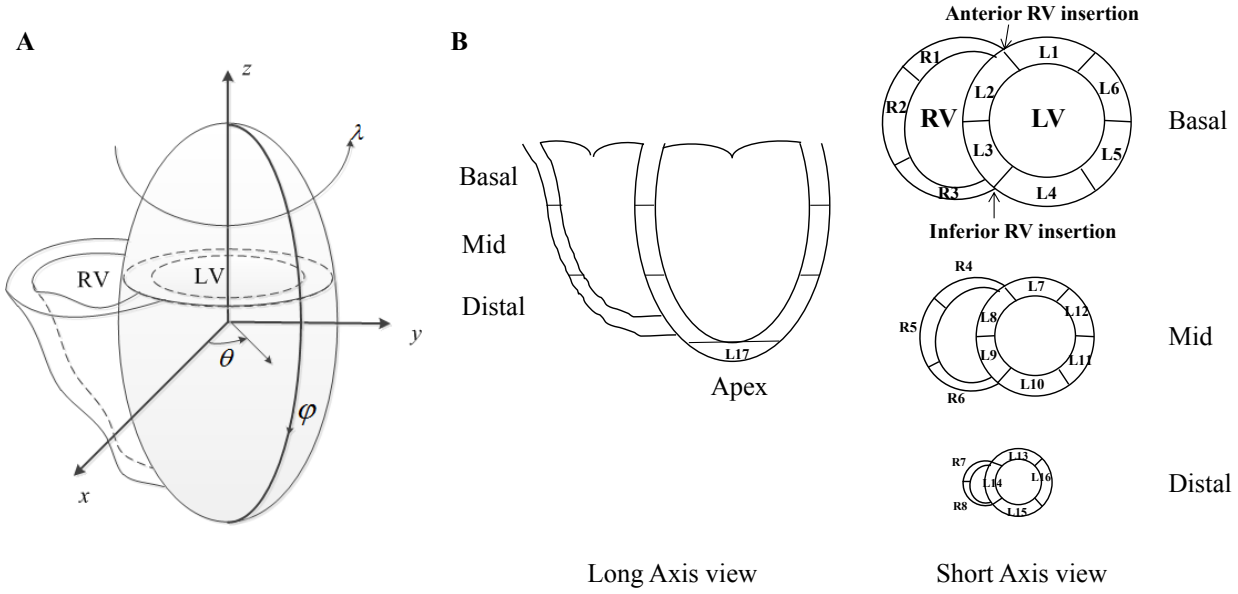

Figure 4.15 Illustration of the LV and RV segments in the prolate spheroidal coordinates

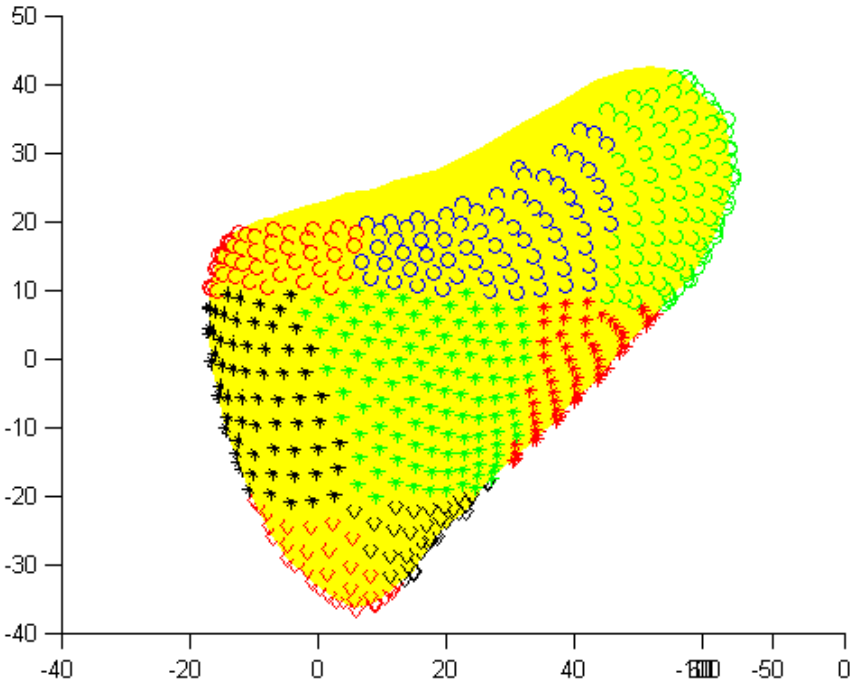

Figure 4.16 Example of the RV segments

Yellow surface, RV mesh with 1000 vertices; ○, vertices allocated in RV segment1; ○, vertices allocated in RV segment2; ○, vertices allocated in RV segment3; *, vertices allocated in RV segment4; *, vertices allocated in RV segment5; *, vertices allocated in RV segment6; ◊, vertices allocated in RV segment7; ◊, vertices allocated in RV segment8.

4.6 Results

4.6.1 Study Population

Fifty three normal subjects (45 ±14 years; 54% female) were selected for this study. Among them, seventeen subjects were randomly selected as training samples while the other thirty six subjects were used as test samples. For comparison purposes, twelve patients with chronic mitral regurgitation (MR) and twelve patients with pulmonary hypertension (PH) were selected for the study as well. Within each group, six patients were randomly selected as training samples and the other six patients were used as test samples.

cMR was performed for all subjects on a 1.5-T MRI scanner (Signa, GE Healthcare, Milwaukee, Wisconsin) optimized for cardiac imaging. Electrocardiographically gated breath-hold steady-state free precision technique was used to obtain standard (2-, 3-, and 4-chamber long axis and serial parallel short-axis) views using the following typical parameters: slice thickness of the imaging planes = 8 mm, field of view = 40 cm, scan matrix = 256 × 128, flip angle = 45 °, repetition/echo times = 3.8/1.6 ms.

For the training samples in each group (i.e. the normal group, the MR group, and the PH group), the proposed mesh generation algorithm was performed on each ventricle. New meshes from the test set were generated by deforming their corresponding PDM towards their 3D segmentations according the method described in Section 4.5.2.

4.6.2 Model Performance Validation

In this section, we studied and validated the performance of the proposed model in several ways.

Since the smoothness of the meshes generated by the proposal model was affected by the triangulation as well as other model parameters, such as the number of singularities M and the

tuning parameter γ of the smoothing function, we utilized mathematical objects such as sphere and prolate spheroid to test the effect of these parameters on curvature error. The reason of using sphere and prolate spheroid was that the true curvatures on these objects were known. Furthermore, a prolate spheroid with $\varphi > \pi/3$ was similar to the shape of a normal LV. We first generated triangulated meshes on these objects without mapping, such that there was no curvature error introduced by the mapping. By varying the number of vertices and the ratio of the semi-minor to semi-major axes of the prolate spheroid, we studied the curvature error by triangulation. Then we generated triangulated meshes on a prolate spheroid with $\varphi > \pi/3$, which was considered as a perfect normal LV, through mapping using the proposed method. The effect of M and γ on the smoothness of the generated meshes was studied and the optimum values of M and γ were selected for the proposed model.

The quality of the performance of AMM was tested. The training sets we used in this study to construct AMM were rather small. The possible influence of the small sample size was that AMM could not capture the features of the new subject out of the training set. We therefore studied the influence of the small sample size on the performance of several AMMs and selected the optimal AMM for the rest of the study.

The clinical measurements, such as volumes and curvatures derived from the proposed method, were validated. The conventional way of computing ventricular volumes was to sum up the volumes defined by contours and multiplied by slice thickness. This method has resulted in huge difference between RVSV and LVSV (see Table 2.2) due to the contour errors at the base of the heart. We therefore studied the difference between RVSV and LVSV in the normal test set generated by the proposed model to test whether the proposed method could provide a more accurate measurement of stroke volume.

A B-spline surface model [38] based on prolate spheroidal coordinate system (PSB) has been used in-house to compute circumferential and longitudinal curvatures of LV at basal, mid and distal levels. This method was considered as a "gold standard" and was compared to the proposed method in terms of their LV curvature measurements.

Furthermore, we looked into the data to see whether the clinical measurements generated by the proposed model could distinguish the difference between pathologies. Boxplot was used to observe the difference in RV end-diastolic volume (RVEDV) between the normal test set and the PH test set (a group known to have enlarged RVEDV[144]). Boxplot was also performed to observe the difference in the LVSV between the normal test set and the MR test set (a group known to have bigger LVSV due to the regurgitant flow into the left atrium during contraction [42]), and the apex curvatures measured by the proposed method between the normal test set and the MR test set (a group known to have a more spherical LV due to eccentric remodeling [42]).

The details of the test procedure and results are presented in the rest of this section. All data are presented as mean $\pm$ standard deviation (SD). A $P < 0.05$ was considered statistically significant. All statistical analyses were performed using SAS version 9.2.

4.6.2.1 *Curvature Error by Triangulation*

A sphere with radius R = 70 mm was triangulated with V vertices. The true curvature of the sphere was equal to $k = 1/R = 0.0143$(1/mm). The curvature at each vertex was calculated using the method described in Section 4.5.3.2 and compared to the true curvature. Figure 4.17 shows the curvature errors by triangulation versus the number of vertices V. The error was decreased as V increased. For V greater than 1000, the curvature error was around 1.4%.

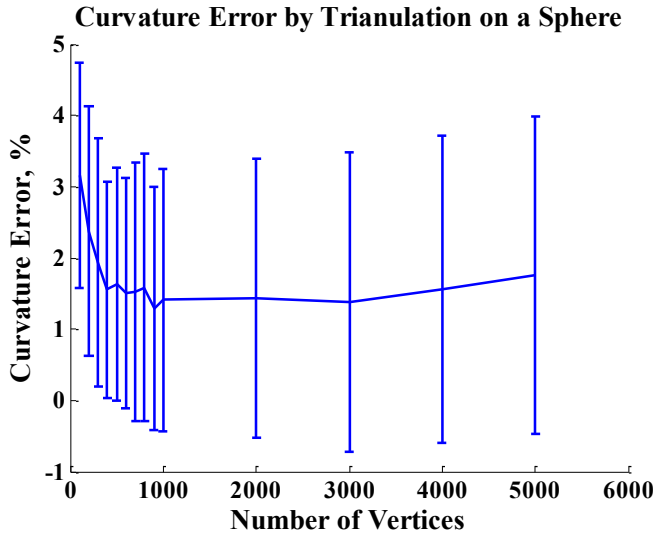

Figure 4.17 The curvature error by triangulation on a perfect sphere.
The curvature error is displayed as mean $\pm$ std, the radius of the sphere is 70mm and the true curvature at each vertex is equal to $1/R = 0.0143$(1/mm). std: standard deviation.

Each triangulated sphere with various V was then mapped to a prolate spheroid as shown in Figure 4.18 A. The semi-major axis of the prolate spheroid was set equal to R and the semi-minor axis was set equal to $2R/3$. A perfect normal LV heart was then represented as the prolate spheroid with $\varphi > \pi/3$ as shown in Figure 4.18 B. φ was a parameter in the prolate spheroid coordinates $(\theta, \varphi, \lambda)$. The transformation between the Cartesian coordinates to the prolate spheroid coordinates was layout in Equation 4.32.

For each vertex on the perfect LV, the true maximum, minimum, circumferential and longitudinal curvatures were calculated using standard formula [30]. The maximum, minimum, circumferential and longitudinal curvatures of each vertex on the triangulated mesh were calculated as described in Section 4.5.3.2 and compared with their true values. Figure 4.19 shows the curvature errors (%) vs. the number of vertices. It indicates that the curvature errors did not improve significantly as V increased on a prolate spheroid mesh. The maximum and

circumferential curvatures at V = 1000 were about -5% and the minimum and longitudinal curvatures at V = 1000 were about +8%.

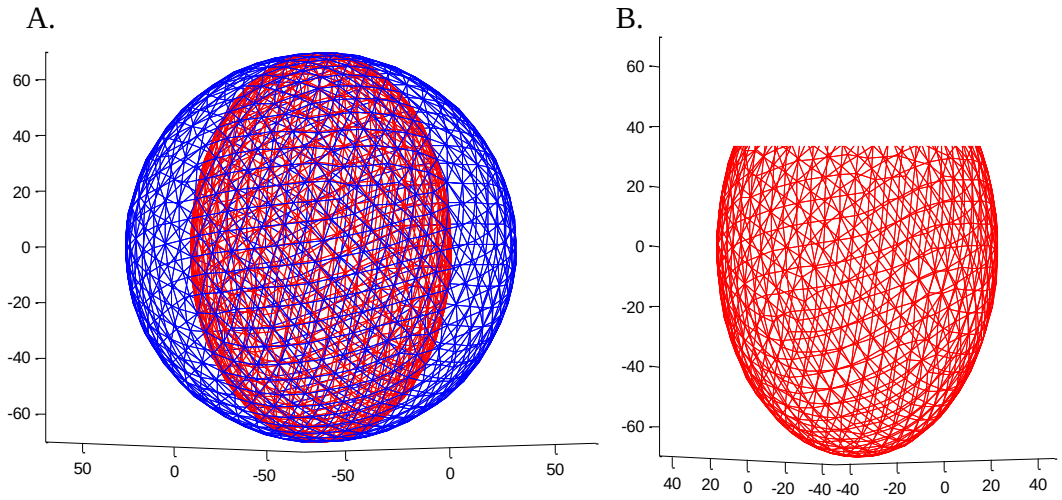

Figure 4.18 Illustration of a prolate spheroid and a perfect normal LV
(A.) Blue triangulated mesh: the original sphere with R = 70 mm; red triangulated mesh: the prolate spheroid mapped from the sphere with semi-major axis = R = 70 mm and the semi-minor axis = 2R/3. (B.) A perfect normal LV

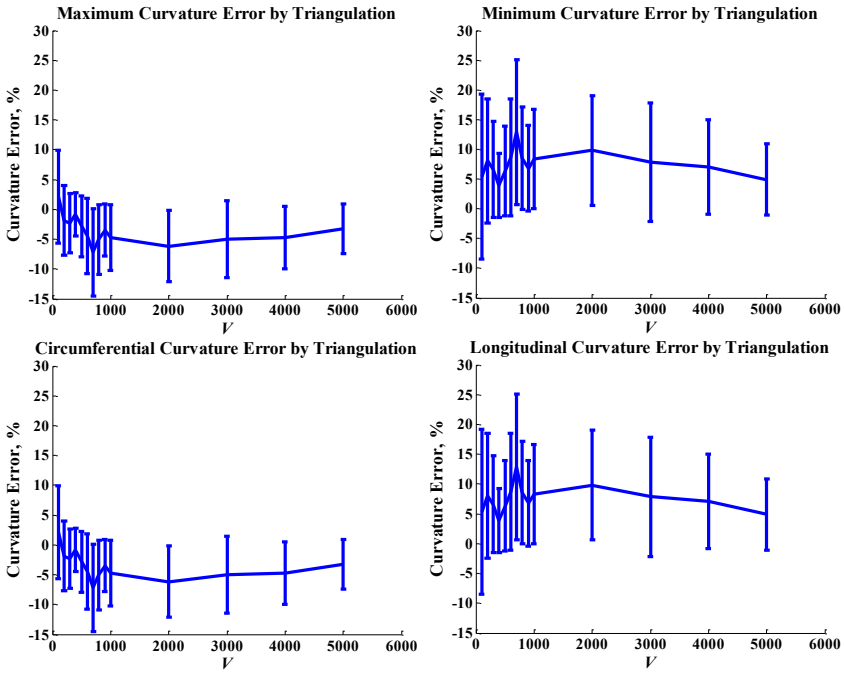

Figure 4.19 The curvature errors on the perfect LV versus V
The curvature error is displayed as mean ± std. The perfect LV is represented by a prolate spheroid with the semi-major axis=70mm , the ratio of semi-minor/semi-major = 2/3 and $\varphi > \pi/3$.

Furthermore, we tested the curvature errors on the perfect LV by varying the ratio of semi-minor axis to semi-major axis. Set V=1000. Figure 4.20 shows the curvature errors from triangulation on the perfect LV by varying the ratio of semi-minor axis to semi-major axis of the perfect LV. It shows that the errors increased significantly as the ratio decreased.

For a real normal heart, the ratio of dimension to length was about 2/3, and for a diseased heart, such as a MR heart, the ratio was higher than 2/3 due to the remodeling. Therefore, the curvature errors by triangulation on hearts with different pathology should be within a manageable range.

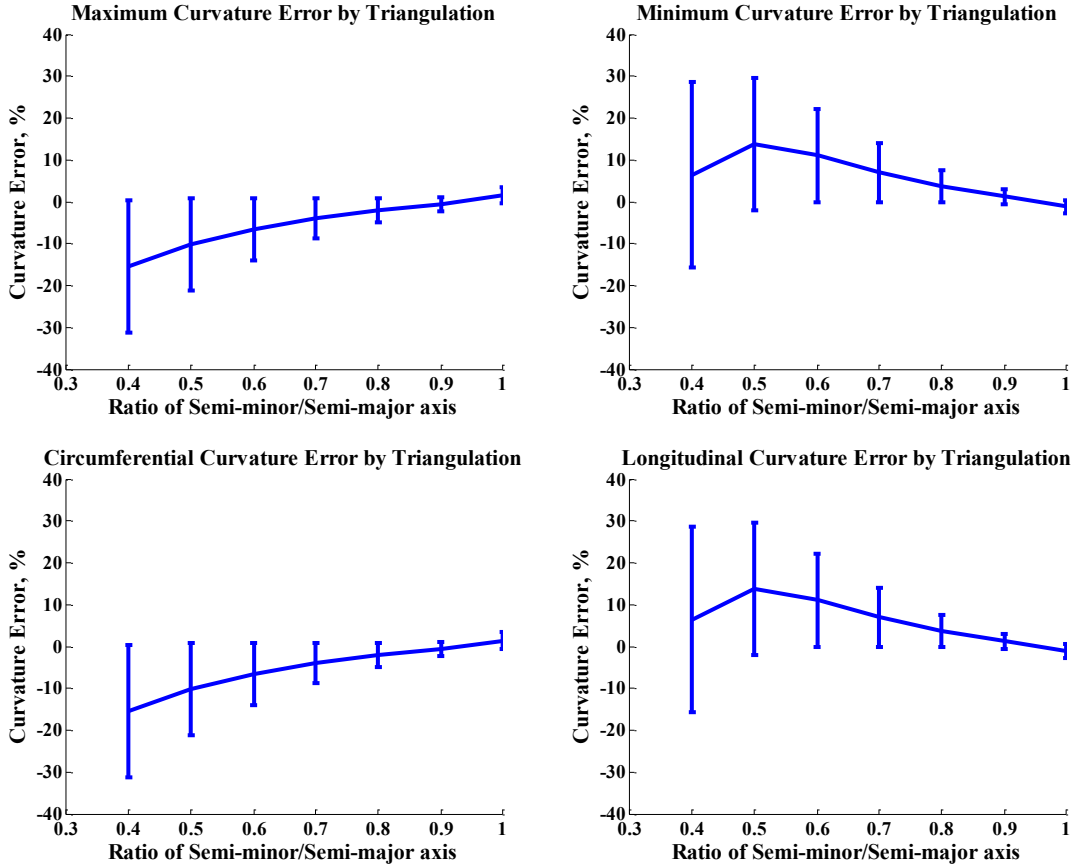

Figure 4.20 The curvature errors on the perfect LV by increasing semi-minor to semi-major axis ratio

The curvature error is displayed as mean $\pm$ std. The number vertices V on these meshes were 1000. The perfect LV is represented by a prolate spheroid with $\varphi > \pi/3$ and semi-major axis=70mm.

At last, we tested the curvature errors on each segment level (Base, Mid, Distal and Apex) of the perfect LV. The definition of each segment level was described in Section 4.5.3.2. Figure 4.21 shows the curvature errors (%) at different segment levels. It indicates that the curvature errors (%) were highest at the base level and lowest at the apex level. Figure 4.22 shows the curvature errors (1/mm) at different segment levels. It indicates that the curvature errors did not vary much by levels. However the true curvatures were higher at the apex resulting in the lower percentage error at the apex compared to that at the base.

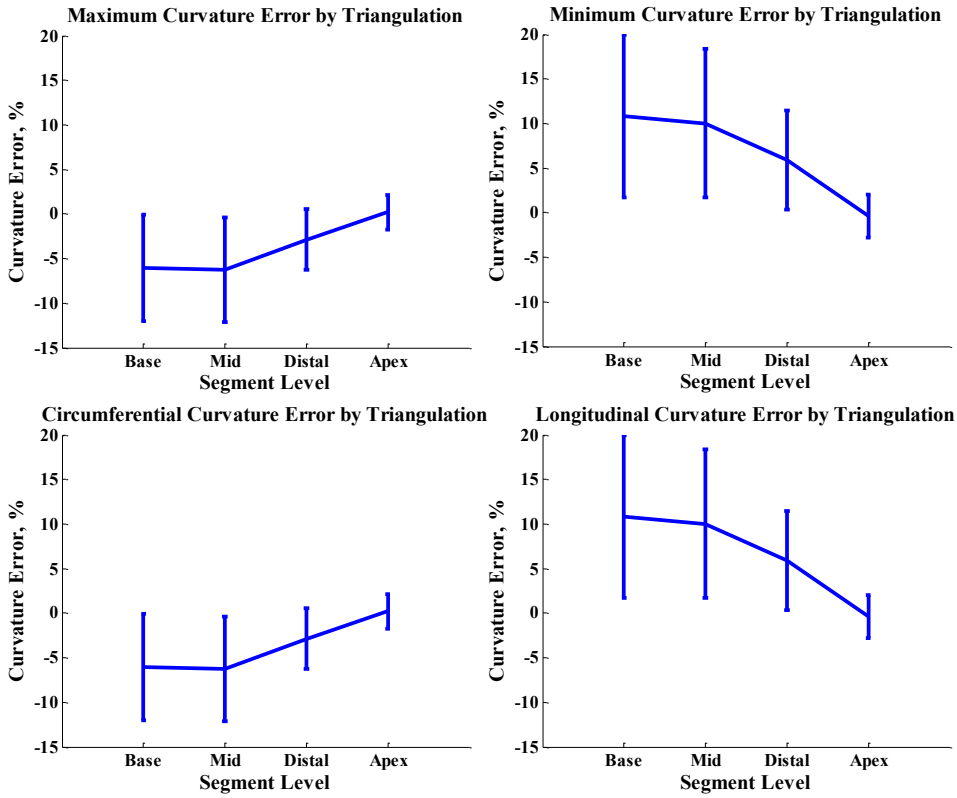

Figure 4.21 The curvature errors versus segment levels
The curvature error is displayed as mean $\pm$ std. The number of vertices V on these meshes is 1000. The perfect LV is represented by a prolate spheroid with ratio of semi-minor to semi-major axis equal to 2/3 and $\varphi > \pi/3$.

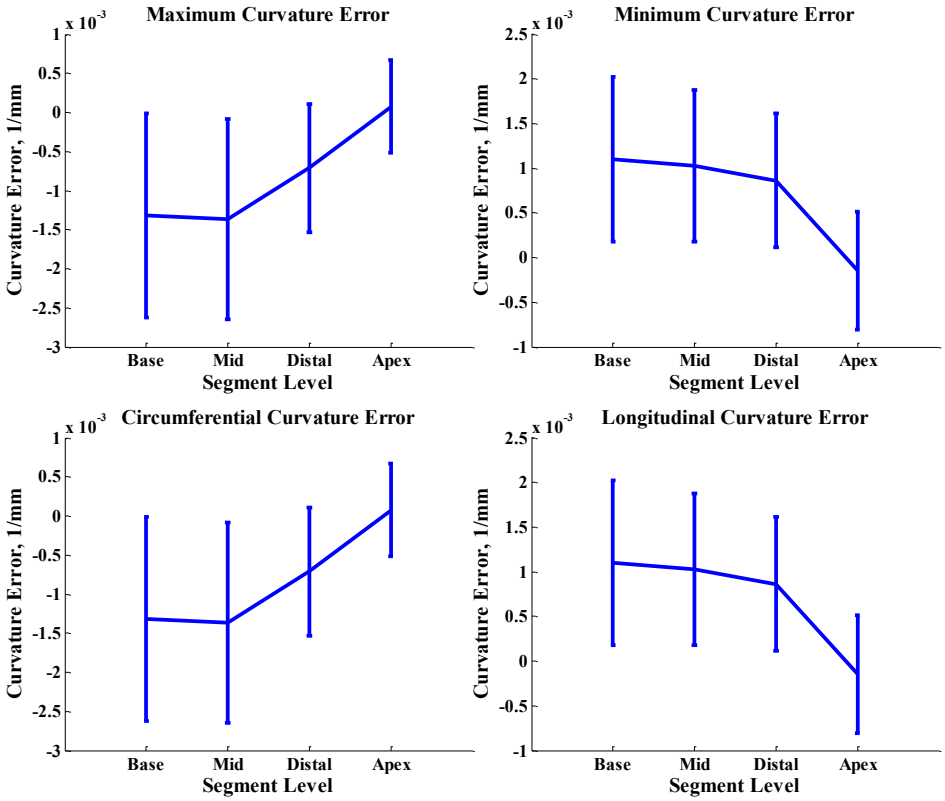

Figure 4.22 The raw curvature errors versus segment levels

The curvature error is displayed as mean $\pm$ std. The number of vertices V on these meshes is 1000. The perfect LV is represented by a prolate spheroid with ratio of semi-minor to semi-major axis equal to 2/3 and $\varphi > \pi/3$.

4.6.2.2 *Optimal Model Parameters*

Based on the experiments in Section 4.6.2.1, triangulation on a perfect LV shape could introduced 5% to 8% curvature error with the number of vertices equal to 1000. Furthermore, the behavior of the circumferential curvature on the perfect LV was similar to that of the maximum curvature, whereas the behavior of the longitudinal curvature was similar to that of the minimum curvature. This indicates that the circumferential direction of the heart was close to the maximum principle direction, whereas the longitudinal direction was close to the minimum principle direction.

In this section, we studied the effect on curvature error by varying the following model parameters: the number of singularities M and the tuning parameter γ of the smoothing function. The number of singularities M controlled the smoothness of the underlying continuous surface. The value of γ in the smoothing function controlled the smoothness of the triangulated surface. M and γ were set such that the surface curvature error was within a tolerance with acceptable goodness of fit.

Given V = 1000, we generated a sequence of meshes to the perfect LV (See Figure 4.18 B) versus the number of singularities M. Note that, in this experiment, the smoothing function was not applied. The smoothing function would be applied in the next experiment after M was set such that the effect of the smoothing function to the surface smoothness could be validated. The propagation of the each vertex $\mathbf{v}$ stopped when $u(\mathbf{r}(t)) = S(\mathbf{v}/|\mathbf{v}|)$ (See Section 4.3). Figure 4.23 shows that the curvature errors (%) versus M.

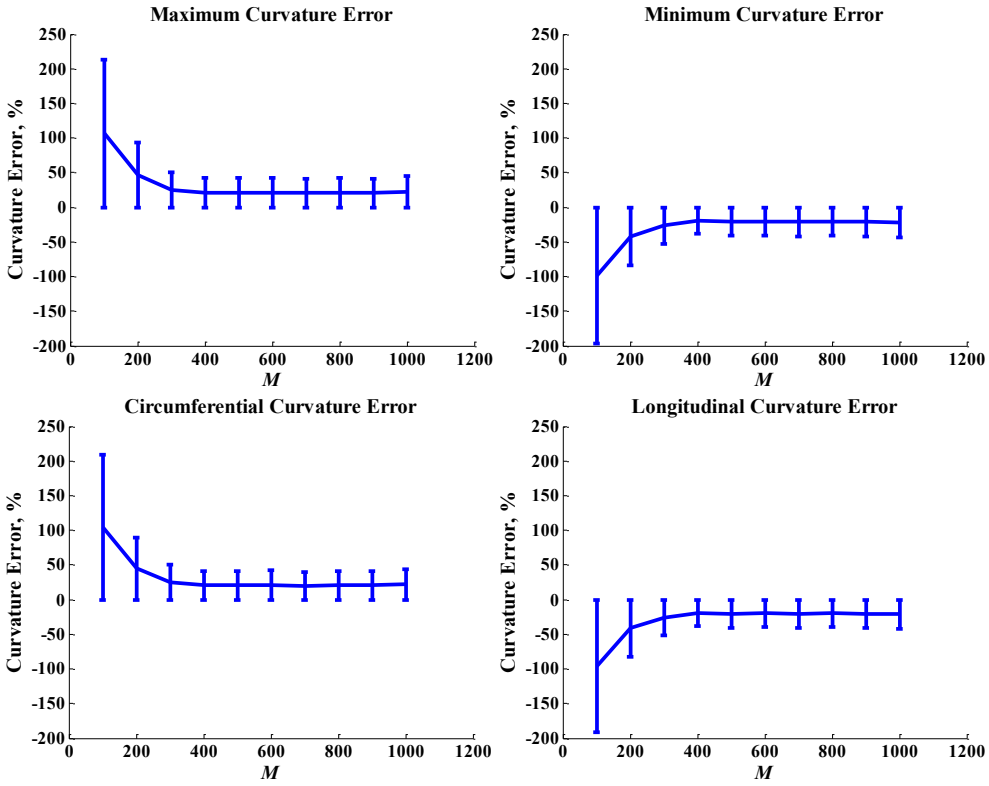

Figure 4.23 The curvature errors versus *M*

This test is performed without applying the smoothing function. Data is presented as mean ±std. The curvature errors are all decreased as *M* increases. As *M* is greater than 400, the absolute errors converge to about 25%.

Figure 4.23 indicates that as *M* increased, the absolute curvature errors reduced. However, for *M* greater than 400, the improvement of curvature error leveled. The minimum curvature error as $M > 400$ was about 20% to 25% without the smoothing function.

As a result, we set $M = 400$. Then we generated a sequence of meshes by applying the smoothing function and varying the tuning parameter γ. Figure 4.24 shows the curvature error versus γ.

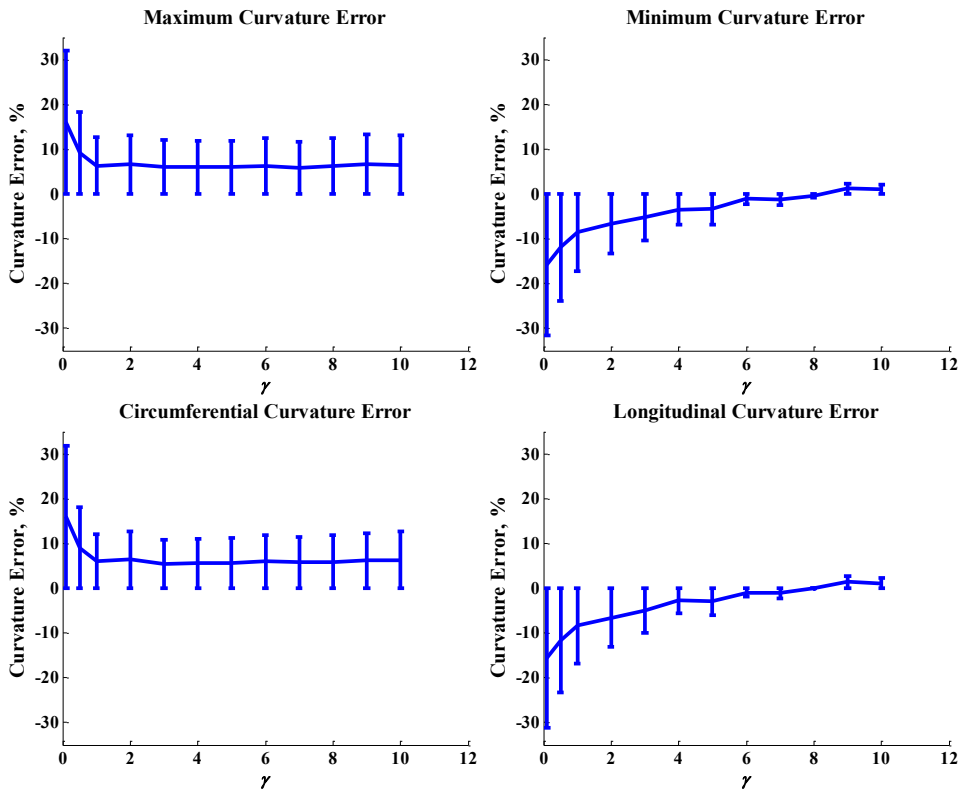

Figure 4.24 The curvature errors by increasing γ
Data is presented as mean ±std.

Compared to the curvature errors (Figure 4.23) without applying the smoothing function, Figure 4.24 shows that the smoothing function has reduced the curvature errors and improved the smoothness of the surface significantly. As γ increased, the curvature error decreased. For the maximum and circumferential curvatures, the curvature errors were about 7% when $\gamma > 1$. For the minimum and longitudinal curvatures, the errors were consistently decreased as γ increased. But the speed of decreasing reduced as $\gamma > 6$.

Meanwhile, the goodness of fit of the triangulated mesh to the surface was calculated in two forms, volume error and mesh distance. The volume error was calculated as the volume difference between the mesh and the true surface (as shown in Figure 4.18 B). Figure 4.25 A shows the volume error versus γ. It shows that the volume error first decreased when $\gamma < 4$ and then increased as $\gamma \geq 4$. However, when γ was within 10, the volume error was small enough to

be ignored. To quantify the mesh distance, the mesh shown in Figure 4.18 B was considered as a gold standard. For each vertex **v** on the triangulated mesh generated by the proposed method, we found its closest vertex **p** on the gold standard. If the closest vertex of **p** on the proposed mesh was also **v**, **p** and **v** were defined as a pair of vertices and their distances were calculated. The mesh distance was then defined as the mean of the distances of all pairs of vertices [120]. Figure 4.25 B shows the mesh distance versus γ. It illustrates that the mesh distance did not vary a lot as γ was within 10.

Considering both curvature errors and goodness of fit, γ was set equal to 6 for our proposed model.

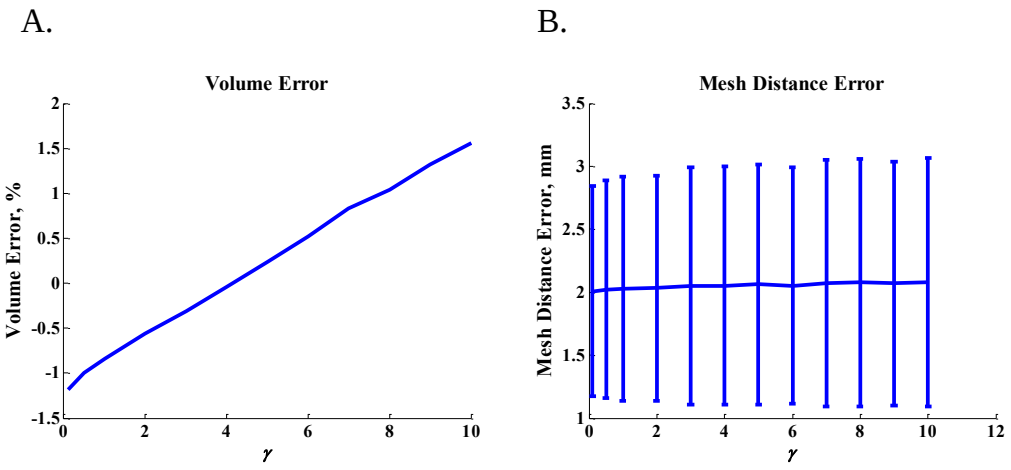

Figure 4.25 The mesh goodness of fit by increasing γ
Data on the right is presented as mean ±std

In conclusion, the optimal parameters set for the proposed model were $V = 1000$; $M = 400$; and $\gamma = 6$.

Figure 4.26 visually shows that the triangulated meshes generated by the proposed method were well matched with their fitted contours for both the LV and RV. Surface color represents the surface curvedness.

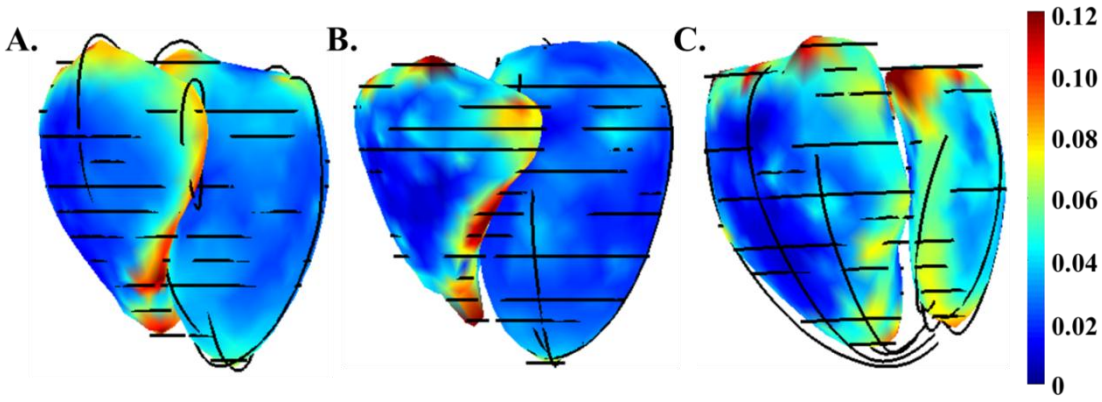

Figure 4.26 Illustration of the deformed triangulated surfaces with fitted contours
Triangulated surface representations of LV and RV ED endocardium with fitted contours (black lines) of a normal subject **(A)**, a MR patient **(B)** and a PH patient **(C)** using color scales of their surface curvedness. The MR heart has a bigger LV chamber with less curvedness at the apex while the PH patient has a bigger RV chamber. LV: left ventricle; RV: right ventricle; ED: end-disatole.

4.6.2.3 *AMM Performance*

Due to the small sample size of the training sets, the quality of the performance of AMM was tested based on the different point distribution models (PDM) they utilized.

Let AMM1 denote the deformable models based on ventricle and pathology specified PDMs. This means the training sets used to generate PDMs had certain ventricle and pathology. AMM1 would only be applied to the same ventricle of new subjects with the same pathology as their training set.

Let AMM2 denote the deformable models based on pathology specified and ventricle non-specified PDMs. This means the training sets used to generate PDMs had certain pathology but included both LV and RV of the training samples. Therefore, AMM2 could be applied to both LV and RV of new subjects with the same pathology as its training set. Since the LV and RV had complete different shapes, mixing these two types of shapes would increase the variance of the training set significantly.

Let AMM3 denote the deformable models based on ventricle specified and pathology non-specified PDMs. This means the training sets used to generate PDMs had certain ventricle but include all types of subjects (normal, MR and PH). Therefore, AMM3 could be applied to the same ventricle (as its training set) of new subjects with any pathology. Since it was known that MR patients have enlarged LV and PH patients had dilated RV, compared with the normal group, mixing training subjects with different pathologies would certainly increase the variance of the training set.

To test the performance of AMM1, AMM2 and AMM3, these three models were applied to the normal test set. The LV and RV stroke volumes were computed from the generated meshes. The stroke volume difference (LVSV-RVSV, ml) of the normal test set were then compared between AMM1 and AMM2, AMM3 visually using boxplots.

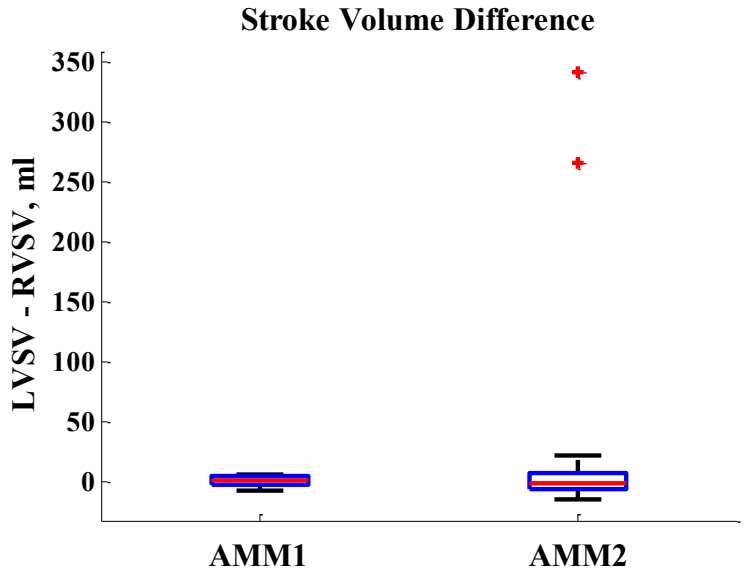

Figure 4.27 Compare AMM1 versus AMM2 based on the stroke volume difference
AMM1, the deformable models based on ventricle and pathology specified PDMs; AMM2 denote the deformable models based on pathology specified and ventricle non-specified PDMs; On each box, the central red mark is the median, the blue edges of the box are the 25th and 75th percentiles, the black whiskers represent the most extreme data points that are considered to be not outliers; +, outliers.

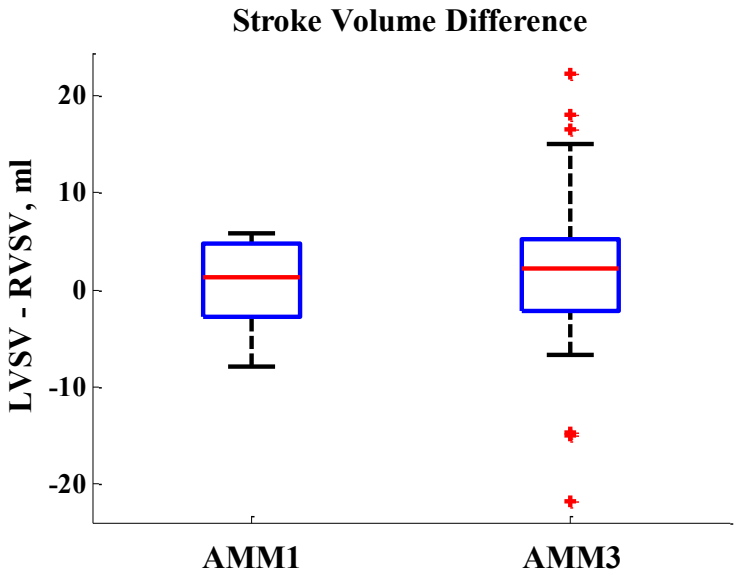

Figure 4.28 Compare AMM1 versus AMM3 based on the stroke volume difference
AMM1, the deformable models based on ventricle and pathology specified PDMs; AMM3 denote the deformable models based on ventricle specified and pathology non-specified PDMs; On each box, the central red mark is the median, the blue edges of the box are the 25th and 75th percentiles, the black whiskers represent the most extreme data points that are considered to be not outliers.

Figure 4.27, Figure 4.28 show that the variance of the stroke volume difference (LVSV-RVSV, ml) of the normal test set was smallest when the PDM was ventricle and pathology specified. This indicates that by reducing the variance of the training set, AMM could capture and generate more accurate meshes to test subjects with the same specifications as their training set. Therefore, AMM based on ventricle and pathology specified PDM was used in the rest of the study.

4.6.2.4 *LV and RV Stroke Volume Comparison*

In this section, we validated the model by comparing LVSV and RVSV measurements of the normal test set derived by the proposed model. The difference between LVSV and RVSV in the normal test set was not significantly different from zero (0.64 ± 4.28 ml, $P = 0.3721$). The correlation analysis and Bland-Altman plot of the LVSV versus RVSV of the normal test set are shown in Figure 4.29. It indicates that the LVSV and RVSV in the normal test set measured by

the generated meshes were significantly correlated (ρ = 0.9635, P < 0.0001) and had a very good agreement. Comparing this result with Table 2.2 in the first study, it indicates the proposed model generated more accurate volume measurements compared with the conventional volume computation method, which was summing up the volumes defined by the contours and multiplying it with slice thickness, therefore providing better volumetric analysis in clinical studies.

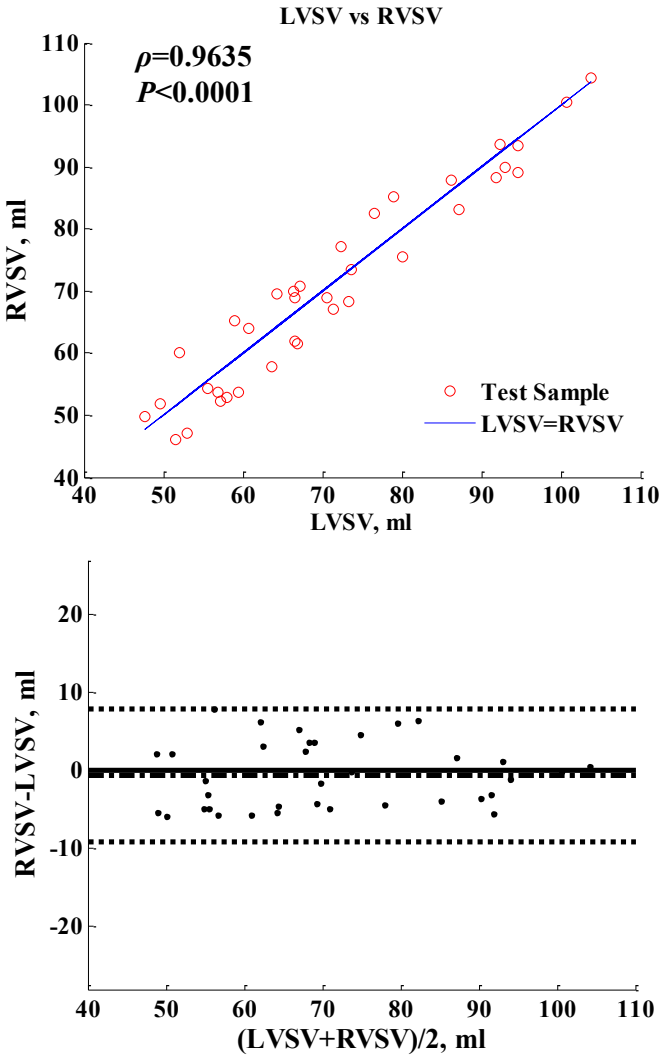

Figure 4.29 Correlation analysis and Bland-Altman plot of LVSV versus RVSV
– · –, mean line; ····· , mean ±2SD; **——**, equal line; LVSV: left ventricular stroke volume; RVSV: right ventricular stroke volume.

4.6.2.5 *PSB versus the Proposed Method*

Correlation analysis of LV circumferential curvatures between PSB and the proposed method shows that the results calculated from these two methods were significantly correlated. Figure 4.30 shows the scatter plot and correlation analysis results of the endocardium circumferential curvatures at LVED and LES between PSB and the proposed method.

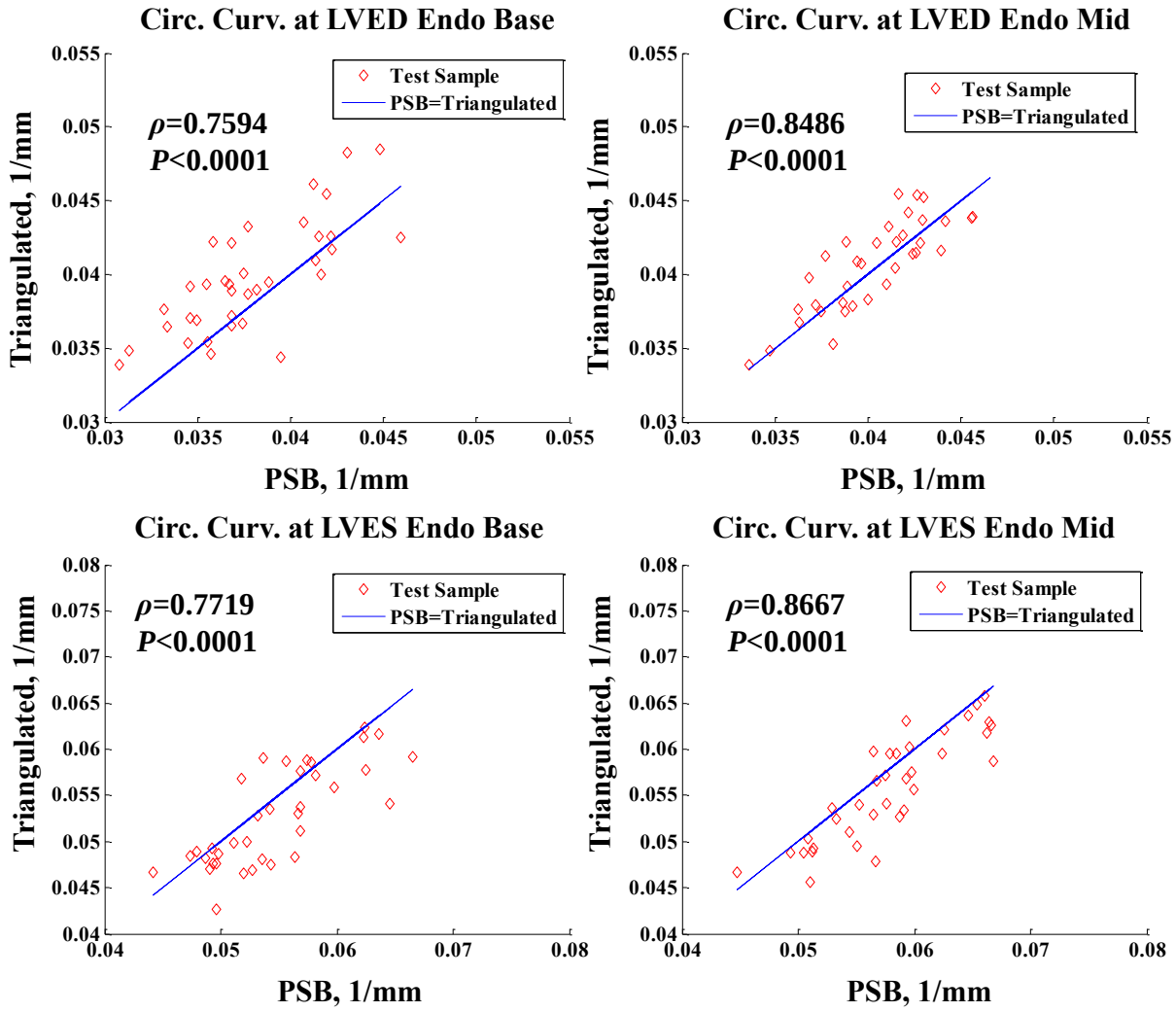

Figure 4.30 Scatter plot and correlation analysis of circumferential curvatures between PSB and Triangulated

Circ. Curv., circumferential curvature; ED, end-diastole; ES, end-systole; Endo: endocardium; PSB: Prolate Spheroidal B-spline method; Triangulated, the proposed biventricular active mesh model. ρ:correlation coefficient; *P*: *P* value of the correlation analysis result.

The Bland-Altman plots shown in Figure 4.31 indicate that the proposed method had a good agreement with the "gold standard" in terms of the circumferential curvature measurements. The differences in endo circumferential curvature between the two methods were within 13% at the basal level and within 8% at the mid level.

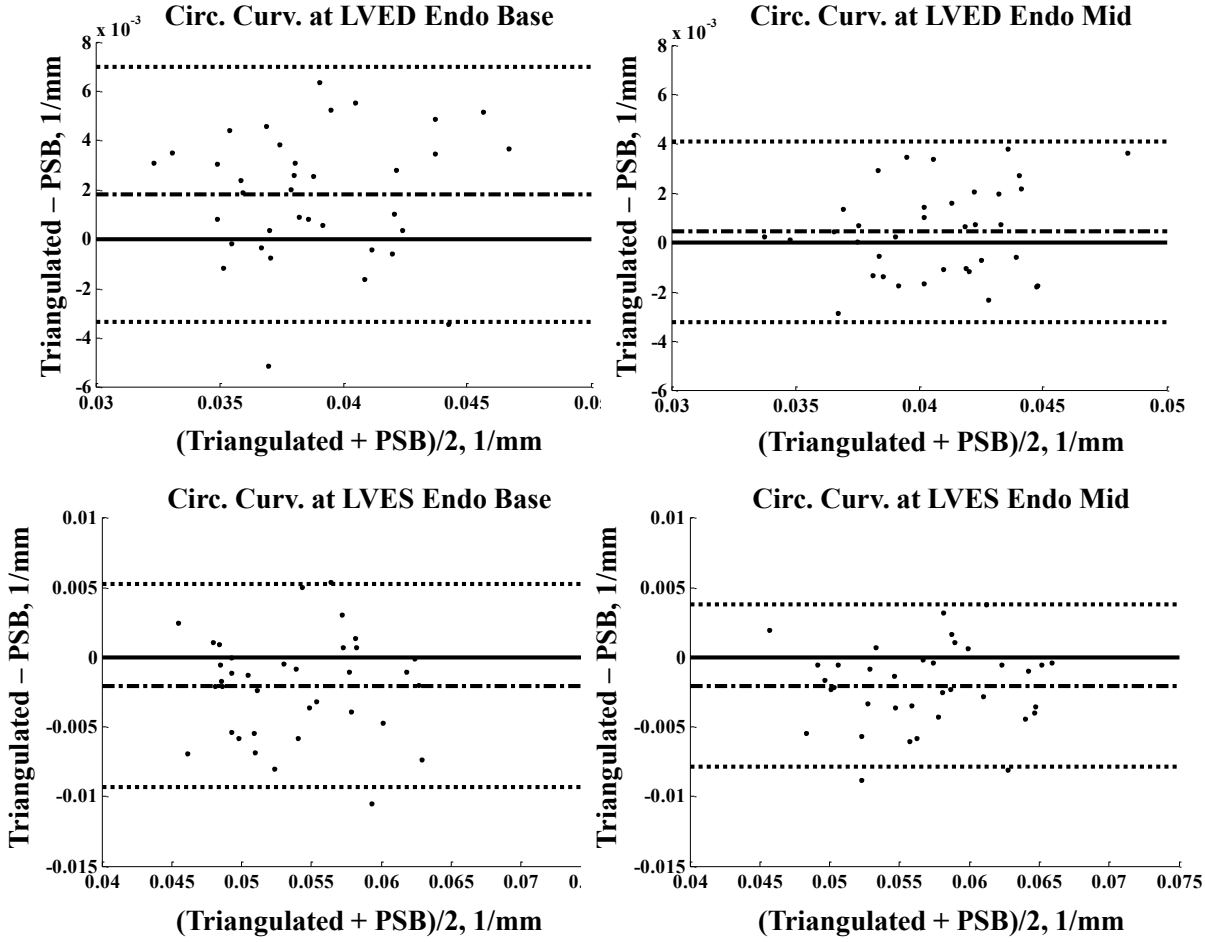

Figure 4.31 Bland-Altman plot of circumferential curvature comparison
– · –, mean line; ····· , mean ±2SD; ——, equal line; PSB, Prolate Spheroidal B-spline method; Circ. Curv., circumferential curvature; ED, end-diastole; ES, end-systole; Endo, endocardium.

Correlation analysis of the LV endocardium longitudinal curvatures between PSB and the proposed method shows that the measurements calculated from these two methods were significantly correlated in both LVED and LVES expect at LVES basal level. However, the scatter plot shown in Figure 4.32 and the Bland-Altman plot shown in Figure 4.33 indicate that

the longitudinal curvatures calculated by the triangulated mesh were smaller at the basal level and higher at middle level compared to that measured by PSB.

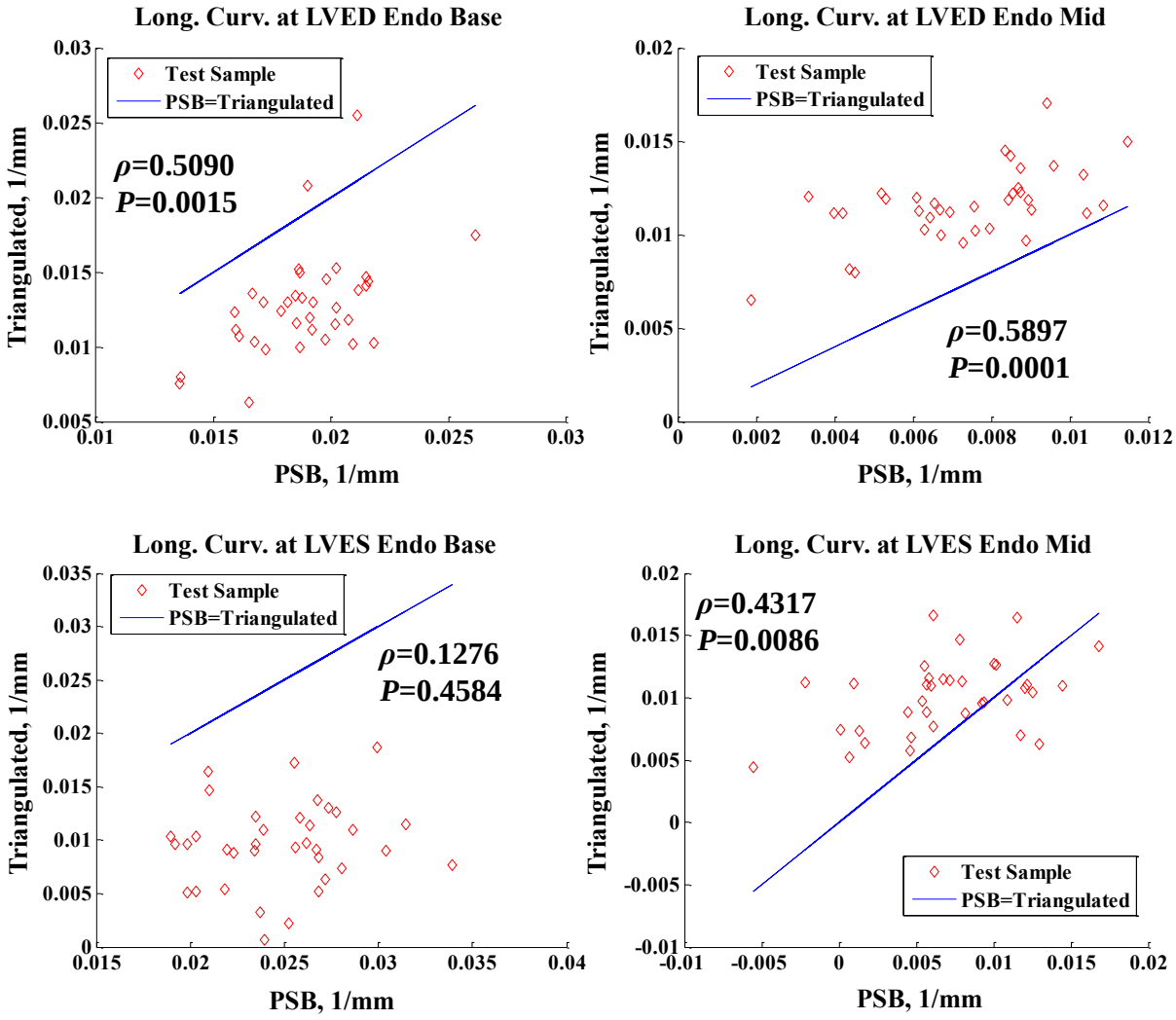

Figure 4.32 Scatter plot and correlation analysis of longitudinal curvatures between PSB and the proposed method

Long. Curv., longitudinal curvature; ED, end-diastole; ES, end-systole; Endo, endocardium; PSB: Prolate Spheroidal B-spline method; Triangulated, the proposed biventricular active mesh model; ρ:correlation coefficient; *P*: *P* value of the correlation analysis result.

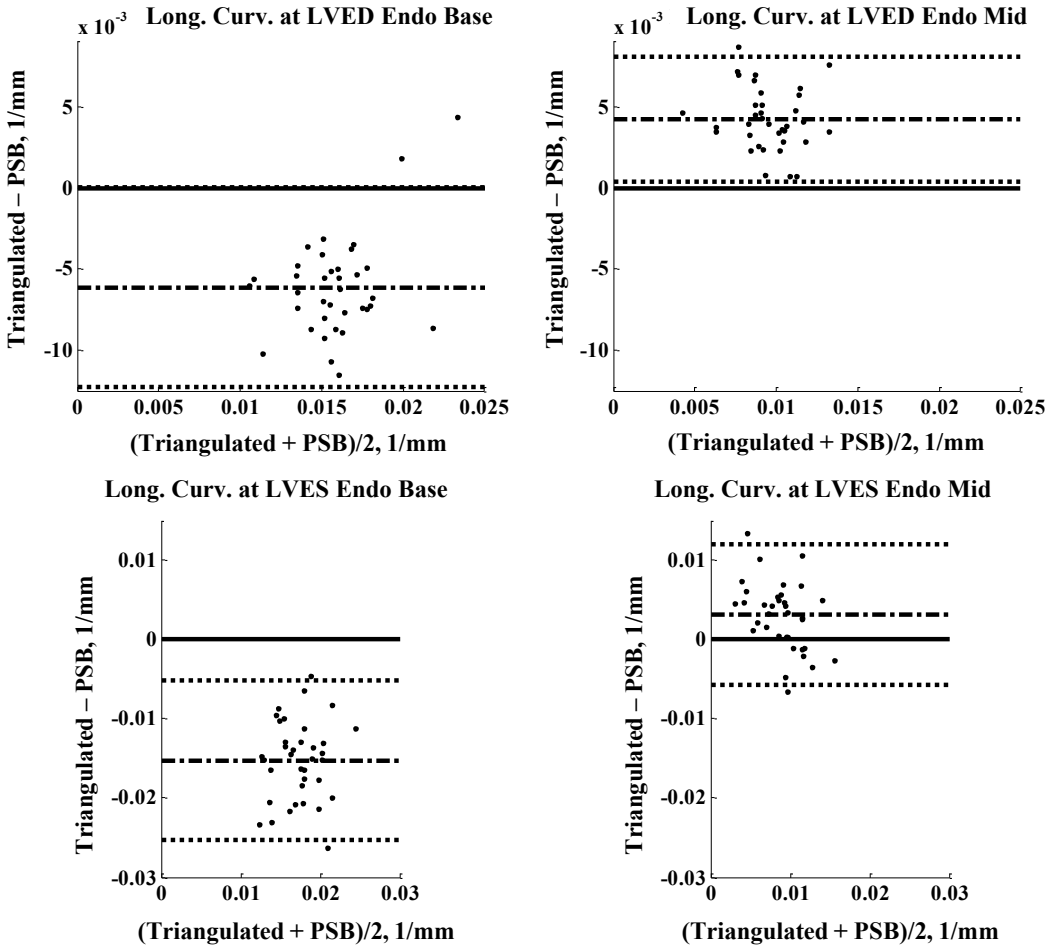

Figure 4.33 Bland-Altman plot of longitudinal curvature comparison
– · –, mean line; ····· , mean ±2SD; ——, equal line; PSB, Prolate Spheroidal B-spline method; Long. Curv., longitudinal curvature; ED, end-diastole; ES, end-systole; Endo, endocardium.

One possible reason for these differences is that the proposed method utilized both short axis contours and long axis contours equally to generate the 3D segmentation to which the triangulated mesh was fitted, whereas PSB weighed more on the short axis contours than the long axis contours to generate the fitted surface. Since the longitudinal curvatures could be affected by the long axis contours heavily, the generated surfaces by these two methods may have different longitudinal curvatures. Also, PSB was the B-spline surface model based on prolate spheroidal coordinate system, so there was a singularity at the LV apex using PSB.

Therefore, PSB was not able to model the apex. This may potentially affect the surface curvedness in the longitudinal direction of the generated surface.

Figure 4.34 demonstrates an example of a LVES surface from the normal test set fitted by the proposed method (left) and PSB (right). As indicated by the red arrows, the mid-ventricle of the surface fitted by the proposed method (on the left) was more flat compared that fitted by PSB (on the right), which was slightly concave. The surface fitted by the proposed method was influenced by both long axis and short axis contours equally whereas the surface fitted by PSB was more determined by the short axis contours.

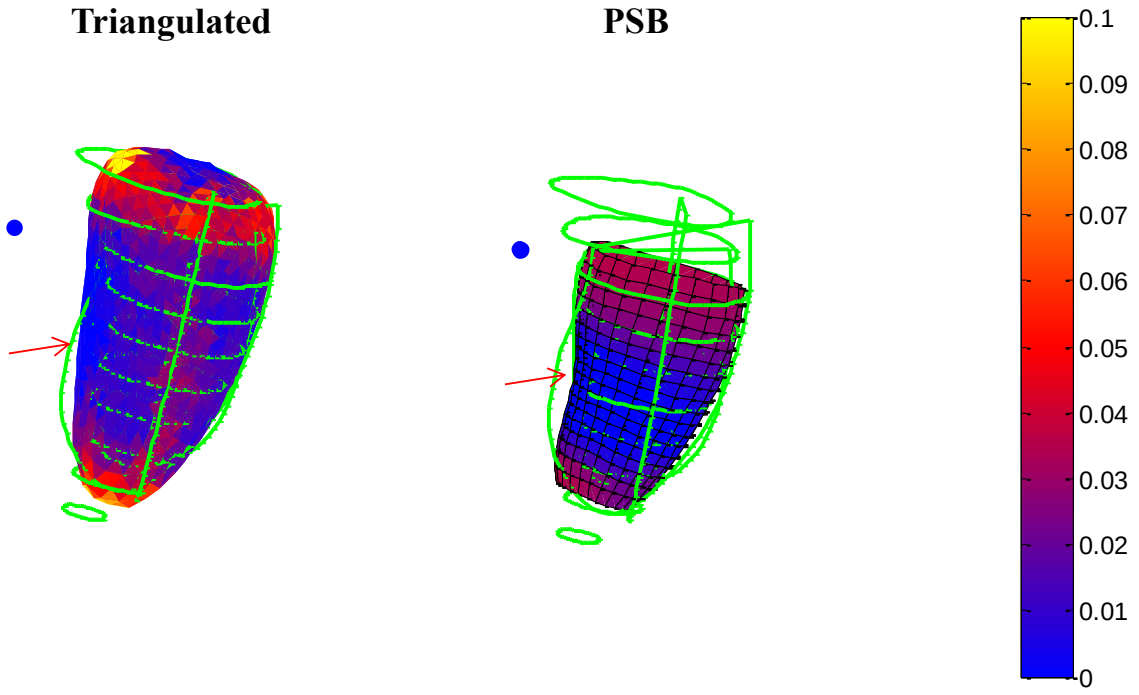

Figure 4.34 Illustration of the surface fitting by the proposed method vs. PSB
Left: a LVES surface from the normal test set fitted by the proposed method; Right: the same surface fitted by PSB; Triangulated, the proposed biventricular active mesh model; PSB: Prolate Spheroidal B-spline method; the surface color depicts the longitudinal curvature of the surface (1/mm). Red arrow indicates the mid ventricle of the surface; Green lines: contours; Blue dot: mid septum.

4.6.2.6 *Curvatures and Volumes in Different Pathologies*

The results of the first two projects presented in this dissertation indicate that patients with MR had significant LV apex remodeling, represented as smaller distal LV curvature compared to normal subjects. And due to the regurgitant flow to the lower pressure left atrium, LVSV in the MR patients was higher than that in the normal group. Moreover, it is known that patients with PH have higher RVEDV compared to normal subjects[144].

In this section, we compared the above mentioned clinical measurements derived by the proposed model between different pathologies to test whether the model can distinguish the difference between pathologies.

As observed in Figure 4.35, MR hearts tended to have smaller circumferential endocardial curvatures at apex compared to the normal hearts (0.069 ± 0.0098 vs. 0.094 ± 0.01 1/mm at LVED; 0.10 ± 0.01 vs. 0.13 ± 0.02 1/mm at LVES).

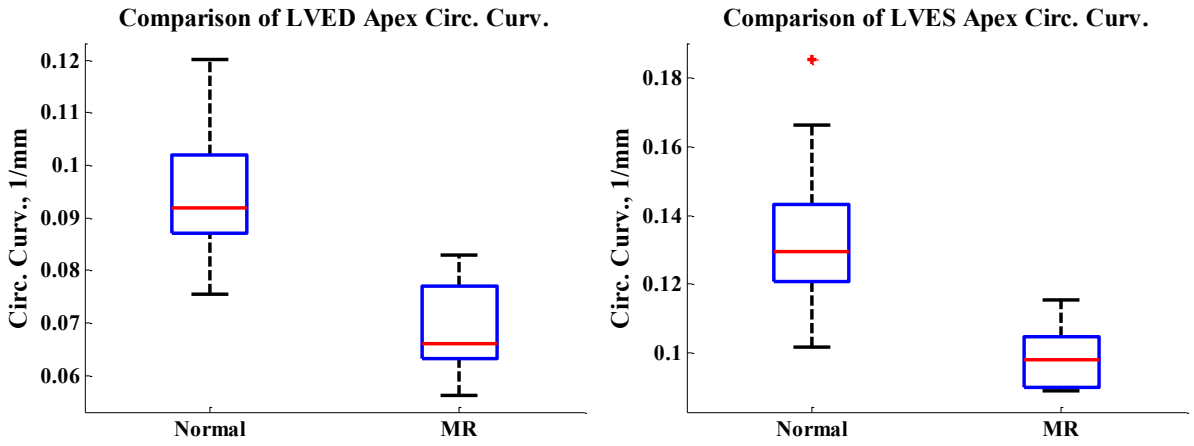

Figure 4.35 Compare LV Apex Curvatures between Normal and MR
Circ. Curv, circumferential curvature; LVED, left ventricle end-diastolic timeframe; LVES, left ventricle end-systolic timeframe; MR: mitral regurgitation; On each box, the central red mark is the median, the blue edges of the box are the 25th and 75th percentiles, the black whiskers represent the most extreme data points that are considered to be not outliers; +, outliers.

As the boxplot shows in Figure 4.36, the mean and medium LVSV was greater in the MR test set versus that in the normal test set (128 ±23 vs. 71 ±16 ml) due to the extra blood flow back to the left atrium during contraction.

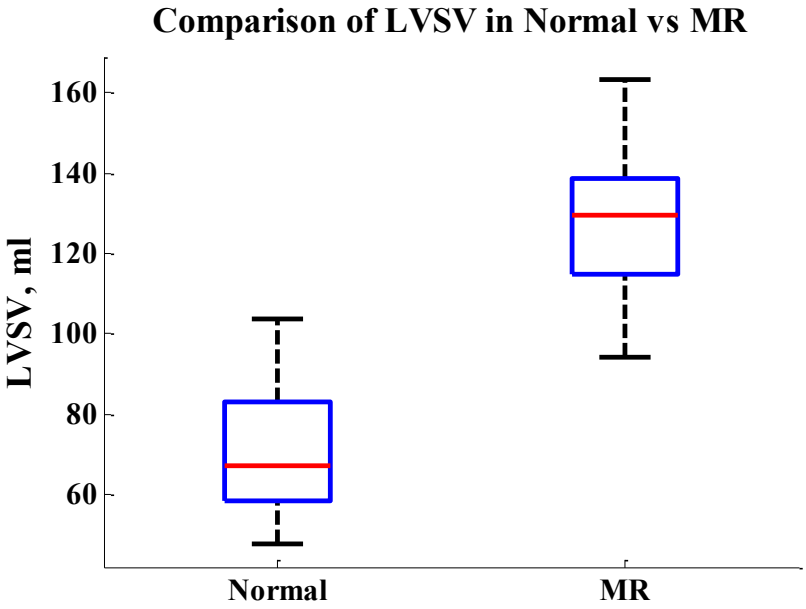

Figure 4.36 Boxplot of LVSV in the normal test group and MR test group
LVSV: left ventricle stroke volume; MR: mitral regurgitation; On each box, the central red mark is the median, the blue edges of the box are the 25th and 75th percentiles, the black whiskers represent the most extreme data points that are considered to be not outliers; +, outliers.

As the boxplot shows in Figure 4.37, the mean and medium RVEDV was greater in the PH test set versus that in the normal test set (181 ±47 vs. 125 ±31 ml).

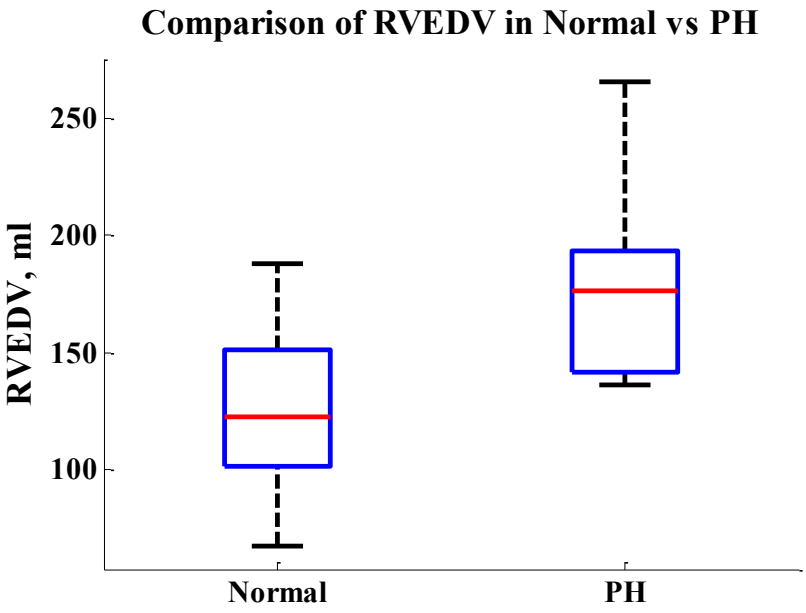

Figure 4.37 Boxplot of RVEDV in the normal test group and PH test group
RVEDV: right ventricle end-diastolic volume; PH: pulmonary hypertension; On each box, the central red mark is the median, the blue edges of the box are the 25th and 75th percentiles, the black whiskers represent the most extreme data points that are considered to be not outliers; +, outliers.

These boxplots show that the clinical parameters derived by the proposed method have the potential to successfully detect the different features between pathologies. Further validation with a larger sample set is necessary.

4.7 Discussion

The biventricular active mesh model proposed in this chapter successfully achieves the goal of fitting a smooth surface for both LV and RV with significant computational efficiency and being able to derive clinical useful parameters for LV and RV at all segment levels based on the meshes.

Our LV 3D segmentations include the information of both short axis and long axis contours in order to complete the knowledge of the apex. To generate the 3D segmentation from the long axis contours, we use angular interpolation of the three long axis contours by assuming

that the LV is symmetric, all long axis slices are perpendicular to the short axis slices and intersected with each other at the long axis of the LV. However, this is not always true for some scans. If any of the long axis slices is severely tilted from the long axis of the LV, the generated 3D long axis segmentation could be a wrong representation of the LV. As a result, in order to generate a true LV 3D segmentation, it requires accurate scanning with right perspective of the LV long axis slices.

For studies that only have three slices of long-axis view, there are usually only two long-axis slices with RV view. Therefore, 3D segmentations of RV for these studies are generated using only short axis slices. To compensate the missing information at RV apex that is provided by the long axis images, one extra short axis slice is manually added to where the RV apex landmark is.

Moreover, the quality of the 3D segmentations is affected by how well all the contours are registered. Although in the last step of our method, the new mesh is generated by the active mesh model which can potentially correct some misregistration error. The generation of training meshes is more affected by the misregistration error. Therefore, the contours must be well registered with user confirmation to generate the 3D segmentation.

The smoothness of the training meshes is controlled by the number of singularities and the tuning parameter γ of the smoothing function. The smoothing function (Equation 4.17) intends to smooth the surface by minimizing the difference in vertex surface normal vectors, while at the same time, matching the surface boundary. This process will stop when the change of the smoothing function reaches a user defined limit. The larger γ is, the more smooth the generated mesh is, the less goodness fit the mesh is. In this study, we set γ equal to 6 such that the generate mesh satisfied both the smoothness and goodness of fit criteria.

In this study, we have a relatively small training sample size. Therefore, AMM may not be able to capture and represent the new subjects accurately. In order to reduce the consequence of small sample size, we construct AMM based on ventricle and pathology specified PDM and apply AMM to subjects with the same specifications as its training sets. As Figure 4.27 and Figure 4.28 show, the constructed new meshes are more accurate and consistent.

The comparison of the circumferential curvatures calculated by the proposed method and the B-spline surface model based on prolate spheroidal coordinate system (PSB) shows a good agreement between the two methods. The maximum circumferential curvature difference is less than 10% in LVED and 8% in LVES. This curvature difference is in our acceptable range. Furthermore, the proposed method has a significant advantage over the PSB in that the proposed method can model both LV and RV and measure curvatures at all segment levels, which cannot be achieved by PSB. Moreover, the model validation results show that the proposed method can better model the LV and RV including the RV base to reduce the computed volume errors. Furthermore, the clinical measurements derived by the proposed model have the potential to successfully differentiate different pathologies.

The computation time for generating a mesh in the training set with V=1000, M=400 and γ=6 is about 2 hours and the computation time for generation a new mesh in the test set using the AMM-based method is less than 20 seconds.

4.8 Conclusion

In conclusion, our proposed novel biventricular active mesh model can construct both LV and RV surface meshes efficiently. Based on this model, we can accurately derive clinical useful parameters such as volume and curvatures at all segment levels in both LV and RV. The difference of the computed stroke volumes between LV and RV is close to zero. The comparison

of the curvatures computed by our proposed method and the PSB shows a good agreement between the two methods with a maximum 10% difference. Moreover, apex curvature, which is an important clinical parameter, is computable by our method. And the comparison of apex curvatures between the normal and MR group shows an expectable result. This method can be applied to real-time mesh generation during scanning.

CHAPTER 5 CONCLUSION AND FUTURE WORK

In this dissertation, three research topics were presented.

The first research topic evaluated the difference in cardiac geometry and function of patients with chronic, compensated MR versus marathoners, who represented pathologic and physiologic volume overload, respectively. This work represents the first study to compare 3D LV geometric remodeling and mechanics in marathoners versus chronic compensated MR utilizing cMR and 3D data analysis. My contribution to this work includes conceiving and designing the research hypothesis with Dr Louis Dell'Italia, generating or acquiring study data, analyzing the data using various statistical models, interpreting the data, describing the results and conclusions. The finding of this work is that in the setting of similar increases in LV volumes and stroke volume, marathoners' hearts maintain a normal LV sphericity and normal wall thickness with lower LV twist, while there is a greater global and regional LV sphericity in the MR hearts.

Upon the finding of the first study, we further assessed the important role that apex remodeling played in the progression of the severity of mitral regurgitation and its significance as an indicator for timing of surgery. My contribution to this work includes conceiving and designing the research idea with Dr. Louis Dell'Italia and Dr. Mustafa Ahmed, acquiring patients' clinical data, generating patients' cMR data, analyzing the data using various statistical models, interpreting the data, describing the results and conclusions, answering the statistical Reviewer's questions. The major finding of this work is that LVES dimension does not accurately reflect the

extent of LV remodeling, largely due to spherical LV remodeling from mid to apical LV by cMR with 3D analysis. This study demonstrates that even when LVES dimension remains below the accepted target of 40 mm for surgical intervention of isolated MR, its associated LVES volume can range as high as twice that of the normal controls, suggesting that cMR with 3D analysis or 3D echocardiography derived LV volumes may be preferred to evaluate disease progression in isolated MR.

These two clinical studies both emphasize the importance of studying ventricle remodeling at LV apex for patients with MR. However, the model that we use in-house to generate curvature measurement is a B-spline model based on prolate spheroidal coordinates which has a singularity at the LV apex. Moreover, this model is limited to only regular symmetric shapes, which is not suitable to complex shape like RV. Therefore, the last project proposed a novel biventricular active mesh model that was able to fit smooth surfaces to both the LV and RV including the LV apex and RV base. This model could accomplish real-time surface generation with significant computational efficiency and it was able to derive clinical useful parameters for LV and RV based on the constructed meshes. Moreover, such new meshes could potentially correct the contour errors near both the LV and RV outflow tract which were usually difficult to determine manually, since the generated new meshes were restricted by the variation from their training sets.

By utilizing this model, LV apex remodeling can be studied and more accurately quantified in the first two clinical studies. Furthermore, the proposed model generates more accurate volume measurements compared with the conventional method, which is summing up the volumes defined by the contours and multiplying it with slice thickness, therefore providing better volumetric analysis in these clinical studies. Since the clinical measurements of RV can be

obtained using the proposed model, comparison of RV size and curvatures between the marathoners and the MR patients in the first study should give us a more comprehensive understanding of these two types of volume overload.

Disease status and disease development of LV have been well studied in the past, however, RV heart failure has not been explored to the same extend, partially due to the limitation of imaging and modeling techniques. Now with the promise of cMR, the proposed method can certainly provide global and local measurements of the RV to help study the RV remodeling in human hearts with RV disease.

Further validation on the proposed model can be done in the future. Due to the uncertainty of both the right atrio-ventricular boundary and vague RVOT, the major difficulty of constructing a right ventricular surface model is an accurate determination of the boundary of the RV. Moreover, the RV has an irregular shape, very thin wall and sensitivity to the pulmonary pressure difference, which may increase the variation of the volume measurements. Therefore, an optimal verification of the right ventricular fitted model in the future will compare the volume calculated from the fitted model against right ventricular volume measurement from animal hearts ex vivo.

In conclusion, the research presented in this dissertation is both clinically and scientifically significant. More importantly, it makes an effort to bridge the gap between clinical practice and technical development by providing techniques to generate data which are clinical important and useful.

BIBLIOGRAPHY

[1] "*http://www.who.int/research/en/*"

[2] E. C. Lin, S. R. Klepac, and E. J. Samett, "Cardiac MRI–technical aspects primer," *E-medicine [online]*.

[3] "*http://www.texasheartinstitute.org/hic/anatomy/anatomy2.cfm*"

[4] "*http://www.uptodate.com/contents/images/CARD/1225/Cardiac_anatomy_PI.jpg*"

[5] R. E. Klabunde, *Cardiovascular physiology concepts*. Lippincott Williams & Wilkins, 2005.

[6] "*http://www.cvphysiology.com*"

[7] C. Mihl, W. R. M. Dassen, and H. Kuipers, "Cardiac remodelling: concentric versus eccentric hypertrophy in strength and endurance athletes," *Netherlands Heart Journal*, vol. 16, pp. 129-133, 2008.

[8] V. V. McLaughlin, S. L. Archer, D. B. Badesch, R. J. Barst, H. W. Farber, J. R. Lindner, M. A. Mathier, M. D. McGoon, M. H. Park, R. S. Rosenson, L. J. Rubin, V. F. Tapson, and J. Varga, "American College of Cardiology Foundation Task Force on Expert Consensus Documents; American Heart Association; American College of Chest Physicians; American Thoracic Society, Inc; Pulmonary Hypertension Association. ACCF/AHA 2009 expert consensus document on pulmonary hypertension a report of the American College of Cardiology Foundation Task Force on Expert Consensus Documents and the American Heart Association developed in collaboration with the American College of Chest Physicians; American Thoracic Society, Inc.; and the Pulmonary Hypertension Association," *Journal of American College of Cardiology*, vol. 53, pp. 1573–619, 2009.

[9] Y. Okajima, Y. Ohno, G. R. Washko, and H. Hatabu, "Assessment of Pulmonary Hypertension:: What CT and MRI Can Provide," *Academic Radiology*, vol. 18, pp. 437-453, 2011.

[10] K. Thygesen, J. S. Alpert, and H. D. White, "Universal definition of myocardial infarction," *Circulation*, vol. 116, pp. 2634-53, 2007.

[11] M. I. Ahmed, D. C. McGiffin, R. A. O'Rourke, and L. J. Dell'Italia, "Mitral regurgitation," *Current Problems in Cardiology*, vol. 34, pp. 93-136, 2009.

[12] R. O. Bonow, B. A. Carabello, K. Chatterjee, A. C. de Leon Jr, D. P. Faxon, M. D. Freed, W. H. Gaasch, B. W. Lytle, R. A. Nishimura, P. T. O'Gara, R. A. O'Rourke, C. M. Otto, P. M. Shah, J. S. Shanewise, S. C. Smith Jr, A. K. Jacobs, C. D. Adams, J. L. Anderson,

E. M. Antman, D. P. Faxon, V. Fuster, J. L. Halperin, L. F. Hiratzka, S. A. Hunt, B. W. Lytle, R. Nishimura, R. Page, and B. Riegel, "ACC/AHA 2006 guidelines for the management of patients with valvular heart disease: a report of the American College of Cardiology/American Heart Association Task Force on Practice Guidelines (writing Committee to Revise the 1998 guidelines for the management of patients with valvular heart disease) developed in collaboration with the Society of Cardiovascular Anesthesiologists endorsed by the Society for Cardiovascular Angiography and Interventions and the Society of Thoracic Surgeons," *Journal of the American College of Cardiology,* vol. 48, pp. 1-148, 2006.

[13] M. D. Cerqueira, N. J. Weissman, V. Dilsizian, A. K. Jacobs, S. Kaul, W. K. Laskey, D. J. Pennell, J. A. Rumberger, T. Ryan, and M. S. Verani, "Standardized myocardial segmentation and nomenclature for tomographic imaging of the heart: a statement for healthcare professionals from the Cardiac Imaging Committee of the Council on Clinical Cardiology of the American Heart Association," *Circulation,* vol. 105, pp. 539-542, 2002.

[14] C. G. Schiros, H. Aggarwal, M. I. Ahmed, S. G. Lloyd, H. Gupta, M. M. Bamman, D. C. McGiffin, T. S. Denney Jr, and L. J. Dell'Italia, "Increased myocardial strain and torsion in compensated pathological versus physiological left ventricular volume overload," presented at the ACC 11, 2011.

[15] E. A. Dawson, G. P. Whyte, M. A. Black, H. Jones, N. Hopkins, D. Oxborough, D. Gaze, R. E. Shave, M. Wilson, K. P. George, and D. J. Green, "Changes in vascular and cardiac function after prolonged strenuous exercise in humans," *J Appl Physiol,* vol. 105, pp. 1562-1568, 2008.

[16] M. H. Laughlin, "Cardiovascular response to exercise," *Am J Physiol,* vol. 277, pp. S244-259, 1999.

[17] N. F. Osman, W. S. Kerwin, E. R. McVeigh, and J. L. Prince, "Cardiac motion tracking using CINE harmonic phase (HARP) magnetic resonance imaging," *Magn Reson Med,* vol. 42, pp. 1048-1060, 1999.

[18] B. D. Levine, "VO2, max: what do we know, and what do we still need to know?," *J Physiol,* vol. 586, pp. 25-34, 2008.

[19] E. B. Fortescue, A. Y. Shin, D. S. Greenes, R. C. Mannix, S. Agarwal, B. J. Feldman, M. I. Shah, N. Rifai, M. J. Landzberg, J. W. Newburger, and A. C.S., "Cardiac troponin increases among runners in the Boston Marathon," *Ann Emerg Med,* vol. 49, pp. 137-143. e1, 2007.

[20] J. Lauschke and B. Maisch, "Athlete's heart or hypertrophic cardiomyopathy?," *Clin Res Cardiol,* vol. 98, pp. 80-88, 2009.

[21] P. D. Thompson, "Historical concepts of the athlete's heart," *Med Sci Sports Exerc,* vol. 36, pp. 363-70, 2004.

[22] B. Levine, L. Lane, J. Buckey, D. Friedman, and C. Blomqvist, "Left ventricular pressure-volume and Frank-Starling relations in endurance athletes. Implications for orthostatic tolerance and exercise performance," *Circulation,* vol. 84, pp. 1016-1023, 1991.

[23] H. Tanaka, F. A. Dinenno, K. D. Monahan, C. M. Clevenger, C. A. DeSouza, and D. R. Seals, "Aging, habitual exercise, and dynamic arterial compliance," *Circulation,* vol. 102, pp. 1270-5, 2000.

[24] M. I. Ahmed, J. D. Gladden, S. H. Litovsky, S. G. Lloyd, H. Gupta, S. Inusah, T. S. Denney, P. Powell, D. C. McGiffin, and L. J. Dell'Italia, "Increased oxidative stress and cardiomyocyte myofibrillar degeneration in patients with chronic isolated mitral regurgitation and ejection fraction> 60%," *J Am Coll Cardiol,* vol. 55, pp. 671-679, 2010.

[25] K. P. George, D. E. Warburton, D. Oxborough, J. M. Scott, B. T. Esch, K. Williams, S. Charlesworth, H. Foulds, A. Oxborough, M. D. Hoffman, and R. Shave, "Upper Limits of Physiological Cardiac Adaptation in Ultramarathon Runners," *J Am Coll Cardiol,* vol. 57, pp. 754-755, 2011.

[26] A. Pelliccia, F. Culasso, F. M. Di Paolo, and B. J. Maron, "Physiologic left ventricular cavity dilatation in elite athletes," *Ann Intern Med,* vol. 130, pp. 23-31, 1999.

[27] J. Scharhag, G. Schneider, A. Urhausen, V. Rochette, B. Kramann, and W. Kindermann, "Athlete's heart:: Right and left ventricular mass and function in male endurance athletes and untrained individuals determined by magnetic resonance imaging," *J Am Coll Cardiol,* vol. 40, pp. 1856-1863, 2002.

[28] A. Young, R. Orr, B. Smaill, and L. Dell'Italia, "Three-dimensional changes in left and right ventricular geometry in chronic mitral regurgitation," *Am J Physiol,* vol. 271, pp. H2689-700, 1996.

[29] K. L. Weeks and J. R. McMullen, "The Athlete's Heart vs. the Failing Heart: Can Signaling Explain the Two Distinct Outcomes?," *Physiology,* vol. 26, pp. 97-105, 2011.

[30] M. M. Lipschultz, *Differential Geometry*. New York: McGraw Hill, 1969.

[31] M. Di Donato, P. Dabic, S. Castelvecchio, C. Santambrogio, J. Brankovic, L. Collarini, T. Joussef, A. Frigiola, G. Buckberg, and L. Menicanti, "Left ventricular geometry in normal and post-anterior myocardial infarction patients: sphericity index and [] new'conicity index comparisons," *Eur J Cardiothorac Surg,* vol. 29, pp. S225-S230, 2006.

[32] T. S. Denney Jr, B. L. Gerber, and L. Yan, "Unsupervised reconstruction of a three dimensional left ventricular strain from parallel tagged cardiac images," *Magn Reson Med,* vol. 49, pp. 743-754, 2003.

[33] J. Li and T. S. Denney, "Left ventricular motion reconstruction with a prolate spheroidal B-spline model," *Phys Med Biol,* vol. 51, pp. 517-537, 2006.

[34] I. K. Russel, M. J. Gotte, J. G. Bronzwaer, P. Knaapen, W. J. Paulus, and A. C. van Rossum, "Left ventricular torsion: an expanding role in the analysis of myocardial dysfunction," *JACC Cardiovasc Imaging,* vol. 2, pp. 648-55, 2009.

[35] P. Knaapen, T. Germans, J. Knuuti, W. J. Paulus, P. A. Dijkmans, C. P. Allaart, A. A. Lammertsma, and F. C. Visser, "Myocardial energetics and efficiency: current status of the noninvasive approach," *Circulation,* vol. 115, pp. 918-927, 2007.

[36] R. A. Stewart, O. C. Raffel, A. J. Kerr, R. Gabriel, I. Zeng, A. A. Young, and B. R. Cowan, "Pilot Study to Assess the Influence of {beta}-Blockade on Mitral Regurgitant Volume and Left Ventricular Work in Degenerative Mitral Valve Disease," *Circulation,* vol. 118, pp. 1041-6, 2008.

[37] K. Jensen Urstad, B. Saltin, M. Ericson, N. Storck, and M. Jensen Urstad, "Pronounced resting bradycardia in male elite runners is associated with high heart rate variability," *Scand J Med Sci Sports,* vol. 7, pp. 274-278, 1997.

[38] B. Pat, C. Killingsworth, T. Denney, J. Zheng, P. Powell, M. Tillson, A. R. Dillon, and L. J. Dell'Italia, "Dissociation between cardiomyocyte function and remodeling with -adrenergic receptor blockade in isolated canine mitral regurgitation," *Am J Physiol Heart Circ Physiol,* vol. 295, pp. H2321-7, 2008.

[39] R. B. Weiner, A. M. Hutter Jr, F. Wang, J. Kim, A. E. Weyman, M. J. Wood, M. H. Picard, and A. L. Baggish, "The impact of endurance exercise training on left ventricular torsion," *JACC Cardiovascular Imaging,* vol. 3, p. 1001, 2010.

[40] T. Hiro, K. Katayama, T. Miura, M. Kohno, T. Fujii, J. Hiro, and M. Matsuzaki, "Stroke volume generation of the left ventricle and its relation to chamber shape in normal subjects and patients with mitral or aortic regurgitation," *Japanese circulation journal,* vol. 60, p. 216, 1996.

[41] C. G. Schiros, D. Clark III, J. D. Gladden, H. Gupta, S. G. Lloyd, D. C. McGiffin, T. Denney Jr, L. J. Dell'Italia, and M. I. Ahmed, "Importance of volumetric analysis as an indicator of left ventricular remodeling in patients with chronic severe mitral regurgitation," presented at the AHA 11, 2011.

[42] C. Schiros, L. Dell'Italia, J. Gladden, D. C. III, I. Aban, H. Gupta, S. Lloyd, D. McGiffin, T. Denney, and M. Ahmed, "Magnetic resonance imaging with three-dimensional analysis of left ventricular remodeling in isolated mitral regurgitation—implications beyond dimensions," *Circulation,* 2012.

[43] V. T. Nkomo, J. M. Gardin, T. N. Skelton, J. S. Gottdiener, C. G. Scott, and M. Enriquez-Sarano, "Burden of valvular heart diseases: a population-based study," *The Lancet,* vol. 368, pp. 1005-1011, 2006.

[44] M. Enriquez-Sarano, C. W. Akins, and A. Vahanian, "Mitral regurgitation," *The Lancet,* vol. 373, pp. 1382-1394, 2009.

[45] M. Enriquez-Sarano, A. J. Tajik, H. V. Schaff, T. A. Orszulak, M. D. McGoon, K. R. Bailey, and R. L. Frye, "Echocardiographic prediction of left ventricular function after correction of mitral regurgitation: results and clinical implications," *Journal of the American College of Cardiology,* vol. 24, pp. 1536-1543, 1994.

[46] J. S. Borer and R. O. Bonow, "Contemporary approach to aortic and mitral regurgitation," *Circulation,* vol. 108, p. 2432, 2003.

[47] D. H. Adams, R. Rosenhek, and V. Falk, "Degenerative mitral valve regurgitation: best practice revolution," *European heart journal,* vol. 31, p. 1958, 2010.

[48] Z. Samad, P. Kaul, L. K. Shaw, D. D. Glower, E. J. Velazquez, P. S. Douglas, and J. G. Jollis, "Impact of early surgery on survival of patients with severe mitral regurgitation," *Heart,* vol. 97, p. 221, 2011.

[49] D. H. Kang, J. H. Kim, J. H. Rim, M. J. Kim, S. C. Yun, J. M. Song, H. Song, K. J. Choi, J. K. Song, and J. W. Lee, "Comparison of early surgery versus conventional treatment in asymptomatic severe mitral regurgitation," *Circulation,* vol. 119, p. 797, 2009.

[50] M. Crawford, J. Souchek, C. Oprian, D. Miller, S. Rahimtoola, J. Giacomini, G. Sethi, and K. Hammermeister, "Determinants of survival and left ventricular performance after mitral valve replacement. Department of Veterans Affairs Cooperative Study on Valvular Heart Disease," *Circulation,* vol. 81, p. 1173, 1990.

[51] M. R. Zile, W. H. Gaasch, J. D. Carroll, and H. J. Levine, "Chronic mitral regurgitation: predictive value of preoperative echocardiographic indexes of left ventricular function and wall stress," *Journal of the American College of Cardiology,* vol. 3, pp. 235-242, 1984.

[52] G. Schuler, K. L. Peterson, A. Johnson, G. Francis, G. Dennish, J. Utley, P. Daily, W. Ashburn, and J. Ross Jr, "Temporal response of left ventricular performance to mitral valve surgery," *Circulation,* vol. 59, p. 1218, 1979.

[53] M. A. Flemming, H. Oral, E. D. Rothman, K. Briesmiester, J. A. Petrusha, and M. R. Starling, "Echocardiographic markers for mitral valve surgery to preserve left ventricular performance in mitral regurgitation* 1," *American Heart Journal,* vol. 140, pp. 476-482, 2000.

[54] K. Lindmark, S. Söderberg, D. Teien, and U. Näslund, "Long-term follow-up of mitral valve regurgitation--Importance of mitral valve pathology and left ventricular function on survival," *International journal of cardiology,* vol. 137, pp. 145-150, 2009.

[55] T. Matsumura, E. Ohtaki, K. Tanaka, K. Misu, T. Tobaru, R. Asano, M. Nagayama, K. Kitahara, J. Umemura, T. Sumiyoshi, H. Kasegawa, and S. Hosoda, "Echocardiographic prediction of left ventricular dysfunction after mitral valve repair for mitral regurgitation as an indicator to decide the optimal timing of repair," *J Am Coll Cardiol,* vol. 42, pp. 458-463, 2003.

[56] M. Enriquez-Sarano, J. F. Avierinos, D. Messika-Zeitoun, D. Detaint, M. Capps, V. Nkomo, C. Scott, H. V. Schaff, and A. J. Tajik, "Quantitative determinants of the outcome of asymptomatic mitral regurgitation," *N Engl J Med,* vol. 352, pp. 875-883, 2005.

[57] P. Montant, F. Chenot, A. Robert, D. Vancraeynest, A. Pasquet, B. Gerber, P. Noirhomme, G. El Khoury, and J. L. Vanoverschelde, "Long-term survival in asymptomatic patients with severe degenerative mitral regurgitation: a propensity score-based comparison between an early surgical strategy and a conservative treatment approach," *The Journal of thoracic and cardiovascular surgery,* vol. 138, pp. 1339-1348, 2009.

[58] R. Rosenhek, F. Rader, U. Klaar, H. Gabriel, M. Krejc, D. Kalbeck, M. Schemper, G. Maurer, and H. Baumgartner, "Outcome of watchful waiting in asymptomatic severe mitral regurgitation," *Circulation,* vol. 113, p. 2238, 2006.

[59] W. Feng, H. Nagaraj, H. Gupta, S. G. Lloyd, I. Aban, G. J. Perry, D. A. Calhoun, L. J. Dell'Italia, and T. S. Denney, "A dual propagation contours technique for semi-automated assessment of systolic and diastolic cardiac function by CMR," *J Cardiovasc Magn Reson,* vol. 11, pp. 11-30, 2009.

[60] H. Wyatt, M. Heng, S. Meerbaum, P. Gueret, J. Hestenes, E. Dula, and E. Corday, "Cross-sectional echocardiography. II. Analysis of mathematic models for quantifying volume of the formalin-fixed left ventricle," *Circulation,* vol. 61, pp. 1119-1125, 1980.

[61] L. J. Dell'Italia, G. G. Blackwell, D. J. Pearce, B. Thorn, and G. M. Pohost, "Assessment of Ventricular Volumes Using Cine Magnetic Resonance in the Intact Dog, A Comparison of Measurement Methods," *Investigative radiology,* vol. 29, p. 162, 1994.

[62] G. A. Barnard, "Significance tests for 2×2 tables," *Biometrika,* vol. 34, pp. 123-138, 1947.

[63] C. R. Mehta and P. Senchaudhuri, "Conditional versus unconditional exact tests for comparing two binomials," 2003.

[64] A. Sabri, K. Rafiq, R. Seqqat, M. A. Kolpakov, R. Dillon, and L. J. Dell'italia, "Sympathetic activation causes focal adhesion signaling alteration in early compensated volume overload attributable to isolated mitral regurgitation in the dog," *Circ Res,* vol. 102, pp. 1127-36, 2008.

[65] M. Dujardin, S. Karl, and M. Enriquez-Sarano, "Echocardiographic assessment of left ventricular remodeling: are left ventricular diameters suitable tools?," *Journal of the American College of Cardiology,* vol. 30, pp. 1534-1541, 1997.

[66] O. Ozdogan, A. Yuksel, C. Gurgun, M. Kayikcioglu, O. Yavuzgil, and C. S. Cinar, "Assessment of cardiac remodeling in asymptomatic mitral regurgitation for surgery timing: a comparative study of echocardiography and magnetic resonance imaging," *Cardiovascular Ultrasound,* vol. 8, p. 32, 2010.

[67] P. Cawley and C. Otto, "Valvular regurgitation: does cardiovascular magnetic resonance provide additional information compared to echocardiography?," *Minerva cardioangiologica,* vol. 57, p. 521, 2009.

[68] J. Borer, E. Herrold, C. Hochreiter, M. Roman, P. Supino, R. Devereux, P. Kligfield, and H. Nawaz, "Natural history of left ventricular performance at rest and during exercise after aortic valve replacement for aortic regurgitation," *Circulation,* vol. 84, p. III133, 1991.

[69] B. Villari, G. Vassalli, E. S. Monrad, M. Chiariello, M. Turina, and O. M. Hess, "Normalization of diastolic dysfunction in aortic stenosis late after valve replacement," *Circulation,* vol. 91, pp. 2353-2358, 1995.

[70] A. F. Frangi, W. J. Niessen, and M. A. Viergever, "Three-dimensional modeling for functional analysis of cardiac images, a review," *Medical Imaging, IEEE Transactions on,* vol. 20, pp. 2-25, 2001.

[71] Q. Duan, E. D. Angelini, and A. F. Laine, "Real-time segmentation by Active Geometric Functions," *Computer methods and programs in biomedicine,* vol. 98, pp. 223-230, 2010.

[72] J. K. Udupa, L. Wei, S. Samarasekera, Y. Miki, M. Van Buchem, and R. I. Grossman, "Multiple sclerosis lesion quantification using fuzzy-connectedness principles," *Medical Imaging, IEEE Transactions on,* vol. 16, pp. 598-609, 1997.

[73] M. Kass, A. Witkin, and D. Terzopoulos, "Snakes: Active contour models," *International journal of computer vision,* vol. 1, pp. 321-331, 1988.

[74] J. A. Sethian, *Level set methods and fast marching methods*. Cambridge Cambridge Univeristy Press, 1999.

[75] S. Osher and R. P. Fedkiw, *Level set methods and dynamic implicit surfaces*. vol. 153 Springer Verlag, 2003.

[76] T. F. Chan and L. A. Vese, "Active contours without edges," *Image Processing, IEEE Transactions on,* vol. 10, pp. 266-277, 2001.

[77] E. D. Angelini, S. Homma, G. Pearson, J. W. Holmes, and A. F. Laine, "Segmentation of real-time three-dimensional ultrasound for quantification of ventricular function: a clinical study on right and left ventricles," *Ultrasound in medicine & biology,* vol. 31, pp. 1143-1158, 2005.

[78] T. Cootes, C. Taylor, D. Cooper, J. Graham, and A. Lanitis, "Active shape models," *Computer vision and image understanding,* vol. 61, pp. 38-59, 1995.

[79] T. F. Cootes, G. J. Edwards, and C. J. Taylor, "Active appearance models," *Pattern Analysis and Machine Intelligence, IEEE Transactions on,* vol. 23, pp. 681-685, 2001.

[80] T. F. Cootes, C. J. Taylor, D. H. Cooper, and J. Graham, "Active shape models-their training and application," *Computer vision and image understanding,* vol. 61, pp. 38-59, 1995.

[81] C. Petitjean and J. N. Dacher, "A review of segmentation methods in short axis cardiac MR images," *Medical Image Analysis,* vol. 15, pp. 169-184, 2011.

[82] E. Bardinet, L. D. Cohen, and N. Ayache, "A parametric deformable model to fit unstructured 3D data," *Computer vision and image understanding,* vol. 71, pp. 39-54, 1998.

[83] S. Han, D. B. Goldgof, and K. W. Bowyer, "Using hyperquadrics for shape recovery from range data," in *Proc. 4th ICCV*, 1993, pp. 492-496.

[84] H. Huang, L. Shen, R. Zhang, F. Makedon, B. Hettleman, and J. Pearlman, "Surface alignment of 3D spherical harmonic models: Application to cardiac MRI analysis," *Medical Image Computing and Computer-Assisted Intervention–MICCAI 2005,* pp. 67-74, 2005.

[85] A. B. Abdallah, F. Ghorbel, K. Chatti, H. Essabbah, and M. H. Bedoui, "A new uniform parameterization and invariant 3D spherical harmonic shape descriptors for shape analysis of the heart's left ventricle-A pilot study," *Pattern Recognition Letters,* vol. 31, pp. 1981-1990, 2010.

[86] L. H. Staib and J. S. Duncan, "Model-based deformable surface finding for medical images," *Medical Imaging, IEEE Transactions on,* vol. 15, pp. 720-731, 1996.

[87] T. W. Sederberg and S. R. Parry, "Free-form deformation of solid geometric models," *ACM Siggraph Computer Graphics,* vol. 20, pp. 151-160, 1986.

[88] E. Bardinet, L. D. Cohen, and N. Ayache, "Tracking and motion analysis of the left ventricle with deformable superquadrics," *Medical Image Analysis*, vol. 1, pp. 129-149, 1996.

[89] C. Brechbühler, "Parametrization of closed surfaces for 3-D shape description," *Computer vision and image understanding*, vol. 61, pp. 154-170, 1995.

[90] M. Quicken, C. Brechbuhler, J. Hug, H. Blattmann, and G. Szekely, "Parameterization of closed surfaces for parametric surface description," 2000, pp. 354-360 vol. 1.

[91] G. Burel and H. Henoco, "Determination of the orientation of 3D objects using spherical harmonics," *Graphical Models and Image Processing*, vol. 57, pp. 400-408, 1995.

[92] M. Kazhdan, T. Funkhouser, and S. Rusinkiewicz, "Rotation invariant spherical harmonic representation of 3D shape descriptors," in *Proc. 2003 Eurographics/ACM SIGGRAPH Symposium on Geometry Processing* 2003, pp. 156-164.

[93] A. Makadia and K. Daniilidis, "Direct 3d-rotation estimation from spherical images via a generalized shift theorem," in *Proc. IEEE CVPR*, 2003, pp. 217-224.

[94] G. Coppini, R. Poli, and G. Valli, "Recovery of the 3-D shape of the left ventricle from echocardiographic images," *Medical Imaging, IEEE Transactions on*, vol. 14, pp. 301-317, 1995.

[95] A. Goshtasby and D. A. Turner, "Segmentation of cardiac cine MR images for extraction of right and left ventricular chambers," *Medical Imaging, IEEE Transactions on*, vol. 14, pp. 56-64, 1995.

[96] P. Hunter and B. Smaill, "The analysis of cardiac function: a continuum approach," in *Progress in biophysics and molecular biology*, 1988, p. 101.

[97] P. Hunter, P. Nielsen, B. H. Smaill, and I. LeGrice, "An anatomical heart model with applications to myocardial activation and ventricular mechanics," *Critical reviews in biomedical engineering*, vol. 20, p. 403, 1992.

[98] J. T. Oden, *Finite elements of nonlinear continua*. vol. 45 McGraw-Hill New York, 1972.

[99] B. Vallet, E. Angelini, and A. Laine, "Variational segmentation framework in prolate spheroidal coordinates for 3D real-time echocardiography," in *Medical Imaging 2006: Image Processing*, 2006, pp. 1370-1380.

[100] A. Young, P. Hunter, and B. Smaill, "Epicardial surface estimation from coronary angiograms," *Computer Vision, Graphics, and Image Processing*, vol. 47, pp. 111-127, 1989.

[101] A. Matheny and D. B. Goldgof, "The use of three-and four-dimensional surface harmonics for rigid and nonrigid shape recovery and representation," *Pattern Analysis and Machine Intelligence, IEEE Transactions on,* vol. 17, pp. 967-981, 1995.

[102] R. Tello, "Fourier descriptors for computer graphics," *Systems, Man and Cybernetics, IEEE Transactions on,* vol. 25, pp. 861-865, 1995.

[103] G. Stalidis, N. Maglaveras, S. N. Efstratiadis, A. S. Dimitriadis, and C. Pappas, "Model-based processing scheme for quantitative 4-D cardiac MRI analysis," *Information Technology in Biomedicine, IEEE Transactions on,* vol. 6, pp. 59-72, 2002.

[104] V. D. Liseikin, *Grid generation methods*. Springer Verlag, 2009.

[105] J. F. Thompson, B. K. Soni, and N. P. Weatherill, *Handbook of grid generation*. Boca Ration, Fla, USA: CRC, 1998.

[106] E. Keppel, "Approximating complex surfaces by triangulation of contour lines," *IBM Journal of Research and Development,* vol. 19, pp. 2-11, 1975.

[107] A. Ekoule, F. Peyrin, and C. Odet, "A triangulation algorithm from arbitrary shaped multiple planar contours," *ACM Transactions on Graphics (TOG),* vol. 10, pp. 182-199, 1991.

[108] D. Meyers, S. Skinner, and K. Sloan, "Surfaces from contours," *ACM Transactions on Graphics (TOG),* vol. 11, pp. 228-258, 1992.

[109] W. E. Lorensen and H. E. Cline, "Marching cubes: A high resolution 3D surface construction algorithm," *ACM Siggraph Computer Graphics,* vol. 21, pp. 163-169, 1987.

[110] W. J. Schroeder, J. A. Zarge, and W. E. Lorensen, "Decimation of triangle meshes," *COMPUTER GRAPHICS-NEW YORK-ASSOCIATION FOR COMPUTING MACHINERY-,* vol. 26, pp. 65-70, 1992.

[111] A. Hilton, A. Stoddart, J. Illingworth, and T. Windeatt, "Marching triangles: range image fusion for complex object modelling," in *Image Processing, 1996. Proceedings., International Conference on,* 1996, pp. 381-384 vol. 2.

[112] K. M. Oh and K. H. Park, "A vertex merging algorithm for extracting a variable-resolution isosurface from volume data," in *Systems, Man and Cybernetics, 1995. Intelligent Systems for the 21st Century., IEEE International Conference on*, 1995, pp. 3543-3548 vol. 4.

[113] H. Hoppe, T. DeRose, T. Duchamp, J. McDonald, and W. Stuetzle, "Mesh optimization," in *SIGGRAPH '93 Proceedings of the 20th annual conference on Computer graphics and interactive techniques*, 1993, pp. 19-26.

[114] J. Lotjonen, P. J. Reissman, I. E. Magnin, J. Nenonen, and T. Katila, "A triangulation method of an arbitrary point set for biomagnetic problems," *Magnetics, IEEE Transactions on,* vol. 34, pp. 2228-2233, 1998.

[115] F. Aurenhammer, "Voronoi diagrams—a survey of a fundamental geometric data structure," *ACM Computing Surveys (CSUR),* vol. 23, pp. 345-405, 1991.

[116] J. Peiró, L. Formaggia, M. Gazzola, A. Radaelli, and V. Rigamonti, "Shape reconstruction from medical images and quality mesh generation via implicit surfaces," *International journal for numerical methods in fluids,* vol. 53, pp. 1339-1360, 2007.

[117] J. C. Carr, W. R. Fright, and R. K. Beatson, "Surface interpolation with radial basis functions for medical imaging," *Medical Imaging, IEEE Transactions on,* vol. 16, pp. 96-107, 1997.

[118] P. J. Frey and P. L. George, *Mesh generation*. Wiley Online Library, 2000.

[119] S. Gibson, "Constrained elastic surface nets: Generating smooth surfaces from binary segmented data," *Medical Image Computing and Computer-Assisted Interventation—MICCAI'98,* pp. 888-898, 1998.

[120] O. Škrinjar and A. Bistoquet, "Generation of myocardial wall surface meshes from segmented MRI," *International Journal of Biomedical Imaging,* vol. 2009, pp. 1-1, 2009.

[121] G. Wahba, "Spline interpolation and smoothing on the sphere," *SIAM Journal on Scientific and Statistical Computing,* vol. 2, p. 5, 1981.

[122] C. Tobon-Gomez, C. Butakoff, P. Yushkevich, M. Huguet, and A. Frangi, "3D mesh based wall thickness measurement: identification of left ventricular hypertrophy phenotypes," in *Engineering in Medicine and Biology Society (EMBC), 2010 Annual International Conference of the IEEE*, 2010, pp. 2642-2645.

[123] T. Erber and G. Hockney, "Equilibrium configurations of N equal charges on a sphere," *Journal of Physics A: Mathematical and General,* vol. 24, p. L1369, 1991.

[124] L. Glasser and A. Every, "Energies and spacings of point charges on a sphere," *Journal of Physics A: Mathematical and General,* vol. 25, p. 2473, 1992.

[125] W. H. Press, S. A. Teukolsky, W. T. Vetterling, and B. P. Flannery, "Numerical recipes in C: the art of scientific computing," 1988.

[126] J. C. Gower, "Generalized procrustes analysis," *Psychometrika,* vol. 40, pp. 33-51, 1975.

[127] R. A. Johnson and D. W. Wichern, *Applied multivariate statistical analysis*. Pearson Prentice Hall, 2007.

[128] B. Van Ginneken, A. F. Frangi, J. J. Staal, B. M. ter Haar Romeny, and M. A. Viergever, "Active shape model segmentation with optimal features," *Medical Imaging, IEEE Transactions on,* vol. 21, pp. 924-933, 2002.

[129] J. Koikkalainen and J. Lotjonen, "Image segmentation with the combination of the PCA- and ICA-based modes of shape variation," pp. 149-152 Vol. 1.

[130] M. Üzümcü, A. Frangi, M. Sonka, J. Reiber, and B. Lelieveldt, "ICA vs. PCA active appearance models: Application to cardiac MR segmentation," *Medical Image Computing and Computer-Assisted Intervention-MICCAI 2003,* pp. 451-458, 2003.

[131] G. J. Edwards, C. J. Taylor, and T. F. Cootes, "Interpreting face images using active appearance models," in *Proc. Third Int'l Conf. Automatic Face and Gesture Recognition*, 1998, pp. 300-305.

[132] P. M. Thompson and A. W. Toga, "Detection, visualization and animation of abnormal anatomic structure with a deformable probabilistic brain atlas based on random vector field transformations," *Medical Image Analysis,* vol. 1, pp. 271-294, 1997.

[133] J. Lotjonen, S. Kivisto, J. Koikkalainen, D. Smutek, and K. Lauerma, "Statistical shape model of atria, ventricles and epicardium from short-and long-axis MR images," *Medical Image Analysis,* vol. 8, pp. 371-386, 2004.

[134] M. Lorenzo-Valdés, G. I. Sanchez-Ortiz, A. G. Elkington, R. H. Mohiaddin, and D. Rueckert, "Segmentation of 4D cardiac MR images using a probabilistic atlas and the EM algorithm," *Medical Image Analysis,* vol. 8, pp. 255-265, 2004.

[135] S. G. Chen and J. Y. Wu, "Estimating normal vectors and curvatures by centroid weights," *Computer Aided Geometric Design,* vol. 21, pp. 447-458, 2004.

[136] W. Kabsch, "A solution for the best rotation to relate two sets of vectors," *Acta Crystallographica Section A: Crystal Physics, Diffraction, Theoretical and General Crystallography,* vol. 32, pp. 922-923, 1976.

[137] E. W. Weisstein, "Delaunay triangulation," *From MathWorld–A wolfram Web Resource. http://mathworld. wolframe. com/DelaunayTriangulation. html,* 1999.

[138] C. Zhang and T. Chen, "Efficient feature extraction for 2D/3D objects in mesh representation," in *Image Processing, 2001. Proceedings. 2001 International Conference on*, 2001, pp. 935-938 vol. 3.

[139] X. Chen and F. Schmitt, "Intrinsic surface properties from surface triangulation," 1992, pp. 739-743.

[140] G. Taubin, "Estimating the tensor of curvature of a surface from a polyhedral approximation," 1995, p. 902.

[141] C. Dong and G. Wang, "Curvatures estimation on triangular mesh," *Journal of Zhejiang University-Science A*, vol. 6, pp. 128-136, 2005.

[142] C. Wollmann, "Estimation of the principle curvatures of approximated surfaces," *Computer Aided Geometric Design*, vol. 17, pp. 621-630, 2000.

[143] G. D. Meier, A. A. Bove, W. P. Santamore, and P. R. Lynch, "Contractile function in canine right ventricle," *American Journal of Physiology-Heart and Circulatory Physiology*, vol. 239, pp. H794-H804, 1980.

[144] N. F. Voelkel, R. A. Quaife, L. A. Leinwand, R. J. Barst, M. D. McGoon, D. R. Meldrum, J. Dupuis, C. S. Long, L. J. Rubin, and F. W. Smart, "Right ventricular function and failure," *Circulation*, vol. 114, pp. 1883-1891, 2006.